Microstrip Resonators made from Granular Aluminium for Microwave Circuit Quantum Electrodynamics

Microstrip Resonatoren aus granularem Aluminium für Mikrowellenschaltkreisquantenelektrodynamik

Masterarbeit

im Studiengang
"Master of Science"
im Fach Physik

an der Fakultät für Physik und Astronomie
der Ruhr-Universität Bochum

von
Isabel Pietka

aus
Bochum

Bochum
2019

Microstrip Resonators made from Granular Aluminium for Microwave Circuit Quantum Electrodynamics

Microstrip Resonatoren aus granularem Aluminium für Mikrowellenschaltkreisquantenelektrodynamik

Masterarbeit

im Studiengang

"Master of Science"

im Fach Physik

an der Fakultät für Physik und Astronomie

der Ruhr-Universität Bochum

von

Isabel Pietka

aus

Bochum

Bochum

2019

The institutions responsible for the supervision of this thesis are the Ruhr University Bochum, Germany, and the University Innsbruck, Austria. It was financed by the student exchange programme Erasmus+. The work described in this thesis was performed in the research group of Superconducting Quantum Circuits at the Institute for Quantum Optics and Quantum Information (IQOQI) of the Austrian Academy of Sciences and at the Institute for Experimental Physics at the University of Innsbruck, both located in Innsbruck, Austria.

1. Gutachter: Prof. Dr. D. Hägele
2. Gutachter: Univ.-Prof. Dr. Gerhard Kirchmair

Abstract

Granular aluminium provides desirable properties for designing superconducting quantum circuits. The material structure that consists of pure aluminium grains surrounded by aluminium oxide is comparable to a network of Josephson junctions (JJ) and features a high intrinsic impedance. Here, microstrip resonators made from granular aluminium have been simulated performing finite element simulation (HFSS), fabricated and characterized. The fabrication is related to conventional JJ fabrication and includes electron lithography and electron beam evaporation of aluminium in a pure oxygen atmosphere. The film room temperature resistivity determines the resonators microwave properties that can be assigned to different regimes, from low ($\rho \leq 100\,\mu\Omega\cdot\mathrm{cm}$) to strongly disordered ($\rho > 10^4\,\mu\Omega\cdot\mathrm{cm}$). Films of different room temperature resistivity are obtained by adjusting the process parameters, i.e. the oxygen mass flow and evaporation rate during the deposition. It is suggested to fabricate films with $\rho \sim 10^3\,\mu\Omega\cdot\mathrm{cm}$, at least one order below the superconductor to insulator transition (SIT) at $10^4\,\mu\Omega\cdot\mathrm{cm}$. The critical temperature of films with $\rho = 120(30)\,\mu\Omega\cdot\mathrm{cm}$ to $\rho = 4800(900)\,\mu\Omega\cdot\mathrm{cm}$ has been determined performing transport measurements and lies in a range from 1.3(5) K to 2.2(5) K, exceeding the transition temperature of bulk aluminium (1.2 K). The maximal T_c is reached at $\rho = 190(3)\,\mu\Omega\cdot\mathrm{cm}$. A U-shaped microstrip resonator that consists of two films differing in resistivity ($\rho_{\mathrm{low}} = 50(9)\,\mu\Omega\cdot\mathrm{cm}$, 40 nm thickness, $\rho_{\mathrm{high}} = 650(120)\,\mu\Omega\cdot\mathrm{cm}$, 20 nm thickness) has been investigated in transmission configuration by mounting it to a copper waveguide. The substrate material is sapphire. Resonance is found in the vicinity of 9 GHz and a coupling Q factor of $9.45(4)\times10^4$ and is in good agreement with simulation, corresponding to a kinetic sheet inductance of 20 pH. The internal Q factor is $8.98(5)\times10^4$ for photon numbers $\bar{N}$ between 10^2 and 10^6. A non-linear behaviour is observed for large $\bar{N} > 10^6$ that leads to a negative frequency shift of $-2.7(6)\times10^{-3}$ Hz per photon in the resonator. Moreover, external magnetic fields in the range of $\sim$ mT cause additional losses by non-zero restive regimes in the material and Q_i decreases by half. The temperature dependence could not have been investigated due to a small signal to noise ratio.

Zusammenfassung

Granulares Aluminium lässt sich hervorragend in supraleitenden Quantenschaltkreisen einsetzen. Isolierendes Aluminiumoxid umgibt die Aluminiumkörner in dem Material, so dass die Struktur an ein Array von Josephson-Kontakten erinnert. Hierdurch erhält das Material eine hohe intrinsische, kinetische Flächeninduktivität. In dieser Arbeit werden Microstrip-Resonatoren aus Aluminium mit Korngrenzen hergestellt, simuliert und ihre Mikrowelleneigenschaften werden untersucht. Der Herstellungsprozess ist vergleichbar mit der konventionellen Herstellung von Josephson-Kontakten und setzt sich aus Elektron-Lithografie und Aluminiumabscheidung in reiner Sauerstoffatmosphäre durch einen Elektronenstrahl zusammen. Der spezifische Widerstand bei Raumtemperatur bestimmt die Mikrowelleneigenschaften der Resonatoren und lässt sich anhand der Ordnung in Bereiche einteilen, von schwach ($\rho \leq 100\,\mu\Omega \cdot \mathrm{cm}$) bis stark ($\rho > 10^4\,\mu\Omega \cdot \mathrm{cm}$). Durch das Einstellen der Herstellungsparameter, genauer gesagt des Sauerstoffflusses und der Verdampfungsrate, lassen sich Filme verschiedener spezifischer Widerstände herstellen. Es wird dazu geraten, Filme von $\rho \sim 10^3\,\mu\Omega \cdot \mathrm{cm}$ herzustellen, mindestens eine Größenordnung unterhalb des Supraleiter-zu-Isolator-Übergangs bei $10^4\,\mu\Omega \cdot \mathrm{cm}$. Anhand von Transportmessungen wurde die Sprungtemperatur für Filme von $\rho = 120(30)\ \mu\Omega \cdot \mathrm{cm}$ bis $\rho = 4800(900)\ \mu\Omega \cdot \mathrm{cm}$ bestimmt. Diese überschreitet den Wert von Vollaluminium (1.2 K) und liegt in einem Bereich von 1.3(5) K bis 2.2(5) K. Der Maximalwert wird für $\rho = 190(30)\ \mu\Omega \cdot \mathrm{cm}$ erreicht. Die Transmission eines Microstrip-Resonator in U-Form bestehend aus zwei Filmschichten unterschiedlichen Widerstands ($\rho_{\mathrm{low}} = 50(9)\ \mu\Omega \cdot \mathrm{cm}$, 40 nm Schichtdicke, $\rho_{\mathrm{high}} = 650(120)\ \mu\Omega \cdot \mathrm{cm}$, 20 nm Schichtdicke) auf Saphir wurde untersucht. Hierfür wurde der Resonator in einen Waveguide aus Kupfer eingesetzt. Der Resonator zeigt Resonanz bei rund 9 GHz und weist einen Kopplungsgütefaktor von $9.45(4) \times 10^4$ auf. Für Photonenzahlen zwischen 10^2 und 10^6 liegt der interne Gütefaktor bei $8.98(5) \times 10^4$. Für größere Photonenzahlen $\bar{N} > 10^6$ wird ein nicht-lineares Verhalten deutlich, dass zu einer negativen Frequenzverschiebung von $-2.7(6) \times 10^{-3}$ Hz pro Photon im Resonator führt. Externe magnetische Felder in der Stärke von $\sim$ mT rufen nicht-supraleitende Bereiche in dem Resonatormaterial hervor und führen zu zusätzlichen internen Verlustmechanismen bei. Dadurch reduziert sich der interne Gütefaktor um 50 %. Die Temperaturabhängigkeit konnte wegen einem ungünstigen Signal-Rausch-Verhältnis nicht weiter untersucht werden.

Acknowledgement

This thesis would not have been possible without strong support of a team of many brilliant people. The work abroad at the renowned institute for quantum optics and quantum information (IQOQI) in Innsbruck, Austria, guided me to a new way of thinking. It turned out to be a great challenge but contributed to my personal development.
I have to acknowledge my two supervisors who both allowed me to elaborate my thesis in a stay abroad. My supervisor on-site, Gerhard Kirchmair (University Innsbruck), guided me through hard times by providing sophisticated advice and welcoming me, no matter how early or late it was in the day. I want to thank him for introducing me to the quantum world and for struggling with the pre-alpha versions of my thesis full of absolute beginner's mistakes.
The advising support from my home university and foundation of this thesis is own to Daniel Hägele (Ruhr University Bochum). His brilliant lectures originally motivated me to dive deeper into the quantum world. I want to acknowledge him for accepting without hesitation the supervision of a thesis elaborated abroad.
Before I decided to end my master's degree study in Innsbruck, I visited the institute on a day trip. On this busy day, it was the first working day of the new year, Aleksei Sharafiev and Christian Schneider introduced me to the thrilling research of the IQOQI superconducting quantum circuit group. Throughout my whole stay abroad, they supported me by sharing their experience and knowledge. A theoretical model discussed in this thesis is due to Aleksei's brilliant mind. Christian supported me incessantly in my experimental conduction and answered all of my questions, no matter how basic they were. I could not have elaborated my thesis without their help.
I owe this as well to the well-experienced researcher Mathieu Juan who promised me my problems are his one and helped me to achieve results I could not have achieved on my own.
I want to acknowledge David Zöpfl whose ambitious elaborated master thesis breaks down the research field my thesis topic is assigned to. At this point, I also want to thank the research group of Ioan Pop at the Karlsruhe Institute of Technology, especially the pioneer on granular aluminium Lukas Grünhaupt. Their scientific success paved the way for elaborating my thesis.
Stefan Oleschko, Phani Muppalla and Oscar Gargiulo shared their experience on finite element simulation with me and helped me to overcome the software pitfalls in the very beginning. Without them, I maybe would still run simulations. Especially, Oscar's original italic aura contributed to a pleasant workplace atmosphere.
The work in the cleanroom would have overextended me if Stephanie Wögerer and Markus Zanner had not shared their experience with me. Both of them mastered the challenging fabrication

of superconducting qubits and helped me to orient myself in this new field of work. I want to express my respect to them since I experienced the cleanroom work as very ambitious and highly frustrating. I owe the formal introduction to this working area to Markus Weiss.
I also want to thank Desislava Atanasova and Alvise Borgognoni, who started their master thesis right after me. Although we spent not much time together, the few conversations we had cheered me up, showing me that we are all in the same boat.
And I want to thank Andreas Strasser and Gerhard Hendl. Both of them supported me with custom-designed solutions for the sample mounting. Without them, none of my samples could have been placed in the cryostat.
Yet, I want to thank my family and friends from the heart for being always there, from beginning till the end of five years of study, although, they do not understand exactly what I am investigating. Thanks!

Contents

List of Figures

List of Tables

Introduction

Superconducting circuits find application in many different fields.. They found use in metrology [1], low temperatures detectors [2], solid-state quantum optics[3] and quantum nanomechanics [4]. Particular interesting are materials of high intrinsic impedance larger than the resistance quantum since they can be used to realize devices with sub-Cooper pair charge fluctuations[5]. Materials with large kinetic inductance comply with this, making them perfectly suitable for superconducting quantum bits[6] (SC qubits) and kinetic inductance detectors for quasiparticle detection [7][8]. A prominent candidate of the former one is the transmon qubit [9] that consists of a capacitance and a Josephson junction (JJ). The JJ leads to a certain anharmonicity, turning the circuit into a non-linear oscillator that provides a two-level system for quantum computation and simulation [10, 11]. However, the limited anharmonicity of the transmon is a disadvantage [12] but can be overcome by alternative architectures like the fluxonium qubit [13] that achieves comparable coherence times in the microsecond range and orders of magnitude larger anharmonicity [14]. In principle, the fluxonium is a transmon qubit shunted by large inductance. So-called superinductors [15] provide high enough inductances. They can be realized by arrays of hundreds of JJs [16]. However, their experimental success is limited due to complexity in design and fabrication. Granular aluminium (grAl) tough overcomes this difficulty: The material consists of pure aluminium grains covered by insulating aluminium oxide and behaves as an effective network of JJs [17]. It can be straight-forward fabricated using convenient JJ fabrication by depositing aluminium in a pure oxygen atmosphere. Furthermore, grAl features a high critical field [18] and an enhanced critical temperature [19]. Both are desirable properties for designing SC quantum circuits. Microwave resonators made of grAl provide low loss resonators, represented by high quality (Q) factors and their resonance can be flux tuned since grAl is sensitive to magnetic fields [20]. Based on this, grAl resonators can be used for coupling to other SC circuits, for instance, to read out the state of SC qubits [21]. This provides new opportunities in the field of analogue quantum simulations, the simulation of complex quantum phenomena. The figure below on the left side illustrates such a complex scenario: Transmons (shown in red) in a waveguide are placed in the propagation direction of the field. They are strongly coupled to each other, realizing a dipolar spin model. The resonators that are located on substrates (blue) couple to a certain qubit, such that the qubit state can be read out dispersively via the resonator.

Microwave resonators made from grAl are also suitable for investigating mechanical hybrid systems [22] that consist of a cavity, for instance, a SC quantum circuit that is coupled to a micromechanical oscillator excited to a quantum state. Those systems find application as ultra-sensitive acceleration sensors [23], optical to microwave converters [24] or single-photon detectors [25]. In particular, they allow the investigation of the transition from classical to quantum mechanics and the interplay between gravity and quantum physics. Exciting a mechanical quantum state requires a coupling strength between the micromechanical mode and the electromagnetic mode larger than the cavity decay rate [26]. This is also known as strong single-photon coupling regime. An appealing approach to realize with this is the implementation of a flux-sensitive quantum circuit [4]. The coupling is established inductively by modifying the circuit inductance through the motion of the mechanical oscillator. A microwave resonator extended by a SQUID (superconducting interference device) fulfils this requirement. While conventional SQUID resonators made of aluminium suffer from high magnetic fields, grAl overcomes this disadvantage since it features a high critical field, preserving the SC phase and providing a high Q, low-loss resonator. Therefore, grAl seems to be a good candidate as material for these systems. The figure below on the right side illustrates such a system: A cantilever modified by a magnet serves as the nanomechanical oscillator (grey) and is on top aligned of the resonator carrying the SQUID (orange).

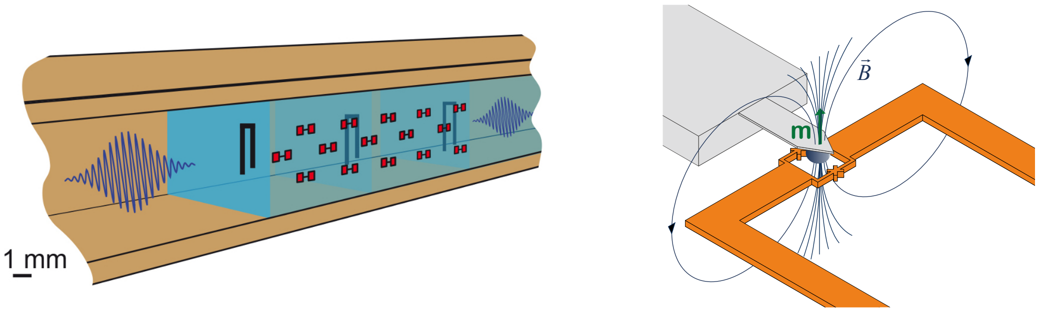

(a) (b)

Figure: (Left) Transmon qubits (red) placed in a waveguide presenting a dipole ladder. Using U-shaped resonators (black) each sitting on a single substrate (blue), slightly detuned in resonane compared to a certain qubit, the quantum state of it can be read out. (Right) Mechanical oscillator (grey) composed of a cantilever functionalized with a permanent magnet. The coupling to the mechanical mode is inductively achieved by a flux tuneable SQUID resonator (orange). Figures taken from www.iqoqi.at/de/forschung-gk, access on July 2019.

Overview of this thesis

In this thesis, high-impedance resonators made from grAlto characterize the material have been designed performing finite element simulation. Conventional aluminium deposition in an oxygen atmosphere is used for fabrication. Afterwards, the transmission has been measured to determine the internal and external (coupling) quality factor that represent losses through coupling to the environment and through internal loss mechanisms, for instance, the generation of quasiparticles. For this purpose, a fitting routine has been used.

Further, a low-impedance resonator has been fabricated and characterized. The resonator is investigated to refine a design for a SQUID resonator and is, therefore, composed of two deposition layers since they are necessary to realize the insulating barriers of the SQUID loop.
Since the critical temperature influences the microwave properties of superconducting resonators, samples for this investigation have been fabricated to determine the transition temperature as a function of room temperature resistivity.

The first part of the thesis introduces the theory on transmission lines and waveguides (chapter 1), the measurement (chapter 2) and superconductivity in granular aluminium (chapter 3). Chapter 4 presents the developed resonator designs and the fabrication process. Before discussing the resonator characterization in chapter 6, the determination of the transition temperature of grAl is given in chapter 5. The last chapter discusses the simulation results on a microstrip resonator coupled to a transmon qubit (chapter 7).

Chapter 1
Transmission Lines and Waveguides

As the microstrip resonators investigated in this thesis are conductors in which currents and voltages are oscillating, the first part of this chapter will offer an introduction to the fundamental concepts of transmission line theory. The propagation of current and voltage in a conductor are discussed. Furthermore, understanding the propagation of electric and magnetic fields in hollow conductors, so-called waveguides, is likewise essential. The second part of this chapter will explain wave propagation in waveguides.
This chapter only serves as a summary of these fundamentals. Further information can be found in the detailed textbook of D. Pozar [27].

1.1 Fundamentals

In general, every transmission line consists of two conductors, where an infinitesimal long section of it can be visualized as an electrical circuit with components l, c, g and r as shown in Fig. 1.1b. Here, l is the total self-inductance and c the shunt capacitance per length of the two conductors. The loss of the transmission line is expressed by the shunt conductance g and the resistance r per length, representing the dielectric loss due to the dielectric material in between the two conductors and the finite conductivity of the conductor material itself.

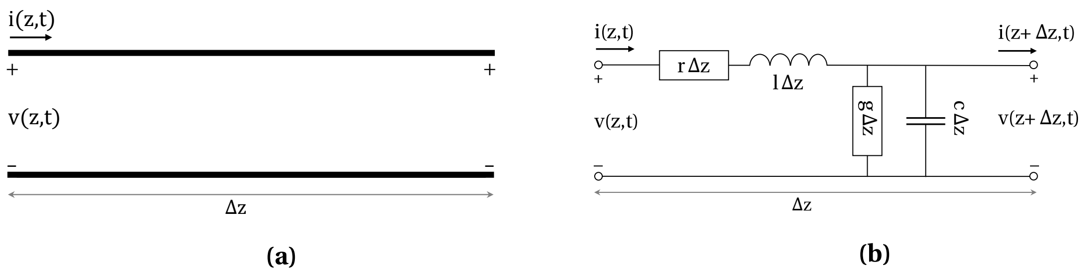

Figure 1.1: Incremental section of a transmission line: (a) Definition of voltage and current. (b) Equivalent circuit model. Adapted from D. Pozar [27].

Using Kirchhoff's current and voltage law, equations for the time and position dependent voltage v and current j in this circuit can be found:

$$v(z,t) - r\,\Delta z\; j(z,t) - l\,\Delta z \frac{dj(z,t)}{dt} - v(z+\Delta z,t) = 0 \tag{1.1}$$

$$j(z,t) - g\,\Delta z\; j(z,t) - c\,\Delta z \frac{dv(z+\Delta z,t)}{dt} - j(z+\Delta z,t) = 0\,. \tag{1.2}$$

With $\Delta z \to 0$, Eq. (1.1) transforms into the *telegrapher equation* [27] and can be further simplified, assuming a sinusoidal time dependence:

$$\frac{dV(z)}{dz} = -(r + i\omega l)\; I(z) \tag{1.3}$$

$$\frac{dI(z)}{dz} = -(g + i\omega c)\; V(z)\;. \tag{1.4}$$

$V(z)$ and $I(z)$ are the voltage and current in the steady-state condition. By introducing the complex propagation constant γ

$$\gamma = \alpha + i\beta = \sqrt{(r + i\omega l)(g + i\omega c)}\,, \tag{1.5}$$

where α is the attenuation and β the phase constant, the two differential equation can be written as

$$\frac{d^2V(z)}{dz^2} = -\gamma^2 V(z) \tag{1.6}$$

$$\frac{d^2I(z)}{dz^2} = -\gamma^2 I(z)\;. \tag{1.7}$$

The solution of this system corresponds to a travelling wave of the form

$$V(z) = V_0^+ e^{-\gamma z} + V_0^- e^{\gamma z} \tag{1.8}$$

$$I(z) = I_0^+ e^{-\gamma z} + I_0^- e^{\gamma z} \tag{1.9}$$

with a right propagating term ($e^{-\gamma z}$) and a left propagating one ($e^{\gamma z}$). Further, one can define the characteristic impedance Z_0 of the system given by

$$Z_0 = \frac{r + i\omega l}{g + i\omega c} \tag{1.10}$$

which also can be expressed by the ratio of the current and voltage:

$$\frac{V_0^+}{I_0^+} = Z_0 = -\frac{V_0^-}{I_0^-}\;. \tag{1.11}$$

For a transmission line without losses ($r = 0$ and $g = 0$) α is zero. This leads to a simplified expression of the impedance:

$$Z_0 = \sqrt{\frac{l}{c}}\,. \tag{1.12}$$

1.2 Terminated Lossless Transmission Line

This section will discuss the property of wave reflection, a phenomenon that occurs in transmission lines terminated by an arbitrary load impedance Z_L at $z = 0$ (see Fig. 1.2). This example illustrates the case of a system connected to a voltage source. The transmission line is assumed to be lossless (R = G = 0).

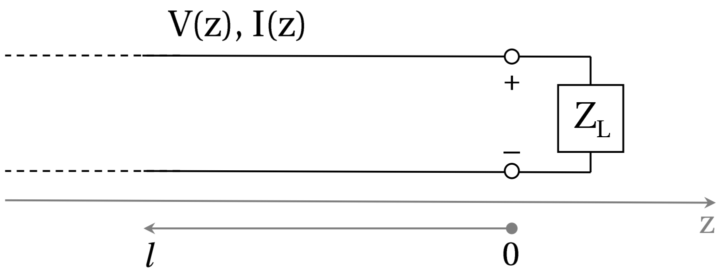

Figure 1.2: Terminated transmission line of length l with a load Z_L at its end. Adapted from D. Pozar [27].

Assuming an incident wave $V_0 e^{-i\beta z}$ is generated at $z < 0$, a part of the wave will be reflected at the position of the load as the impedance has to be equal to the load impedance to fulfil Eq. (1.11), $Z_L = V(0)/I(0)$:

$$V(z) = V_0^+ e^{-i\beta z} + V_0^- e^{i\beta z} \tag{1.13}$$

$$I(z) = I_0^+ e^{-i\beta z} + I_0^- e^{i\beta z}\,. \tag{1.14}$$

Solving for V_0^- at the position of the load one finds the relation

$$V_0^- = \frac{Z_L - Z_0}{Z_L + Z_0} V_0^+ \equiv \Gamma V_0^+\,. \tag{1.15}$$

Here, the fraction is defined as the reflection coefficient Γ. Rewriting Eq. (1.13), the proportion of the reflected wave component can be seen immediately, given by the second term in Eq. (1.16).

$$V(z) = V_0^+ \left(e^{-j\beta z} + \Gamma e^{j\beta z}\right) \tag{1.16}$$

Finally, the input impedance Z_{in}, which is located at the beginning of the transmission line in $z = -l$ is defined by

$$\begin{aligned} Z_{\text{in}} = \frac{V(-l)}{I(-l)} &= \frac{1+\Gamma e^{-2i\beta l}}{1-\Gamma e^{-2i\beta l}} Z_0 \\ &= \frac{Z_L + iZ_0 \tan(\beta L)}{Z_0 + iZ_L \tan(\beta L)} Z_0 \,. \end{aligned} \tag{1.17}$$

In the special situation of an open-circuited lossless line ($Z_{\text{in}} = \infty$ and $Z_L = \infty$), the equations for voltage, current and input impedance, Eq. (1.13), (1.14) and (1.17), simplify to

$$V(z) = 2V_0^+ \cos(\beta z) \tag{1.18}$$

$$I(z) = -2i \frac{V_0^+}{z_0} \sin(\beta z) \tag{1.19}$$

$$Z_{\text{in}} = -iZ_0 \cot(\beta l) \,. \tag{1.20}$$

Resonance occurs for a transmission line with a length equal to multiples of $\lambda/2$. V and I get reflected at the ends of the line, experiencing a phase jump of 2π. They share the behaviour of a standing wave, and the transmission line then represents a $n\lambda/2$-resonator ($n \in \mathbb{N}$). Fig. 1.3a and 1.3b shows a plot of the voltage, current, and impedance distribution as a function of the wavelength λ of such a special transmission line. The current equals zero at the ends of the transmission line, having a number of nodes depending on the order of resonance. The voltage reaches maxima at the nodes whereas the impedance goes to infinity.

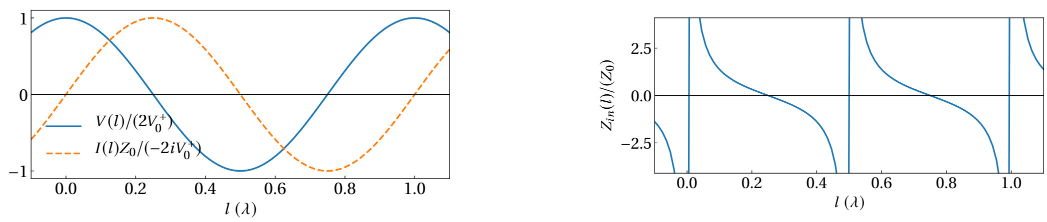

(a) **(b)**

Figure 1.3: (a) Voltage (solid) and current (dotted) distribution in a terminated transmission line compared to the wavelength λ. Voltage and current are reflected at the ends, experiencing a phase jump of 2π and having nodes depending on the mode number. (b) The impedance goes to infinity where the current equals zero according to $Z_{\text{in}} \propto \cot(\beta l)$.

1.3 Waveguides

A waveguide, having the capability to transmit electromagnetic waves with very low-loss and handling high powers, is the special case of a 3D transmission line. Waveguides with two conductors, e.g. coaxial cables can guide transverse electromagnetic (TEM) waves which are characterized by the lack of a field component in propagation (longitudinal) direction. Contrary to this, transverse electric (TE) and transverse magnetic (TM) waves have either magnetic or electric field components in the longitudinal direction.
This section starts with a general solution of Maxwell's equation for wave propagation in waveguides and discusses the solution for the special case of a rectangular one as well.

1.3.1 General Solution of Maxwell's equation

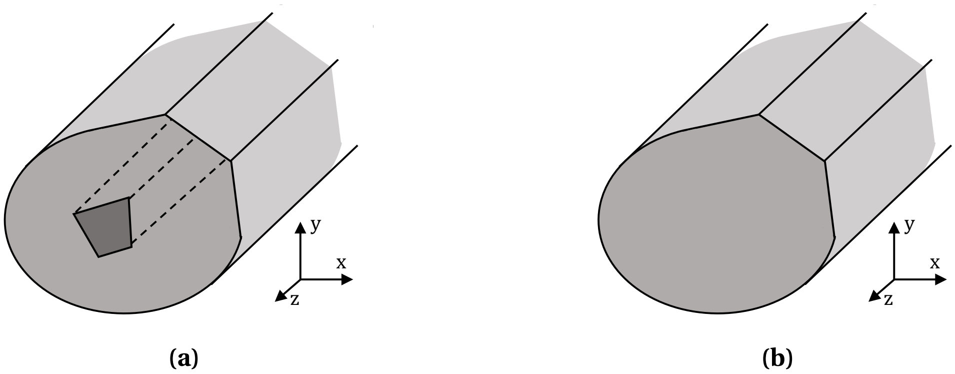

Figure 1.4: (a) Arbitrary shaped two-conductor and (b) single-conductor waveguide.

For an arbitrary, z-axis symmetric waveguide consisting of a single or two conductors presented in Fig. 1.4a and 1.4b the electric and magnetic fields have the form

$$\mathbf{E}(x,y,z) = [\mathbf{e}(x,y) + \mathbf{e_z}(z)\hat{z}]\, e^{-j\beta z} \tag{1.21}$$

$$\mathbf{H}(x,y,z) = [\mathbf{h}(x,y) + \mathbf{h_z}(z)\hat{z}]\, e^{-j\beta z}\ , \tag{1.22}$$

where $\bar{e}(x,y)$ and $\bar{h}(x,y)$ are the transverse field components and e_z and h_z the longitudinal ones, respectively. Here, it is assumed that the waves are harmonic in time and propagating in z-direction without losses, so the propagation constant equals β (Eq. (1.5)).

When assuming there are no sources in the waveguide, Faraday's induction law and Ampere's current law reduce to [27]

$$\nabla \times \mathbf{E} = -i\omega\mu_0 \mathbf{H} \tag{1.23}$$

$$\nabla \times \mathbf{H} = i\omega\epsilon_0 \mathbf{E}\,. \tag{1.24}$$

As the waves only propagate in the z-direction, one obtains for the x-component

$$H_x = i\frac{1}{k_c^2}\left(\omega\epsilon\frac{\partial E_z}{\partial y} - \beta\frac{\partial H_z}{\partial x}\right) \tag{1.25}$$

$$E_x = -i\frac{1}{k_c^2}\left(\beta\frac{\partial E_z}{\partial x} + \omega\mu\frac{\partial H_z}{\partial x}\right) \tag{1.26}$$

and a similar expression for the component in the y-direction. The cutoff wavenumber k_c is defined as [27]

$$k_c^2 = k^2 - \beta^2 \tag{1.27}$$

and $k = \omega\sqrt{\mu\epsilon} = 2\pi/\lambda$ is the wave number. The meaning of the cutoff wavenumber will become more clear in the next section.

1.3.2 TE Modes in a Rectangular Waveguide

Since a rectangular waveguide consists of one conductor, only TE and TM modes can propagate. In the case of TE waves, there is no electric field component in the propagation direction ($E_z = 0$). To solve the differential equations (1.25) and (1.26), one has to find a solution for H_z by solving the Helmholtz wave equation at first. As the wave only propagates in the z-direction, $H_z(x, y, z) = h_z(x, y)\, e^{-i\beta z}$, it reduces to

$$\left(\frac{\partial^2}{\partial x^2} + \frac{\partial^2}{\partial y^2} + k_c^2\right) h_z = 0\,. \tag{1.28}$$

Separating the variables, $h_z(x, y) = X(x)\, Y(y)$, the reduced Helmholtz equation leads to

$$\frac{1}{X}\frac{d^2 X}{dx^2} + \frac{1}{Y}\frac{d^2 Y}{dy^2} + k_c^2 = 0 \tag{1.29}$$

which has the general solution

$$h_z(x, y) = \left(A\cos(k_x x) + B\sin(k_x x)\right)\left(C\cos\left(k_y y\right) + D\sin\left(k_y y\right)\right)\,. \tag{1.30}$$

A solution for the constants A, B, C and D is found when using Eq. (1.25) and respecting the boundary condition that the electric field has to be zero at the waveguide walls. Finally, one obtains

$$H_z(x,y) = A_{mn}\cos\left(\frac{m\pi}{a}x\right)\cos\left(\frac{n\pi}{b}y\right)e^{-i\beta z}\,. \tag{1.31}$$

Here, A_{mn} represents an arbitrary amplitude constant composed of the remaining constants A and C, and m and n correspond to the mode order in x- and y-direction. With Eq. (1.31) and (1.26), an expression for the transverse electric field components propagating in the z-direction can be found:

$$E_x = i\frac{\omega\mu n\pi}{k_c^2 b}A_{mn}\cos\left(\frac{m\pi}{a}x\right)\sin\left(\frac{n\pi}{b}y\right)e^{-i\beta z} \tag{1.32}$$

$$E_y = -i\frac{\omega\mu m\pi}{k_c^2 b}A_{mn}\sin\left(\frac{m\pi}{a}x\right)\cos\left(\frac{n\pi}{b}y\right)e^{-i\beta z} \tag{1.33}$$

and similar expressions for the magnetic field components. The propagation constant β is given by

$$\beta = \sqrt{k^2 - k_c^2} = \sqrt{k^2 - \left(\frac{m\pi}{a}\right)^2 - \left(\frac{n\pi}{b}\right)^2}\,. \tag{1.34}$$

One can see that only modes with

$$k > k_c = \sqrt{\left(\frac{m\pi}{a}\right)^2 - \left(\frac{n\pi}{b}\right)^2} \tag{1.35}$$

can propagate as β stays real for this condition. For other modes, β is imaginary and the wave will decrease exponentially in the waveguide. The corresponding cutoff frequency $f_{c_{mn}}$ is

$$f_{c_{mn}} = \frac{k_c}{2\pi\sqrt{\mu\epsilon}} = \frac{1}{2\pi\sqrt{\mu\epsilon}}\sqrt{\left(\frac{m\pi}{a}\right)^2 - \left(\frac{n\pi}{b}\right)^2}\,. \tag{1.36}$$

The lowest cutoff frequency for a rectangular waveguide with $a > b$, as shown in fig. 1.5, is obtained for the TE_{10} mode: [27]

$$f_{c_{10}} = \frac{1}{2a\sqrt{\mu\epsilon}}\,. \tag{1.37}$$

Finally, an expression for the wave impedance is found in

$$Z_{\mathrm{TE}} = \frac{E_x}{H_y} = \frac{\beta\eta}{k}\,, \tag{1.38}$$

where $\eta = \sqrt{\mu/\epsilon}$ is the intrinsic free space impedance.

The power flow of the fundamental TE_{10} mode through the waveguide can be given using the expression for the electric and magnetic field components derived in Eq. (1.32) and (1.33):

$$\begin{aligned} P_{10} &= \frac{1}{2}\mathrm{Re}\left(\int_{x=0}^{a}\int_{y=0}^{b} \mathbf{E}\times\mathbf{H}^{\star} dy dx\right) \\ &= \frac{1}{2}\mathrm{Re}\left(\int_{x=0}^{a}\int_{y=0}^{b} E_y H_x^{\star} dy dx\right) \\ &= \frac{\omega\mu a^2}{2\pi^2}\mathrm{Re}(\beta)\,|A_{10}|^2 \int_{x=0}^{a}\int_{y=0}^{b} \sin^2\left(\frac{\pi x}{a}\right) dy dx \\ &= \frac{\omega\mu a^3 b}{4\pi}|A_{10}|^2 \mathrm{Re}(\beta)\ . \end{aligned} \tag{1.39}$$

1.3.3 TM Modes in a Rectangular Waveguide

A solution for the electric and magnetic field components in the xy-plane for the transverse magnetic modes can be found analogously as done for the TE modes with respecting $H_z = 0$. For this, a solution for $E_z(x,y,z)$ has to be found at first, again by solving the Helmholtz equation (1.28). Finally and under consideration of the boundary conditions that E_z has to be zero at the waveguide walls, one obtains for the electric field components

$$E_x = -i\frac{\beta m\pi}{k_c^2 a} B_{mn}\cos\left(\frac{m\pi}{a}x\right)\sin\left(\frac{n\pi}{b}y\right)e^{-i\beta z} \tag{1.40}$$

$$E_y = -i\frac{\beta n\pi}{k_c^2 b} A_{mn}\sin\left(\frac{m\pi}{a}x\right)\cos\left(\frac{n\pi}{b}y\right)e^{-i\beta z} \tag{1.41}$$

and again a similar expression for the magnetic field components. The propagation constant β and the wave impedance Z_{TM} stays the same as for the TE modes. However, in this case, the lowest fundamental mode is the TE_{11} mode since the fields vanish for other combinations of m and n. Fig. 1.5 shows an overview of the fundamental modes in a rectangular waveguide with $a = 2b$ with respect to the lowest TE_{10} mode.

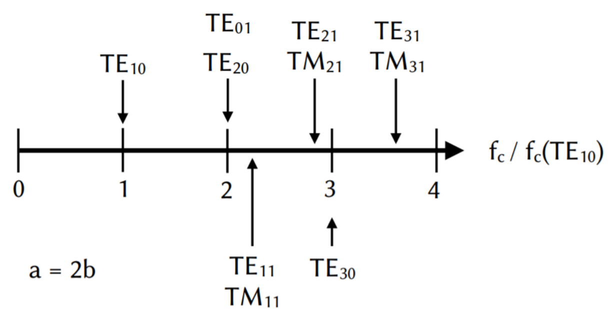

Figure 1.5: Modes and their cutoff frequencies in a rectangular waveguide with a = 2b, compared to the fundamental mode cutoff TE_{10}. From D. Zöpfl [28].

1.3.4 Equivalence of Current and Voltage

Determining voltage or current at microwave frequencies is difficult, especially for the single-conductor waveguide used in this thesis. For a two-conductor transmission line, e.g. a coaxial cable or a microstrip line, two ports exist such that the current can be determined using Ampere's law as the result does not depend on the integration path. The voltage can be calculated via the relation between current, voltage and impedance, Eq. (1.11). However, in the single-conductor case, e.g. the rectangular waveguide, current and voltage are spatially dependent [29] as illustrated in Fig. 1.6.

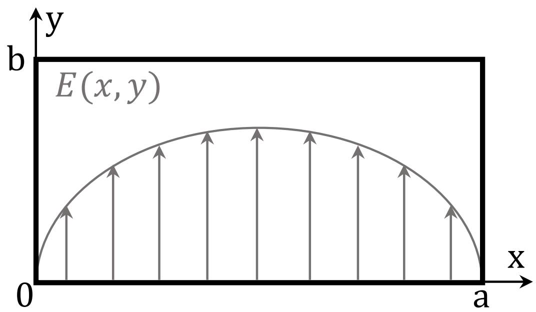

Figure 1.6: Shape of the electric field: fundamental TE_{10} mode in a rectangular waveguide with a = 2b. Adapted from D. Pozar [27].

In the following, a formulation of equivalent voltage and current will be given assuming the following considerations: [27]

1. Current and voltage are defined only for one certain waveguide mode and are proportional to the transverse magnetic and electric field.
2. Their product should give the power present to the conductor.
3. The relation defining the impedance, $Z = V/I$ (Eq. (1.11)), has to be respected.

With these considerations, the fundamental Eq. (1.8) and (1.9) for voltage and current can be modified to:

$$\mathbf{E}_t(x, y, z) = \frac{\mathbf{e}(x, y)}{C_v}\left(V^+ e^{-i\beta z} + V^- e^{i\beta z}\right) \tag{1.42}$$

$$\mathbf{H}_t(x, y, z) = \frac{\mathbf{h}(x, y)}{C_i}\left(I^+ e^{-i\beta z} + I^- e^{i\beta z}\right) . \tag{1.43}$$

Here, **e** and **h** are the transverse field variations of the mode that are sinusoidal shaped for the fundamental mode in the rectangular waveguide,

$$\mathbf{e}(x,y) = \sin\left(\frac{\pi x}{a}\right)\hat{y} \tag{1.44}$$

$$\mathbf{h}(x,y) = \frac{\hat{z} \times \mathbf{e}(x,y)}{Z_w} \,. \tag{1.45}$$

Here, Z_w is the wave impedance. The constants C_v and C_i can be determined by the conditions for power and impedance mentioned above.

1.3.5 Microstrip Line

This section introduces the architecture of a microstrip line since the system of the resonators sitting on a substrate that is placed in a waveguide corresponds to this geometry. Further, the influence on the resonators eigenfrequency of the microstrip intrinsic parameters that are width, length and impedance, will be summarized. This knowledge is necessary to understand the development of the resonator designs discussed in chapter 4.1.

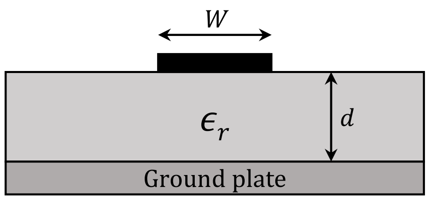

Figure 1.7: Microstrip line geometry: A microstrip (black) lies on top of a dielectric (light grey) that sits on a ground plate (dark grey). From the other side, the microstrip is covered by air.

Fig. 1.7 shows a schematic drawing of the microstrip line geometry: The system is composed of a wire (the microstrip) that is located above a ground plate and is surrounded by a dielectric on one side and air on the other. In this thesis, the dielectric corresponds to the substrate that is in contact with the ground plate, the waveguide.

Even though this system contains two conductors like a coaxial cable, the microstrip line cannot guide TEM waves because the dielectric contributes a phase difference between the field contained in the dielectric and the fraction propagating in air [27]. Similar to other resonators, the fundamental eigenfrequency f_r of the microstrip resonator is given by its total inductance L and capacitance C and is linked to the effective impedance via $Z = \sqrt{L/C}$:

$$f_r = \frac{1}{\sqrt{LC}} \propto Z \,. \tag{1.46}$$

Usually, the dielectric is very thin, $d \ll \lambda$, and the system can be treated like in the static case. From curve-fit approximations, a solution for the phase velocity v_p, propagation constant β and characteristic impedance Z_0 can be found when introducing an effective dielectric constant ϵ_e given by [27]

$$\epsilon_e = \frac{\epsilon_r + 1}{2} + \frac{\epsilon_r - 1}{2} \frac{1}{\sqrt{1 + 12d/W}} \,. \tag{1.47}$$

This constant represents the average dielectric surrounding the whole microstrip. It follows that $v_p = c/\sqrt{\epsilon_e}$ and $\beta = k\sqrt{\epsilon_e}$. For the case of this thesis, $W \leq d$, the characteristic impedance is given by [27]

$$Z_0 = \frac{60}{\sqrt{\epsilon_e}} \ln\left(\frac{8d}{W} + \frac{W}{4d}\right) \,. \tag{1.48}$$

For $W \ll d$, one can approximate the logarithm

$$Z_0 = \frac{60}{\sqrt{\epsilon_e}} \ln(8d) - \ln(W) \tag{1.49}$$

and see that Z_0 decreases with increasing length W. So does the eigenfrequency, too, according to Eq. (1.46) since the characteristic impedance contributes to the total impedance, Z.

Another, more illustrative description of how the geometry of the resonator influences its eigenfrequency can be given when considering the microstrip resonator as a simple wire as it is: By increasing the length of the wire, its total inductance L increases similar to coils serially interconnected. When increasing the width, the inductance decreases since the added conductor material acts as a parallel circuit of inductances. Therefore, the eigenfrequency of the microstrip resonator rises proportionally to its width while decreasing with its length. Moreover, the microstrip material itself, the granular aluminium, contributes to a high intrinsic impedance. This allows the realization of relative short resonators with high eigenfrequencies compared to conventional resonators made of pure aluminium or niobium [28].
Finally, one can conclude that length and width are the dominant properties in the determination of the microstrip resonators frequency.

Chapter 2
Resonator in an Environment

This chapter will give a closer look at the theory of measurement and the measurement configuration. At first, the scattering parameters are discussed which are fundamental for describing the quality of the coupling between resonator and waveguide. A general discussion on the quality factor is given in the section afterwards. Before the interaction between resonator and waveguide is pointed out on a classical basis, the losses are discussed.
Following, an introduction in the measurement configuration that is the notch configuration is given. At the end of this chapter, the circle fit is presented, a fit routine that has been implemented in the superconducting circuits group at the IQOQI Innsbruck. This routine is used to extract the parameters – Q factors and resonance frequency – from the measurement.
For elaborating this chapter, the theses by M.J. Reagor [30], A. Palacios-Laloy [31] and D. Zöpfl [28] have been used. More details can be found in their works.

2.1 Scattering Parameters

To obtain the transmitted or reflected power in a circuit network, for instance, a resonator coupled to a waveguide, one can compare the voltage amplitude and phase at the specific ports of the circuit. The scattering matrix $\underline{S}$ contains this information and will be introduced next. Furthermore, $\underline{S}$ can be transferred into the impedance matrix $\underline{Z}$ and therefore offers a full description of the circuit [27]. For an arbitrary circuit represented as a network with n ports the scattering matrix, or S-matrix, is defined as

$$\begin{pmatrix} V_1^- \\ V_2^- \\ \vdots \\ V_N^- \end{pmatrix} = \begin{pmatrix} S_{11} & S_{12} & \cdots & S_{1N} \\ S_{21} & S_{22} & \cdots & S_{2N} \\ \vdots & \vdots & \ddots & \vdots \\ S_{N1} & S_{N2} & \cdots & S_{NN} \end{pmatrix} = \begin{pmatrix} V_1^+ \\ V_2^+ \\ \vdots \\ V_N^+ \end{pmatrix} . \tag{2.1}$$

For a single entry, one reads

$$S_{ij} = \left. \frac{V_i^-}{V_j^+} \right|_{V_k^+=0 \text{ for } k \neq j} . \tag{2.2}$$

The parameter S_{ij} is obtained when port j is driven with a specific voltage V_j^+ and the output voltage V_i^- at port i is measured. To determine the bare parameter, every other port except port j should be terminated in a matched load to avoid reflections. Based on this method, the transmission coefficient is obtained while the reflection coefficient S_{ii} is measured when every port except port i is terminated.

Note that in a network without losses, the scattering matrix becomes purely imaginary and unitary. Furthermore, in a reciprocal network that is the usual case, the S-matrix is symmetric. This means, for a two-port reciprocal network as it is the case in this thesis, the knowledge of S_{11} and S_{21} are sufficient to offer a full description of the network.

2.2 Quality Factor

Before presenting the measurement configuration, the meaning of the quality factor Q will be discussed. In principle, the Q factor indicates how long a photon stays in a resonator. Large Q factors indicates a long photon lifetime. For a resonant circuit, the quality factor is generally defined as

$$Q = 2\pi \frac{\text{average energy stored in resonator}}{\text{energy dissipated per cycle}} = \frac{\omega_r}{2\gamma} , \tag{2.3}$$

where γ is the damping of the system that corresponds to the bandwidth $\delta\omega = |\omega_2 - \omega_2| = 2\gamma$ shown in Fig. 2.1. The resonance frequency is ω_r. Moreover, the bandwidth equals the coupling rate $\kappa = 2\gamma$ between the circuit and its environment. The Q factor itself is a dimensionless number which provides information about the width of the resonance and the energy loss in the circuit. If a full circuit model is available, the quality factor can be calculated by [30]

$$\begin{aligned} Q &= \left. \frac{1}{Z_0 \mathrm{Re}\,(Y)} \right|_{\omega=\omega_r} \\ &= \omega_r RC , \end{aligned} \tag{2.4}$$

where Z_0 is the characteristic impedance of the resonator and $Y = 1/Z$ is the admittance. R and C depict the resistance and capacitance of the resonator. The total or load quality factor, Q_L, consists of two loss channels, namely the internal and external (or coupling) ones, Q_i and Q_c:

$$\frac{1}{Q_l} = \frac{1}{Q_c^{Re}} + \frac{1}{Q_i} \,. \tag{2.5}$$

It should be noted that only the real part of Q_c is regarded since it is a complex number and describes besides the coupling losses also the phase shift caused by a possible impedance mismatch in the circuit [30].

$$\frac{1}{Q_c^{\mathrm{Re}}} = \mathrm{Re}\left(\frac{1}{Q_c}\right) = \frac{1}{|Q_c|} e^{i\phi_0} \,. \tag{2.6}$$

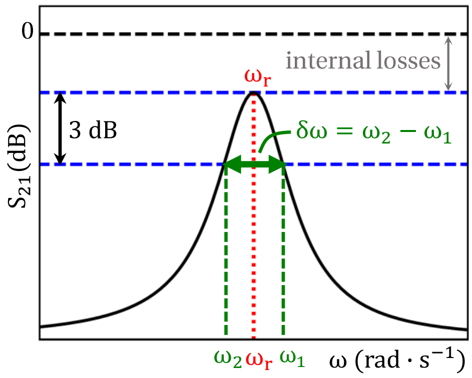

Figure 2.1: Transmission spectrum of a resonator at its resonance ω_r. The distance between the maximum and 0 dB equals the internal loss. The bandwidth $\delta\omega = \omega_2 - \omega_1$ is read at full width at half maximum at approximately 3 dB and equals two times the damping γ. Adapted from S. Meier [32].

The internal channel Q_i covers dissipative losses arising from intrinsic variables of the system, such as material impurities. The external one is determined by coupling losses that enable control over the circuit from the outside. That means, Q_i cannot be changed while Q_c can be adjusted, e.g. by the geometry of the setup [30].

By the ratio of Q_i to Q_c, one distinguishes between three different coupling regimes:
If $Q_c \gg Q_i$, the majority of losses stem from internal nature. The system then is called "under-coupled". In the opposite case, $Q_c \ll Q_i$, the losses are mainly paid off the outside, i.e. the transmission line. In the case, both channels are served equally, the system is critically coupled ($Q_c \approx Q_i$). In general, the resonators lifetime is limited by the lower quality factor.

Table 2.1: Survey of the different coupling regimes

$Q_c \approx Q_i$	critically coupled
$Q_c \gg Q_i$	under-coupled
$Q_c \ll Q_i$	over-coupled

2.3 Loss Mechanisms

In total, a variety of loss mechanisms contribute to the two loss channels, the internal and external one. The total power dissipated in the circuit is expressed by

$$\Gamma_{\mathrm{tot}} = \sum_n \Gamma_n \, , \tag{2.7}$$

where one specific mechanism consumes power at a rate Γ_n. This leads to the definition

$$\frac{1}{Q} = \sum_n \frac{1}{Q_n} = \frac{1}{\omega E_{\mathrm{tot}}} \sum_n \Gamma_n \, , \tag{2.8}$$

where E_{tot} is the total energy stored and $\omega = 2\pi f$. It should be mentioned that Q_n is the net result of all losses. That means Q_n will differ for different resonator geometries even if all material properties are the same.

A loss mechanism is described by its lossiness and the sensitivity to the mechanism [30]. The quantity that contains information about the sensitivity to this mechanism is the participation ratio which is defined as

$$p_n = \frac{\text{energy stored in the mechanism}}{\text{total energy stored}} \, . \tag{2.9}$$

By the definition of the ratio between the energy stored in a specific (lossy) volume compared to the energy stored in the total volume, the participation ratio is sensitive to the geometrical layout of the circuit. However, the specific lossiness of the mechanism expressed by the loss tangent $\tan(\delta_n)$ depends on the used materials and their intrinsic properties. Finally, it follows

$$Q_n = \frac{1}{p_n \tan(\delta_n)} = \frac{q_n}{p_n} \, . \tag{2.10}$$

If $Q_n = q_n$, so p_n is close to unity, the system is particularly sensitive to this mechanism.

2.3.1 External Loss

(a) **(b)**

Figure 2.2: (a) Equivalent circuit of a resonator coupled via a capacitance C_{couple} to a load R_{ext}. (b) Model of the circuit with a parallel impedance to simplify the problem and to find an expression for Q_c. Adapted from M. Reagor [30].

For readout purpose, every resonator is coupled to a certain port, sharing the same loss mechanism. Fig. 2.2 shows a LC circuit capacitively coupled to an external load via a capacitance C_{couple}. To derive an expression for Q_c, first the admittance Y_{ext} needs to be found:

$$Y_{\text{ext}} = \frac{1}{R + \frac{1}{i\omega C_{\text{couple}}}} \,. \tag{2.11}$$

This expression simplifies in the case of weak coupling, $\omega C_{\text{couple}} \ll R$, to

$$Y_{\text{ext}} = i\omega C_{\text{couple}} + \omega^2 C_{\text{couple}}^2 R_{\text{ext}} \,. \tag{2.12}$$

The total admittance of the circuit with total inductance L and capacitance C is then given by

$$\begin{aligned} Y_{\text{tot}} &= \frac{1}{i\omega L} + i\omega C + i\omega C_{\text{couple}} + \omega^2 R_{ext} \\ &= \frac{1}{i\omega L} + i\omega C_{\text{tot}} + \omega^2 R_{\text{ext}} \,. \end{aligned} \tag{2.13}$$

With the characteristic impedance $Z_0 = \sqrt{L/C}$ and using Eq. (2.4), the coupling quality factor can be expressed by

$$Q_c = \frac{1}{\omega_r^2 C_{\text{couple}}^2 R_{\text{ext}} Z_0} \,. \tag{2.14}$$

2.3.2 Internal Loss

Multiple mechanisms contribute to the internal loss channel. First, there are losses relying on the electric and magnetic energy that is stored in the material and, therefore, can be characterized by the participation ratio. Since the electric and magnetic fields transmit these energies, these losses are mainly of dielectric and conductive nature. In the following, the mechanisms behind them will be described briefly. More details can be found in the PhD thesis of J. Reagor [30].

Dielectric losses occur since the electric field exists in dielectrics. That means, in the substrate, holding the resonator, and in oxide layers, for instance, the substrate surface and the surface of the waveguide. Compared to other circuit structures, e.g. planar geometries, the employed 3D waveguide geometry profits from the advantage that the electric field vanishes on its walls, as discussed in chapter 1.3. Therefore, it supports a higher Q_i because less or no energy can be stored on the waveguide's surfaces. Additionally, the participation ratio for the dielectric loss scales inversely proportional with the electrode distance. So, the large distance of the waveguide's walls compared to a planar device also provides a low participation ratio, supporting a higher Q_i.

Losses caused by magnetic fields appear as conductive losses since the magnetic field induces currents in the conductive material. Because the resonator will be in the superconducting state while measuring, conductive losses play a minor role and instead dominate circuits made from normal conducting metal. However, at finite temperatures, due to non-equilibrium quasiparticles or vortices, the resonator still can have a finite conductivity for which reason it is hard to exclude magnetic losses. Based on a two-fluid model, the influence on the internal Q factor can be approximated by [33]

$$\frac{1}{Q_i^{n_e,n_s}} = \frac{A}{T}\exp\left(-\frac{\Delta}{k_B T}\right) + \frac{1}{Q_{\text{other}}}\,. \tag{2.15}$$

Based on this, a decrease of Q_i with increasing temperature is expected. The energy gap of the superconductor is Δ, and A is a constant determined by fitting. The Boltzmann term accounts for quasiparticle generation and the additional offset $1/Q_{\text{other}}$ respects other loss mechanisms without temperature dependency. Eq. (2.15) is valid for bulk superconductors up to $T < T_c/2$ [32].

Further, losses to two-level systems (TLS) contribute to the internal loss mechanism [34]. These are losses due to saturation of impurities that act as dipoles. The impurities can be found in the substrate and on surfaces. The contributing loss can be approximated by

$$\frac{1}{Q_i^{\text{TLS}}} = F\delta_{\text{TLS}}\tanh\left(\frac{hf_r(T)}{2k_B T}\right) + \frac{1}{Q_{\text{other}}}\,. \tag{2.16}$$

The expression δ_{TLS} denotes the loss tangent towards TLS and F is the filling factor of the TLS containing medium. Based on this, one expects an increase of Q_i for large input powers because the two-level systems get saturated. High temperatures lead to the same effect since they also support the saturation. In contrast, low power inputs lead to a maximal loss and Q_i converges to a finite value.

2.4 Waveguide Resonator Interaction

This section provides a closer look at the interaction between a resonator and its environment based on a classical consideration. An expression for Q_c in dependence of the resonator position relative to the waveguide will be derived. The model has been originally developed by A. Sharafiev. Details can be found in the handbook by Tai [35].

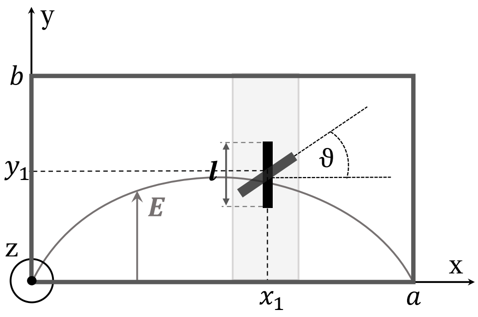

Figure 2.3: Waveguide resonator interaction: A resonator (black) is located in (x_1, y_1) and tilted by an angle ϑ in a waveguide. The substrate is shown in light grey.

The resonator is assumed to be an elongated dipole with length $|\mathbf{l}|$ located in the centre of the waveguide that has width a and height b, see Fig. 2.3. The electromagnetic field is propagating through the waveguide with frequency ω and causes the charge q in the resonator to oscillate. The total charge is given by

$$q = \int_0^{\pi/\omega} S \cdot |\mathbf{J}| \sin(\omega t) dt = \frac{2}{\omega} S |\mathbf{J}| \,. \tag{2.17}$$

Here, S equals the resonator cross section and $\mathbf{J}$ is the current density vector that is assumed to be

$$\mathbf{J}(\mathbf{r}) = \left(j_x \hat{\mathbf{x}} + j_y \hat{\mathbf{y}} + j_z \hat{\mathbf{z}} \right) \cdot \delta(\mathbf{r} - \mathbf{r}') \,, \tag{2.18}$$

where $\delta(\mathbf{r} - \mathbf{r}')$ denotes the delta-distribution and j_x, j_y and j_z correspond to the components of $\mathbf{J}$. The direction vectors are $\hat{\mathbf{x}}$, $\hat{\mathbf{y}}$ and $\hat{\mathbf{z}}$. The dipole moment is given by $\mathbf{d} = q \cdot \mathbf{l}$. To satisfy the dimensional differences between the one-dimensional dipole and its cross section S, the integral over the delta distribution $\delta(\mathbf{r} - \mathbf{r}')$ is assumed to be $1/V$ whereas $V = S \cdot |\mathbf{l}|$ is the resonator volume.

Respecting the phase difference between **d** and **J** of $\pi/2$, it follows

$$\mathbf{d} = q \cdot \mathbf{l} = i\frac{2}{\omega V}\left(j_x\hat{\mathbf{x}} + j_y\hat{\mathbf{y}} + j_z\hat{\mathbf{z}}\right) . \tag{2.19}$$

According to Eq. (2.3), the coupling Q factor is defined by

$$Q_c = \frac{W}{\tau \cdot P_{10}} , \tag{2.20}$$

where W is the total energy stored in the resonator, $\tau = \omega/2\pi$ is the oscillation period and P_{10} is the power flow through the waveguide of the fundamental TE_{10} mode. In the following derivation, only this mode will be considered ($m = 1$, $n = 0$). The resonator modelled as a dipole provides a total energy equal to the Coulomb energy

$$W = \frac{q^2}{4\pi\epsilon_0 l} = \frac{|\mathbf{d}|^2}{4\pi\epsilon_0 l^3} . \tag{2.21}$$

The power flow P_{10} is calculated according to Eq. (1.40):

$$P_{10} = 2\frac{\omega\mu a^3 b}{4\pi}|A_{10}|^2 \mathrm{Re}\{\beta\} . \tag{2.22}$$

Here, $\beta = \sqrt{k_c^2 - k^2}$ is the propagation constant of the field. The additional factor 2 respects that the resonator mode decays in both directions of the waveguide. An expression for the amplitude A_{10} can be found when calculating the electric field using dyadic analysis and the Green's function formalism:

$$\mathbf{E}(\mathbf{r}) = i\omega\mu \int_{V'} \mathbf{G}_{e1}(\mathbf{r}, \mathbf{r}') \cdot \mathbf{J}(\mathbf{r}) dV' . \tag{2.23}$$

The vector $\mathbf{r}'$ points to the location of the dipole charge. The function $\mathbf{G}_{e1}(\mathbf{r}, \mathbf{r}')$ corresponds to the dyadic Green's function for the electric field of the first kind and is given by

$$\begin{aligned}\mathbf{G}_{e1}(\mathbf{r}, \mathbf{r}') = \frac{1}{k^2}\mathbf{zz}\delta(\mathbf{r} - \mathbf{r}') + \frac{i}{ab}\sum_{m,n}\frac{2-\delta_0}{k_c^2\beta}\left(\mathbf{M}_{emn}(\pm\beta)\cdot\mathbf{M}'_{emn}(\mp\beta)\right) \\ + \mathbf{N}_{omn}(\pm\beta)\cdot\mathbf{N}'_{omn}(\mp\beta) , z \lessgtr z' .\end{aligned} \tag{2.24}$$

The functions $\mathbf{N}_{omn}(\beta)$ reproduce TM modes and, therefore, can be neglected while $\mathbf{M}_{emn}(\beta)$ correspond to TE modes. The indices 'o' and 'e' identify *odd* and *even*, respectively. More details on these can be found in the book of Chen-Cho Tai [35]. For arbitrary m, n, $\mathbf{M}_{emn}(\beta)$ is given by

$$\mathbf{M}_{emn}(\beta) = \left[-k_y\cos(k_x x)\sin(k_y y)\hat{\mathbf{x}} + k_x\sin(k_x x)\cos(k_y y)\,\hat{\mathbf{y}}\right]\cdot e^{i\beta z} . \tag{2.25}$$

When assuming the current density vector to be only defined in the x- and y-direction, $\mathbf{M}_{emn}(\beta)$

reduces for the TE_{10} mode to

$$\mathbf{M}_{e10}(\beta) = \sin\left(\frac{\pi x}{a}\right)\left(\frac{\pi}{a}\right) e^{i\beta z}\hat{y} \tag{2.26}$$

using the definitions $k_x = \pi/a$ and $k_y = \pi/b$. The expression for the Green's function results then in

$$\mathbf{G}_{e1}(\mathbf{r},\mathbf{r}') = \frac{i}{ab}\frac{1}{k_c^2\beta}\left(\frac{\pi}{a}\right)^2 \sin\left(\frac{\pi x}{a}\right)\sin\left(\frac{\pi x_1}{a}\right)\exp\left(i\beta z\right)\hat{\mathbf{y}}\hat{\mathbf{y}}\,. \tag{2.27}$$

To obtain the final expression for the electric field, the integral in Eq. (2.23) has to be solved. Note that **J** is assumed to be $\mathbf{J} = j_y\delta(\mathbf{r}-\mathbf{r}')$. The δ-distribution can be written as $\delta(\mathbf{r}-\mathbf{r}') = \delta(x-x')\delta(y-y')\delta(z-z')$. Finally, it is

$$\mathbf{E}(\mathbf{r}) = i\omega\mu\frac{i}{ab}\frac{1}{k_c^2\beta}\left(\frac{\pi}{a}\right)^2 \sin\left(\frac{\pi x}{a}\right)\sin\left(\frac{\pi x_1}{a}\right) e^{i\beta(z-z_1)} j_y\hat{\mathbf{y}}\,. \tag{2.28}$$

An expression for the coefficient j_y can be found using the above definition for the resonator dipole moment, Eq. (2.19). Dividing the dipole moment in its x- and y-proportions, $\mathbf{d} = |\mathbf{d}|\cos(\vartheta)\hat{x} + |\mathbf{d}|\sin(\vartheta)\hat{y}$, j_y is obtained to be:

$$j_y = -\frac{i\omega}{2}|\mathbf{d}|\sin(\vartheta)\,. \tag{2.29}$$

The final expression for the electric field yields

$$\mathbf{E}(\mathbf{r}) = -i\frac{\omega^2\mu}{2ab}\frac{|\mathbf{d}|}{k_c^2\beta}\left(\frac{\pi}{a}\right)^2 \sin(\vartheta)\sin\left(\frac{\pi x}{a}\right)\sin\left(\frac{\pi x_1}{a}\right) e^{i\beta z}\hat{\mathbf{y}}\,. \tag{2.30}$$

Comparing this expression with the electric field y-component derived in Eq. (1.33), the amplitude of the field is given by

$$A_{10} = -\frac{\omega\pi}{2a^2 b}\frac{|\mathbf{d}|}{k_c^2\beta}\left(\frac{\pi}{a}\right)^2 \sin(\vartheta)\sin\left(\frac{\pi x_1}{a}\right)\,. \tag{2.31}$$

Finally, the coupling Q factor can be defined using the above expressions and the definition in Eq. (2.20).

$$
\begin{aligned}
Q_c &= \frac{a^5 k_c^4 \beta b}{\pi^6 l^3 \omega^2 \mu \epsilon} \frac{1}{\sin^2(\vartheta)\sin^2\left(\frac{\pi x_1}{a}\right)} \\
&= \frac{ab}{l^3 \pi^2 \omega Z_{10}(\omega)\epsilon} \frac{1}{\sin^2(\vartheta)\sin^2\left(\frac{\pi x_1}{a}\right)}
\end{aligned}
\tag{2.32}
$$

Here, the wave impedance $Z_{10}(\omega) = \omega\mu/\beta$ for the fundamental mode has been used according to Eq. (1.38) and $k_c = \pi/a$. One can see that Q_c increases to infinity when ϑ reaches multiples of $n\pi$, $n \in \mathbb{N}$, according to the proportionality to $\sin^{-2}(\vartheta)$.
Concluding, the coupling between resonator and waveguide can be increased by tilting the resonator horizontally.

2.5 Measurement Configuration

Figure 2.4: Equivalent circuit representation of a resonator coupled to a transmission line in notch configuration: (a) For simplification the circuit is presented with general impedances Z_1, Z_2, and Z_3. (b) shows the same circuit with specific components. Adapted from D. Zöpfl.[28]

As already mentioned at the beginning of this chapter, the resonators in this thesis are measured in notch configuration. So, the S_{21} parameter is of interest. In a two-port reciprocal network, S_{21} is obtained when driving a voltage at port 2 and receiving the signal at port 1. Figure 2.4a shows the equivalent circuit of this configuration in generality using arbitrary impedances Z_1, Z_2 and Z_3. In Fig. 2.4b, the same circuit is shown when considering specific elements: The resonator is modelled as a LCR oscillator with losses R and the transmission line that means the waveguide, with an external resistance R_{ext}. The coupling capacitance C_{couple} expresses the capacitive coupling between resonator and waveguide. With these assumptions, an expression for the S_{21} coefficient can be given in dependency of the total and external Q factors and the resonance frequency f_r [31].
Since the impedances Z_1 and Z_2 do not have to be equal, there is an impedance mismatch causing

a phase shift ϕ_0 that leads to a shifted resonance frequency: $f_r' = f_r + \delta f$. The transmission coefficient then depends on the shifted frequency and the load and coupling Q factors:

$$S_{21} = 1 - \frac{Q_l/Q_c}{1 + 2iQ_l \frac{f - f_0'}{f_0'}} \,. \tag{2.33}$$

Fig. 2.5 shows the S parameter of an ideal resonator in notch configuration in the complex plane and the coupling of different Q_c/Q_i ratios.

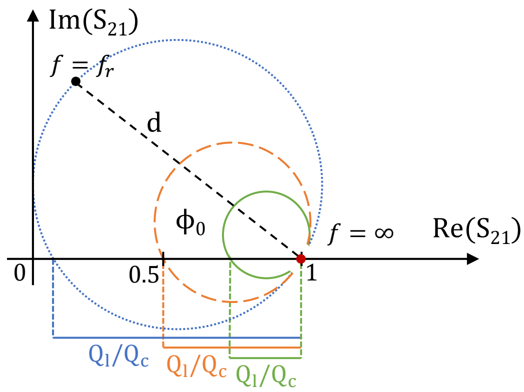

Figure 2.5: Coupling regimes in notch configuration: The diameter of the circle increases when the system is over-coupled and decreases when under-coupled visualized by the ratio of Q_l/Q_c. When critically coupled, the circle crosses the real axis at 0.5. Adapted from D. Zöpfl [28].

For off-resonant probing frequencies, $|f - f_r| \ll 0$, the S_{21} parameter goes to unity, marked by a red dot in Fig. 2.5. The resonant point, $f = f_r$, lies on the opposite due to the phase shift of π and is additionally shifted by the impedance mismatch ϕ_0, whereas $S_{21} \rightarrow 1 - Q_l/|Q_c|$. The circle diameter and its intersection with the real axis give information about the coupling of the resonator: The axis section between the crossing with the circle and 1 equals the ratio of Q_l/Q_c. The remaining distance to the origin corresponds to Q_l/Q_i. The resonator is critically coupled when the circle crosses the axis at 0.5. In this case, coupling losses equal the internal losses ($Q_c \approx Q_i$). The diameter increases when the system is over-coupled ($Q_i \ll Q_c$) and decreases when under-coupled ($Q_c \ll Q_i$).

2.6 Circle Fit Routine

The circle fit routine is applied to extract the Q factors and exact resonance frequency from the measurement. The superconducting quantum circuits group at the IQOQI Innsbruck has developed this fit routine using python. This routine fits the measured S parameters by dividing the whole process in subroutines that are successively passed. In the following, the effects of the measurement environment to a resonator are pointed out. This section is based on the master thesis by D. Zöpfl [28] where more detailed information can be found.

Environmental effects can occur in the form of an additional attenuation a, a phase shift α or a cable delay τ. This modifies Eq. (2.33) to

$$S'_{21} = \left(ae^{i\alpha}e^{-2\pi i f\tau}\right)\left(1 - \frac{Q_l/Q_c}{1+2iQ_l\frac{f-f'_r}{f'_r}}\right). \tag{2.34}$$

The added term in front respects the attenuation and phase shift by $ae^{i\alpha}$ and the cable delay by $e^{-2\pi i f\tau}$. Since the path is the same the signal has to take with or without a cable delay, S_{21} increases linearly in frequency. The effect of the delay is roughly sketched in Fig. 2.6a. The additional phase shift leads to a rotation of the measured S parameter in the complex plane while the diameter of the circle scales with the attenuation. This is shown in Fig. 2.6b after the cable delay has been removed.

Before the actual fit routine is applied, the linear background of the transmission line amplitude is subtracted. This enhances the stability of the fit. Fig. 2.6a to Fig. 2.6d present a survey on how the environmental effects to the S parameter are subsequently corrected.

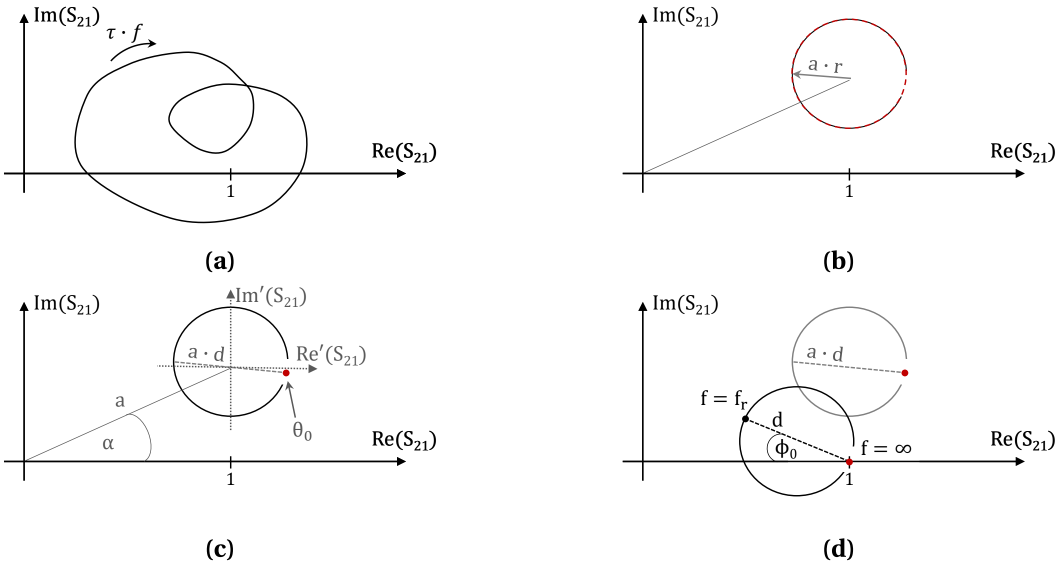

Figure 2.6: Steps of the circle fit routine: The influence of the environment is respected in four steps subsequently: (a) Effects of the cable delay, (b) subtraction of the delay and fitting of the circle, (c) circle normalisation, and (d) circle with removed environmental effects. More details in the text. Figure adapted from D. Zöpfl [28].

Subtraction of the Cable delay

The effects of the cable delay appear as a linear slope to the phase. This is shown exemplarily in Fig. 2.7. After the delay has been corrected, a circle can be fitted to the data. For this, an algebraic fit is employed that does need no initial parameters and reduces the problem to an eigenvalue problem. From the non-normalized circle, the diameter d' and centre-point can be extracted.

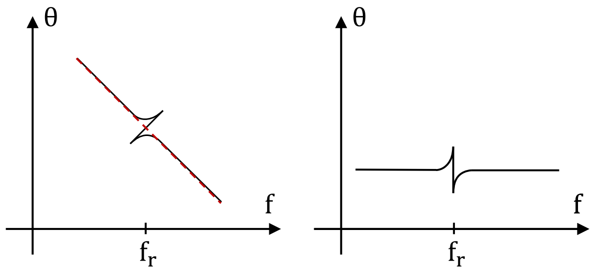

Figure 2.7: Subtracting the cable delay: The delay adds a linear slope to the phase (left) that is corrected using a linear fit (right). Expect for the resonance at $f = f_r$, no frequency dependency is expected. Adapted from D. Zöpfl [28].

Determining the off-resonant point

The off-resonant point is extracted by transforming the coordinate system in the way the origin of the complex plane lies in the centre of the circle, see Fig. 2.6c. By fitting Eq. (2.35), the parameters f_r, Q_l and θ_0 are obtained where $\tan(\theta_0)$ is the resonant point.

$$\theta(f) = -\theta_0 + 2\arctan\left(2Q_l\left(1 - \frac{f}{f_r}\right)\right) \tag{2.35}$$

Since the off-resonant point lies opposite to the resonant point, the argument of the off-resonant point is $\theta_\infty = \theta_0 + \pi$. Knowing the absolute position of θ_∞ and the shift of the coordinate system, the attenuation a and phase shift α can be determined since the circle diameter is known from the previous step, $d' = 2a \cdot r$. The frequency f_r and Q_l obtained in this step are not used as results. This is because the fit according to Eq. (2.35) is very sensitive to noise, so the fitted values for f_r and Q_l are not robust. Both parameters get extracted in the fourth step of the routine.

Normalization

Because the circle has already been fitted in the first step, it only has to be normalized. This is done by compensating the phase shift α and dividing the radius by a. Finally, the phase shift caused by the impedance mismatch is given by

$$\sin(\phi_0) = \frac{y_c}{r} \,. \tag{2.36}$$

Here, y_c equals the y-coordinate of the centre-point.

Determining Q_l and f_r

As explained in the second step, Q_l and f_r can be obtained by fitting Eq. (2.35) to the phase. However, the hereby extracted values for Q_l and f_r are not robust. Therefore, Q_l and f_r are extracted by a fit to the magnitude of the S parameter because it is more stable and provides the same information.

Determining Q_c and Q_i

At this point, every fitted parameter is known. The coupling and internal Q factors then can be determined using to Eq. (2.5) whereas Q_c is linked via the real part to Q_l by

$$Q_c^{Re} = \frac{Q_l}{d \cdot \cos(\phi_0)} \,. \tag{2.37}$$

The circle fit routine is now complete and all values describing the measured data are known.

Chapter 3
Theory on Granular Aluminium

Granular aluminium provides interesting properties that are desirable for designing superconducting quantum circuits. It features not only an enhanced critical field and critical temperature but also a high intrinsic impedance that relies on its grain-like structure. After a brief introduction to superconductivity, the second section of this chapter discusses the benefits of a high-impedance circuit. An impedance larger than the resistance quantum contributes to low charge fluctuations which are advantageous to realize charge qubits. The last section of this chapter presents a model of the electrodynamics in granular aluminium.

3.1 General on Superconductivity

Superconductivity is a macroscopic quantum state certain materials reach under specific circumstances. The state is described by a wave function with phase $\chi\left(\mathbf{r},t\right)$ that is coherent on a length χ_0 and an amplitude given by the electron density $\Psi_0\left(\mathbf{r},t\right)=\sqrt{n_s\left(\mathbf{r},t\right)}$:

$$\Psi\left(\mathbf{r},t\right)=\Psi_0\left(\mathbf{r},t\right)e^{i\chi\left(\mathbf{r},t\right)}\,. \tag{3.1}$$

In general, these circumstances are defined by a certain temperature T_c and external magnetic fields that do not exceed a certain strength B_c. Then, the electrons in the material condense into the superconducting state, showing several unique properties [36]: The electrical resistance of the material almost vanishes while the conductivity reaches infinity. The electrons couple weakly via a phonon to a bosonic state, forming a so-called Cooper pair [37]. In an external magnetic field, the so-called supercurrent $\mathbf{J_s}$, given by Eq. (3.2) arises in the material, shielding every magnetic field below certain strengths and leading to perfect diamagnetism (Meissner effect).

$$\begin{aligned}\mathbf{J_s}(\mathbf{r},t)&=2e\mathrm{Re}\left[\Psi^\star\left(\frac{\hbar}{m_s i}\nabla-\frac{2e}{m_s}\mathbf{A}(\mathbf{r},t)\right)\Psi\right]\\&=\frac{2en_s\hbar}{m_s}\left(\nabla\chi\left(\mathbf{r},t\right)-\frac{2\pi}{\Phi_0}\mathbf{A}(\mathbf{r},t)\right)\,.\end{aligned} \tag{3.2}$$

In Eq. (3.2), $2e$ is the charge of a Cooper pair with mass m_s, and $\Phi_0 = h/2e$ denotes the flux quantum. The vector potential is $\mathbf{B}(\mathbf{r},t) = \nabla \times \mathbf{A}(\mathbf{r},t)$. However, if the external magnetic field exceeds B_c, the superconducting state collapses. Depending on the collapse mechanism, one distinguishes between two types of superconductors (SC) [38]: Type I SCs collapse at a magnetic field strength B_c while type II SCs allow the field to penetrate the material in the form of flux hoses until the state collapses at a value $B_{c,2}$. In general, $B_c < B_{c,2}$, for which reason type II superconductors endure higher fields. Granular aluminium can be assigned to the type II superconductors with critical field strengths of up to 3.6 T [18].

A Pseudogap Superconductor

According to BCS theory (named after J. Bardeen, L. N. Cooper, and J. R. Schrieffer) [36], in a superconducting condensate, all states up to an energy $\Delta = 1.764 k_B T_c$ below the Fermi energy are occupied. The states between the superconducting gap 2Δ are suppressed, shown in Fig. 3.1a.

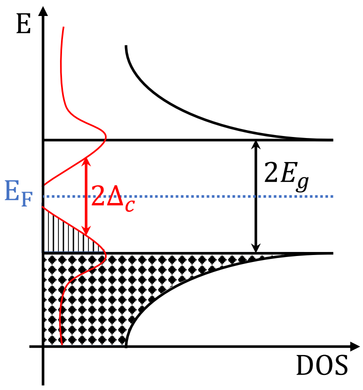

(a)

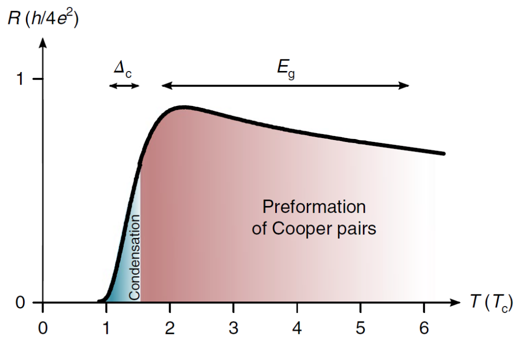

(b)

Figure 3.1: (a) Density of states (DOS) of a normal superconductor (black curve) and a pseudogap one (red curve): In the normal SC, all states are occupied up to the Fermi-energy E_F (shaded area) and no states exist in between the superconducting gap 2Δ whereas theses states get observed for a pseudogap SC. (b) Two-step transition to superconductivity: Pseudogap SCs feature a high T_c, which origin relies on the preformation of Cooper pairs at $T^\star > T_c$, leading to the observation of two energy gaps, E_g and Δ_c. Figure taken from Dubouchet et al. [39]

However, this theory cannot explain superconductivity in disordered SCs like granular aluminium consistently [40]. In SCs of this type, electrons pair up to preformatted Cooper pairs already at a temperature $T^\star > T_c$, leading to a second energy gap Δ_p (*pairing gap*) that can be experimentally observed [39]. This energy gap is also called 'pseudogap' because it is not isotropically distributed in the material [41]. At T_c, the electrons of the material then condense into the phase-coherent superconducting state with an energy gap Δ_c (*collective gap*), and the pseudogap evolves into a hard gap E_g. Fig. 3.1b illustrates the transition to superconductivity for such a SC. The two energy gaps of granular aluminium have been experimentally proven by Andreev spectroscopy [39].

Josephson Effect

The existence of Cooper pairs has been experimentally proven [37] in superconductor-insulator-superconductor structures, so-called Josephson junctions (JJ), by measuring the I-V-curve of this structure, shown in Fig. 3.2a. A schematic drawing of a JJ is seen in Fig. 3.2b. Since the Cooper pairs cannot exist in the non-superconducting layer, they tunnel through the barrier, leading to a measurable current I_J with amplitude I_c (first Josephson equation):

$$I_J = I_c \sin(\varphi) \tag{3.3}$$

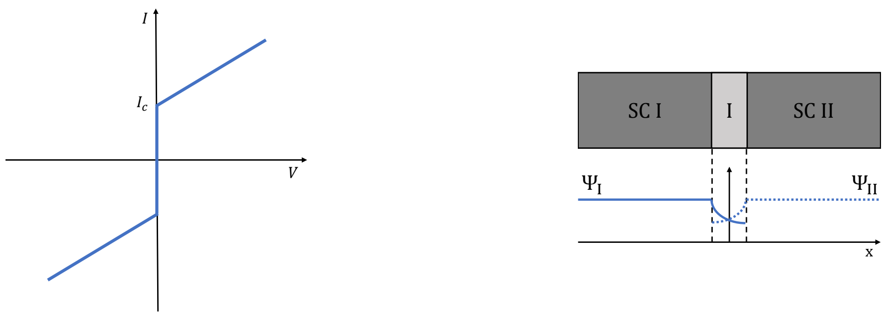

(a) (b)

Figure 3.2: (a) I-V-Curve: An external current below the critical value I_c leads to no voltage difference. Currents above this value cause a potential difference because it breaks apart Cooper pairs which tunnel through the junction. (b) Josephson Junction: Two superconductors (SC I, SC II, dark grey) are contacted via an insulating layer (I, light grey). The Cooper pairs in SC I tunnel through the barrier in SC II, leading to interference between the two wave functions with phases χ_1 and χ_2. Since the superconducting state cannot exist in the insulator, the wave functions Ψ_{I}, Ψ_{II} decrease exponentially.

The current I_J depends on the phase difference $\varphi = \chi_2 - \chi_1$ between the wave functions of the two SCs. The phase difference depends on the potential difference ΔV between the two superconductors (second Josephson equation):

$$\frac{\partial \varphi}{\partial t} = \frac{2\pi}{\Phi_0} \Delta V \, . \tag{3.4}$$

The critical current, I_c, represents the maximal current that can flow through the junction before Cooper pairs will break apart. For currents below this value, no voltage difference is observed. However, a current exceeding I_c will break up a proportion of Cooper pairs tunnelling, causing a potential difference. This mechanism leads to the observed I-V-curve shown in Fig. 3.2a.

3.2 Kinetic Inductance

The inductance of a resonant circuit that consists of a geometrical and kinetic part, L_g and L_{kin}, determines the microwave properties of the circuit. Especially, materials of high inductance like granular aluminium are interesting for building superconducting quantum circuits because they provide a large impedance that contributes to small charge fluctuations as will become clear in this section.

In general, the inductance L is defined by the relation of magnetic flux and current:

$$\Phi = L \cdot I \ . \tag{3.5}$$

For a superconducting two-dimensional wire, L_{kin} is given by [38]

$$L_{\text{kin}} = \frac{m_e}{n_s e^2} N \ . \tag{3.6}$$

Here, m_e is the electron mass, e the elementary charge, n_s the superconducting charge carrier density and $N = l/w$, the length to width ratio of the wire. According to BCS theory, the total kinetic inductance for a superconducting wire is given by

$$L_{\text{kin,tot}} = N L_{\text{kin}}^{\square} = N \frac{1}{1.76\pi} \frac{\hbar}{k_B T_c} \frac{\rho}{t} \ . \tag{3.7}$$

Here, $L_{\text{kin}}^{\square}$ is the kinetic sheet inductance of the wire. The factor $1/1.76 = \pi/(2k)$ respects the deviation of resistances below 10 mK from room temperature measurements and $k = 0.87$ is a correction factor [42]. By this relation, the kinetic (sheet) inductance is linked to the room temperature resistivity $\rho = R_s \cdot t$ of the wire (R_s is the sheet resistance and t the thickness of the wire). Eq. (3.7) is valid for $T \ll T_c$ and superconductors with a coherence length exceeding the mean free path, $l \ll \chi_0$, (local limit) which is true for grAl [17][43].

As discussed earlier, the inductance influences the impedance of a LC circuit increasingly. The impedance again determines the flux and charge fluctuations $\delta\Phi$ and δq that again contribute to the total inductive and capacitive energy of the circuit, $\delta q/2C$ and $\delta\Phi/2L$. The charge and flux fluctuations are given by [16]

$$\delta q = 2e \sqrt{\frac{1}{4\pi} R_q / Z_0} \tag{3.8}$$

$$\delta\Phi = \Phi_0 \sqrt{\frac{1}{4\pi} Z_0 / R_q} \ . \tag{3.9}$$

The flux quantum is $\Phi_0 = h/2e \simeq 2.0x10^{15}$ Wb and the resistance quantum is $R_q = h/(2e)^2 \simeq 6.5\,\text{k}\Omega$. Therefore, low impedance resonators with $Z_0 < R_q$ keep the flux localized in the inductance while high-impedance resonators with $Z_0 > R_q$ localize the charge on the capacitor. Consequently, small charge fluctuations that are desired for building charge qubits are only possible with high-impedance devices. Granular aluminium features such a high kinetic inductance ($Z_0 > R_q$) due to its structure of Josephson coupled superconducting grains: In the superconducting state, Cooper pairs tunnel through the insulating barriers of AlO_x which limits the number of tunnelling charges. The current decreases and consequently the (kinetic) inductance increases since the magnetic flux needs to be conserved, Eq. (3.5). The total kinetic inductance of a film made from granular aluminium is the sum of all Josephson inductances [43]. A film made of granular aluminium with a room temperature resistivity of 4000 µΩ cm features a critical temperature of $T_c = 2.2$ K which results in a 8×10^3 higher kinetic inductance as a geometric equivalent film made from conventional aluminium [17].

3.3 Superconductivity in Granular Aluminium

Although, granular superconductors are subject to research since the 1960s a complete model that explains the rich properties of grAl consistently, for instance, the high T_c, B_c and large kinetic inductance, does not exist yet [19]. Therefore, this section will only present a summary of what is known today. The discussion is based on the work of Levy-Bertrand et al [40].

As a first approach, one can describe the material as superconducting nanograins (made from aluminium), surrounded by insulating matter (made from aluminium oxide) and the grains being Josephson coupled. The ratio Δ/T_c gives the coupling strength. The electrons have to overcome the Coulomb barrier of energy E_c between the grains to tunnel through the material. The coherence of the phase through the grains is represented by the phase stiffness J. Experimentally, J is estimated in two ways, $J_\Delta = \frac{\hbar}{4e^2}\frac{\pi\Delta}{R_s}$ and L_{kin}, $J_{L_k} = \frac{\hbar^2}{4e^2 L_{\text{kin}}}$. The energy gap is Δ, L_{kin} is the kinetic inductance and R_s is the surface resistance. Primarily, the relation of superconducting and insulating material influences the electronic transport, conducting and microwave properties [43][44].

Based on the room temperature resistivity ρ, one can distinguish the properties of grAl in three regimes. The phase diagram in Fig. 3.3 summarizes the behaviour.
For small values, $\rho \leq 100\,\mu\Omega \cdot$ cm, the superconducting phase is coherent through all grains. This is also visible in the energy scales: The phase stiffness J exceeds E_c, indicating a strong phase coherence. In this regime, the critical temperature already reaches values above the value of bulk aluminium ($T_{c,\text{Al}} = 1.2$ K) [45]. The coupling strength is $\Delta/T_c = 1.78k_B$, comparable to BCS theory and close to the bulk value of $1.8k_B$, indicating a moderate coupling strength.
The maximal $T_c = 2.17$ K is reached in the next regime, $100\,\mu\Omega \cdot \text{cm} \leq \rho \leq 1000\,\mu\Omega \cdot$ cm, at $\rho = 160\,\mu\Omega \cdot$ cm to $\rho = 220\,\mu\Omega \cdot$ cm. With J lying in the order of E_c, the coherence of the phase is still given, and the grain coupling strength is comparable to conventional bulk aluminium,

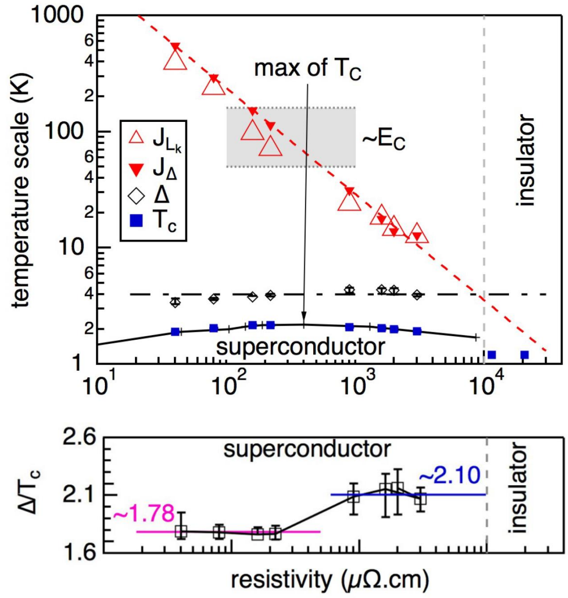

Figure 3.3: *Top panel:* Phase diagram: Based on the room temperature resistivity ρ, three regimes can be indicated: $\rho \leq 100\,\mu\Omega\cdot\text{cm}$, $100\,\mu\Omega\cdot\text{cm} \leq \rho \leq 1000\,\mu\Omega\cdot\text{cm}$, $\rho > 10^4\mu\Omega\cdot\text{cm}$. The regimes are described by the phase stiffness J (approximated by $J_\Delta = \hbar/(4e^2)\cdot(\pi\Delta)/(R_s)$ and $J_{L_k} = \hbar^2/(4e^2 L_{\text{kin}})$), the Coulomb energy E_c and the energy gap Δ. The maximal T_c is reached for $\rho = 220\,\mu\Omega\cdot\text{cm}$. *Bottom panel:* Coupling strength Δ/Tc as a function of resistivity. To the left of the maximal T_c, the coupling strength corresponds to a value comparable to BCS theory ($1.78\;k_B$) and increases to $2.10\;k_B$ for higher resistivity. Figure taken from Levy-Bertrand et al [40].

$\Delta/T_c = 1.8k_B$.

For $\rho > 10^4\;\mu\Omega\cdot\text{cm}$, J falls below the Coulomb energy: The phase coherence weakens due to fluctuations and the superconducting state is progressively suppressed. The grain coupling is increased, $\Delta/T_c = 2.10k_B$, leading to a lower critical temperature, indicating that the film has a strong disorder. While BCS theory fits the properties of films with resistivity in the first and second regime so far, it cannot describe grAl consistently in this regime. When ρ increases further, the film turns insulating. The electrons then localise due to the Coulomb blockade [40].

3.4 Electrodynamic Model

This section introduces a model for describing the electrodynamics in granular aluminium, resulting in an expression for the dispersion relation of it. The content and model have been originally derived by N. Maleeva et al. [17]

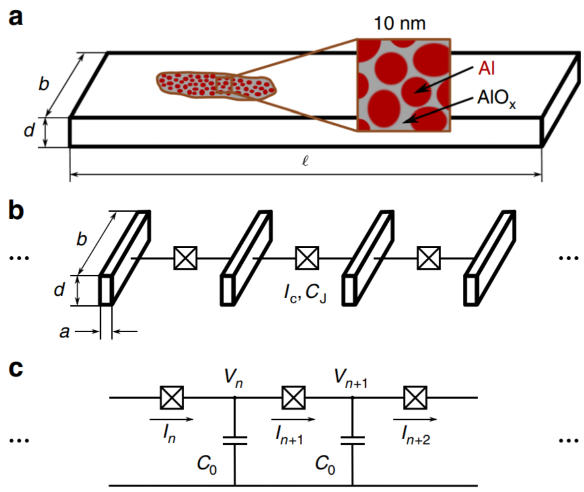

Figure 3.4: Electrodynamic model: (a) Sketch of a stripline made from granular aluminium with length l, width b and thickness d. The insert shows the material structure. (b) The structure is modelled as a 1-D network of effective Josephson junctions with critical current I_c and junction capacitance C_J. (c) Equivalent circuit of the considered model: chain of cells with each containing one Josephson junction with self-capacitance C_0, current I_n and voltage V_n. The current goes in the x-direction along the resonator. Figure taken from N. Maleeva et al. [17]

The structure of granular aluminium is similar to an array of Josephson junctions since the superconducting grains are connected via an insulating oxide barrier. Therefore, one can model the system as an effective network of Josephson junctions shown in Fig. 3.4.

In a homogeneous film (Fig. 3.4a,b) of width b and thickness d the superconducting grains (diameter a) have a self-capacitance C_0 and are connected to effective Josephson junctions with critical current I_c and capacitance C_J (Fig. 3.4c). The phase and voltage of the nth junction are given by χ_n and V_n, respectively. To calculate the dispersion relation of the system, the equation of motion for the phase difference $\varphi_n = \chi_{n+1} - \chi_n$ will be derived, starting with the Kirchhoff laws and the Josephson equations for two neighbouring junctions:

$$I_n = I_{n+1} + C_0 \frac{dV_n}{dt} \tag{3.10}$$

$$V_{n+1} - V_n = \frac{\hbar}{2e} \frac{d(\chi_{n+1} - \chi_n)}{dt} . \tag{3.11}$$

Since the microstrip resonators are elongated structures, the following calculation is performed in the limit of one-dimensional current distributions along the stripline. Moreover, the current is assumed to be homogeneously distributed through the sample cross-section as the film thickness is much smaller than the magnetic field penetration depth, $\lambda_L = 0.4\,\mu\text{m}$ [17].

The next step is to introduce the external excitation $I_{\text{ext}}\cos(\omega t)$ to the mth cell. Combining this with Eq. (3.10) and (3.11) leads to

$$2\,I_{n+1} - I_{n+2} - I_n + \delta_{m,n} I_{\text{ext}} \cos(\omega t) = \frac{\hbar C_0}{2e}\frac{d^2\varphi_n}{dt^2}\,. \tag{3.12}$$

The current trough the nth JJ is given by the phase difference and time-varying voltage (first and second JJ equation):

$$I_n = I_c \sin(\varphi_n) + \frac{\hbar C_J}{2e}\frac{d^2\varphi_n}{dt^2}\,. \tag{3.13}$$

Substituting I_n in Eq. (3.12), an expression for the equation of motion for the phase difference in the discrete limit can be formulated:

$$\begin{aligned}
&2I_c \sin(\varphi_{n+1}) - I_c \sin(\varphi_{n+2}) - I_c \sin(\varphi_n) \\
&+ \frac{\hbar C_J}{2e}\frac{d^2}{dt^2}\left(2\varphi_{n+1} - \varphi_{n+2} - \varphi_n\right) \\
&+ \delta_{m,n} I_{\text{ext}} \cos(\omega t) = \frac{\hbar C_0}{2e}\frac{d^2\varphi_n}{dt^2}\,.
\end{aligned} \tag{3.14}$$

To obtain the dispersion relation for the resonator, Eq. (3.14) needs to be rewritten in the continuous limit. The current distribution is considered to be sinusoidal, $I(x,t) = I(t)\sin\left(\frac{\pi x}{l}\right)$. The corresponding phase difference is $\varphi(x,t) = \varphi(t)\sin\left(\frac{\pi x}{l}\right)$. Substituting these considerations and integrating along the resonator (x-direction), the equation of motion for the resonator is found to be

$$\frac{d^2\varphi(t)}{dt^2} + \frac{4e\tilde{I}_c}{\hbar\tilde{C}} J_1[\varphi(t)] = \frac{4e}{\hbar}\frac{1}{C_0 + \frac{\pi^2 a^2}{l^2} C_J}\frac{a}{l} I_{ext}\cos(\omega t)\;, \tag{3.15}$$

where $\tilde{I}_c$ is $\tilde{I}_c = I_c \frac{\pi^2 a^2}{l^2}$ and $\tilde{C} = C_0 + \frac{\pi^2 a^2}{l^2} C_J$. The Bessel function $J_1[\varphi(t)]$ is approximated to first order by $\varphi(t)/2$. Solving Eq. (3.15) and performing the calculation for all higher modes, the dispersion relation is obtained to be

$$\omega_n = \frac{na\pi}{l}\sqrt{\frac{2eI_c}{\hbar\left(C_0 + \frac{n^2\pi^2 a^2}{l^2} C_J\right)}}\,. \tag{3.16}$$

A plot of Eq. (3.16) is shown in Fig. 3.5. For the lowest mode, the dispersion behaves linearly with a slope $a\pi/l\sqrt{C_J/C_0}$ and saturates at the effective plasma frequency $\omega_p = \sqrt{2eI_c/\hbar C_J}$, shown in Fig. 3.5. The plasma frequency for granular aluminium films with a room temperature resistivity of 4000 μΩ · cm is $\omega_p \simeq 70$ GHz, several times lower than the plasma frequency for conventional aluminium that is 14×10^6 GHz [46].

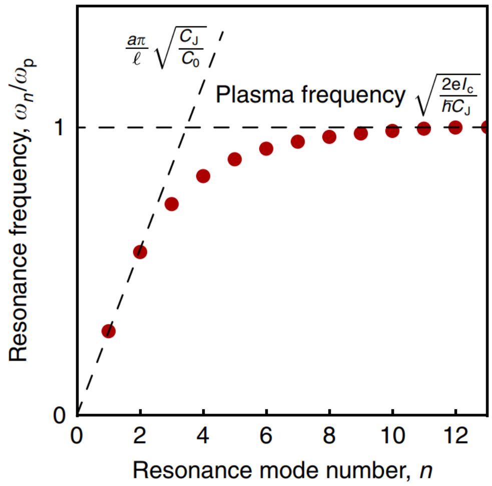

Figure 3.5: Dispersion relation of the electrodynamic model: The resonance frequency ω_n of mode n saturates at the plasma frequency ω_p and rises linearly for the lowest modes. Figure taken from N. Maleeva et al. [17]

3.5 Circuit Electrodynamics in Granular Aluminium

In the following, the circuit electrodynamic properties of grAl will be presented. Like the previous discussion, this section is also based on the work by N. Maleeva et al [17]. After defining the Hamiltonian, the self-Kerr and cross-Kerr coefficients will be derived.

In first-order approximation, the resonator modes can be described as a harmonic oscillator with non-linear properties related to the self-Kerr and cross-Kerr effect. The non-linearities occur since the resonator is modelled as a network of JJs. That means interactions between the fundamental mode with itself (self-Kerr, K_{nn}) and with higher modes (cross-Kerr, K_{nm}) exist. The corresponding Hamiltonian can be written in the familiar quantum optical form:

$$H = \hbar \sum_{n=1} \left(\omega_n + K_{nn} a_n^\dagger a_n\right) a_n^\dagger a_n + \hbar \sum_{\substack{n,m=1 \\ n\neq m}} \frac{K_{nm}}{2} a_n^\dagger a_n a_m^\dagger a_m \, . \tag{3.17}$$

The operators a_n and $a_n^\dagger$ are the lowering and raising operators.

self-Kerr coefficient

To derive the self-Kerr coefficient of the fundamental mode, the equation of motion for the resonator, Eq. (3.15), is expanded by a damping term with constant γ:

$$\ddot{\varphi} + \gamma\dot{\varphi} + \frac{4e\tilde{I}_c}{\hbar\tilde{C}} J_1\left[\varphi(t)\right] = \frac{4e}{\hbar\tilde{C}}\frac{a}{l} I_{ext}\cos(\omega t) \ . \tag{3.18}$$

Since the self-Kerr effect is only obtained at resonance, the drive is assumed to be near resonant. The system then only oscillates with the driving frequency ω, so the phase difference is

$$\varphi = \varphi_a \cos(\omega t + \delta) \ . \tag{3.19}$$

The amplitude response is φ_a and δ is the phase delay due to losses in the system. Applying this to Eq. (3.18) and expanding the Bessel function to third order, one obtains an expression for the amplitude

$$\varphi_a = \frac{\frac{4e}{\hbar\tilde{C}}\frac{a}{l} I_{\text{ext}}}{\sqrt{\left(\omega^2 - \omega_1^2\left(1 - \frac{3\varphi_a^2}{32}\right)\right)^2 + \gamma^2\omega^2}} \ . \tag{3.20}$$

Maximizing Eq. (3.20) for φ_a, one finds the resonance frequency to be

$$\omega = \omega_1\sqrt{1 - \frac{3\varphi_a^2}{32}} \approx \omega_1\left(1 - \frac{3\varphi_a^2}{64}\right) \ . \tag{3.21}$$

At this point, one can see that the non-linearity of the array is similar to the one of a single JJ, $\omega = \omega_1\left(1 - \frac{\varphi_a^2}{4}\right)$, but has a lower first order non-linearity. At resonance, φ_a reaches its maximal value given by

$$\varphi_a = \frac{2\pi}{\Phi_0} I_{\text{res}} L_J \ . \tag{3.22}$$

Here, $I_{\text{res}} = \sqrt{2\pi\frac{a}{l}\hbar\omega_1\bar{N}/L_J}$ is the amplitude of the current circulating in the resonator and $L_J = \hbar/(2eI_c)$ is the Josephson inductance of a single junction. Φ_0 is the magnetic flux quantum, and $\bar{N}$ is the average photon number in the resonator. The square of φ_a is correlated to the average photon number in the resonator and given by

$$\varphi_a^2 = 4\pi e a \frac{\omega_1}{I_c V_{\text{grAl}}} \bar{N} \ . \tag{3.23}$$

Note that $j_c = I_c/(bd)$ and $V_{\mathrm{grAL}} = bdl$ is the film volume. Substituting this expression in Eq. (3.21), one obtains

$$\omega = \omega_1 - \frac{3}{16}\frac{\pi e \omega_1^2}{I_c}\frac{a}{l}\bar{N} = \omega_1 - K_{11}\bar{N} \,. \tag{3.24}$$

The self-Kerr coefficient of the fundamental mode is given by

$$K_{11} = \frac{3}{16}\pi e a \frac{\omega_1^2}{j_c V_{grAl}} \,. \tag{3.25}$$

cross-Kerr coefficient

For the derivation of the cross-Kerr coefficient, the modes m and k with eigenfrequencies ω_a and ω_b are considered. Similar to the derivation of the self-Kerr coefficient, one starts with the equation of motion in the continuous limit expanded by a drive, $I_m \cos(\omega_a t) + I_k \cos(\omega_b t)$, on the mth and kth mode:

$$\begin{aligned} I_c a^2 \frac{d^2}{dx^2}\sin(\varphi(x,t)) + \frac{\hbar C_J}{2e} a^2 \frac{d^2}{dt^2}\frac{d^2}{dx^2}\varphi(x,t) \\ + a\delta\left(x - \frac{l}{2}\right)(I_m \cos(\omega_a t) + I_k \cos(\omega_b t)) \\ = \frac{\hbar C_0}{2e}\frac{d^2}{dt^2}\varphi(x,t) \,. \end{aligned} \tag{3.26}$$

I_m and I_k are the excitation amplitude on the mth and kth mode, respectively. In the following derivation, the interaction between the first and third mode will be investigated, so the phase is assumed to be

$$\varphi(x,t) = \varphi_1(t)\sin\left(\frac{\pi x}{l}\right) + \varphi_3(t)\sin\left(\frac{3\pi x}{l}\right) \,. \tag{3.27}$$

When using Eq. (3.27) and considering strong pumping of the first mode and weak probing of the third, Eq. 3.26 splits in a differential equation for each mode.

$$\frac{\hbar}{2e}\left(C_0 + \left(\frac{\pi a}{l}\right)^2\right)\ddot{\varphi}_1 + 2I_c\left(\frac{\pi a}{l}\right)^2 J_1[\varphi_1] = 2\frac{a}{l} I_1 \cos(\omega_a t) \tag{3.28}$$

$$\frac{\hbar}{2e}\left(C_0 + \left(\frac{3\pi a}{l}\right)^2\right)\ddot{\varphi}_3 + 2I_c\left(3\frac{\pi a}{l}\right)^2\left(1 - \frac{\varphi_1^2}{4}\right)\varphi_3 = 2\frac{a}{l} I_3 \cos(\omega_a t) \tag{3.29}$$

Eq. (3.28) looks similar to the differential equation of the self-Kerr coefficient, Eq. 3.18: Since the drive on the first mode is strong, it only contains self-Kerr non-linearities. Eq. (3.29), on the contrary, contains only cross-Kerr non-linearities. Analogue to the derivation of the self-Kerr coefficient, the drive is assumed to be in resonance and the phase response is

$$\varphi_3 = \varphi_b \cos(\omega t + \delta) \tag{3.30}$$

where φ_b is the phase amplitude of the third mode and δ being the delay due to losses. Again, the phase response is maximized for φ_b, yielding the resonance frequency to be

$$\omega = \omega_3 \sqrt{1 - \frac{\varphi_b^2}{8}} \approx \omega_3 \left(1 - \frac{\varphi_b^2}{16}\right) . \tag{3.31}$$

Since φ_b reaches its maximum in resonance analogous to φ_a, the φ_b is given by Eq. (3.23)

$$\varphi_b^2 = 4\pi e a \frac{\omega_1}{I_c V_{\text{grAl}}} \bar{N} . \tag{3.32}$$

Applying this to the above equation, it is found

$$\omega = \omega_3 - K_{13}\bar{N} = \omega_3 - \frac{1}{4}\pi e a \frac{\omega_1 \omega_3}{I_c V_{\text{grAl}}} \bar{N} . \tag{3.33}$$

The cross-Kerr coefficient between the first and third mode is given by

$$K_{13} = \frac{1}{4}\pi e a \frac{\omega_1 \omega_3}{j_c V_{grAl}} . \tag{3.34}$$

Expanding this procedure for the first and all other modes, the cross-Kerr coefficient is defined as

$$K_{1n} = \frac{1}{4}\pi e a \frac{\omega_1 \omega_n}{j_c V_{grAl}} . \tag{3.35}$$

Chapter 4
Fabrication Process and Design Consideration

In this chapter, the fabrication procedure and considerations of the resonator dimensions are presented. At first, an introduction to the developed simulation routine will be given. The simulations have been performed to figure out appropriate dimensions of the resonators that result in a coupling Q factor in the range of the internal one, which is in the order of 10^4 to 10^5. This ensures that the later fabricated resonators are well suited for the circle fit routine.
The second part of this chapter presents the fabrication procedure that is composed of two main steps: electron beam lithography and the deposition of aluminium in a pure oxygen atmosphere. For the film deposition, the commercial electron beam evaporator MEB 550S$^{\text{TM}}$ (*Plassys*) has been used. The deposition process has been investigated in detail regarding reproducibility and the variation of the process parameters, which are oxygen mass flow and growth rate. The sample position in the evaporator has been investigated as well.

4.1 Design Consideration

Finite element simulations have been done to determine the correct geometrical dimensions of resonators that result in eigenfrequencies above the waveguide cutoff frequency of 6 GHz. The coupling quality factors should be of the order of 10^4 to 10^5. The coupling Q factor and coupling rate are determined using the circle fit routine.
This section starts with some basic information on the simulation software used, HFSS, and the established simulation routine. Afterwards, the developed resonator designs are presented.

4.1.1 Finite Element Simulation

Ansys HFSS is a commercial finite element solver for electromagnetic fields at microwave frequencies in 3D structures. By solving Maxwell's equations, it calculates numerically the electric and magnetic fields contained by the object. For this, the object is divided into tetrahedral elements

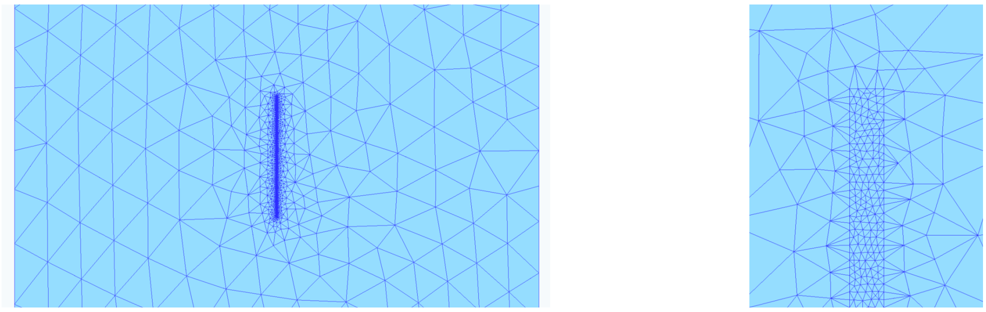

(a) **(b)**

Figure 4.1: Applying an appropriate mesh: (a) Mesh of a microstrip line on a substrate. (b) Closer look on the mesh of the microstrip. The mesh has a size four times smaller than the smallest size of each object. The resonator has a dimension of (10 × 450) µm.

with a local function, interrelating each other so that Maxwell's equation are satisfied across the network of finite elements. This network is known as the mesh. The fields are calculated by transforming Maxwell's equation into a matrix that is solved at every node of a tetrahedron. An appropriately sized mesh has to be assigned to achieve high accuracy in results. Although HFSS can assign the mesh automatically, the experience shows that more precise results are achieved when assigning it manually. However, the required computational capacity increases with the fineness of the mesh, so a compromise between the required computation power and result accuracy has to be found. By experience, good results are found when assigning each structure a mesh size four times smaller than the structures smallest length. Fig. 4.1a and 4.1b show the mesh structure exemplarily for a (10 × 450) µm microstrip line.

The software provides multiple simulation modes, the assignment of materials and different boundary conditions. In this thesis, the *Eigenmode* and the *Driven Modal* solver have been used primarily. The former one calculates the system eigenfrequency of first and higher orders. The latter one finds the system response when it is excited at a port with a swept frequency. In both modes, the entire system consisting of the waveguide, the substrate, and the resonator has been modelled using 3D boxes for the substrate and the waveguide. The microstrip resonator is presented by a 2D sheet to reduce the calculation time. In the Driven Modal mode, the substrate is placed off-centre the same way it is positioned in the experiment, see Fig. 4.2a. Note that in the Eigenmode solver the waveguide works as a 'vacuum box' that restricts the space the simulation is done in and is, therefore, sized small. By this, the box eigenfrequencies increase according to Eq. (1.36), preventing coupling between the box modes and that of the resonator. The model for the Eigenmode solver is shown in Fig. 4.2b. In both models, the substrate has a dimension of (2 × 13) mm corresponding to the actual size of the substrate that will be used for fabrication.

Further, both offer the possibility to visualize the electric and magnetic field, including vectorial plots, plots of the magnitude and the animation of the time evolution. The magnitude of the electric field of the system, including the substrate and resonator, is shown in Fig. 4.3 using the

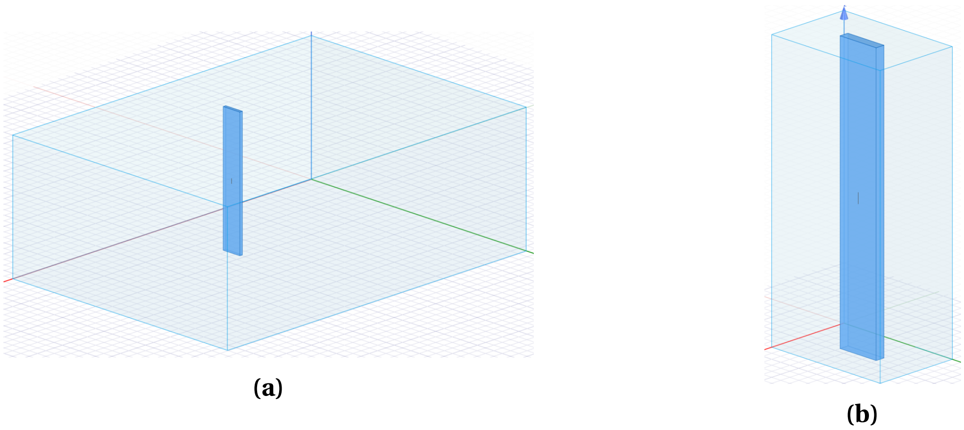

Figure 4.2: Different model designs: (a) Driven Modal solver: The box (transparent) surrounding the substrate (blue) that carries the microstrip resonator corresponds to the waveguide used in the experiment. (b) Eigenmode solver: The box is of small dimensions to restrict the space the calculation is executed in. More details in the text.

Driven Modal. The field propagating along the waveguide axis reaches a maximal value in the waveguide centre and decreases to a minimum at the walls. This agrees with Eq. (1.33) since the field magnitude is in space proportional to a sinusoidal function. The distance between the field maxima corresponds to the excitation wavelength. Note that the speed of light is reduced inside the waveguide according to $v_p = \omega/\beta$ (v_p is the phase velocity in the waveguide). The small asymmetry of the field is caused by the substrate as it has a higher dielectric constant and thus confines the field.

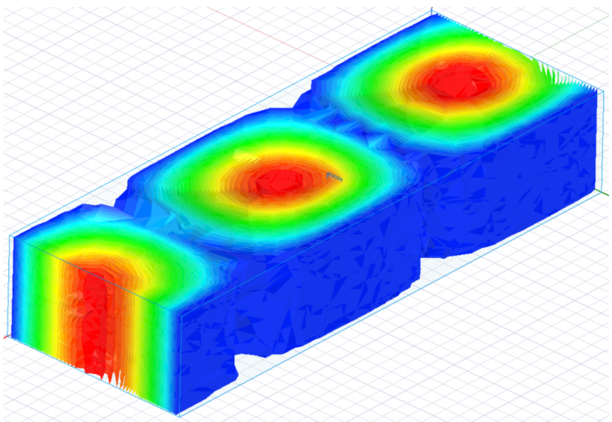

Figure 4.3: Magnitude of the electric field inside the waveguide: The field reaches a maximum in the centre of the waveguide axis and decreases to the walls. The substrate confines the field and leads to a small deformation of the field. Red colours indicate high values whereas blue colours indicate low values.

To correctly regard the high impedance of granular aluminium, in both modes the boundary condition *impedance* is used. Here, the resonator is assigned a certain reactance $X = 2\pi f L_{\mathrm{kin}}$ and zero resistance since it is superconducting. The kinetic sheet inductance is L_{kin}. The frequency f is a parameter that can adopt different values and should equal the solution frequency *Freq* to achieve a self-consistent solution. Since the Driven Modal treats an excited system, the solution of both modes is not consistent. The difference between the modes could be reduced by refining the mesh in the way mentioned above. By this, the differing has been reduced to $\sim$ 15 MHz ($\sim$ 0.2 %). After all, the solution of the Driven Modal is given more trust because the eigenfrequencies converged here faster on refining the mesh compared with the Eigenmode solver.

4.1.2 Simulation Routine

The simulation routine developed to find appropriate dimensions for resonators providing the desired properties (resonance $f_r > 6\,\text{GHz}$, $Q_c \sim 10^4$) consists of two main steps.
First, a survey of resonators with the same width but different lengths in a microwave regime of 6 GHz to 8 GHz is created. This is done using the Eigenmode solver and implementing the *impedance* boundary as described above and applying the tool *optimetrics*. This tool allows setting a parametric sweep. That means the resonator width is, e.g., $W = 20\,\mu\text{m}$ while the parametric frequency f and resonator length l are varied, solving the system for every value set. When f matches the system solution frequency $Freq$, the resonance f_r of a resonator with a particular length is found, so $f_r = Freq$. In Fig. 4.4, the result of this first step is plotted. The black markers show where f matches the solution frequency, indicating possible resonator geometries. As discussed in section 1.3.5, lower resonances are found for longer resonators, while short resonators result in a higher frequency. The error bars in Fig. 4.4 are point-sized.

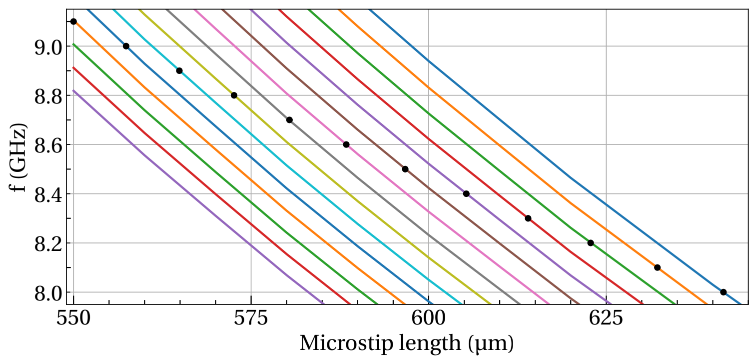

Figure 4.4: Overview: Using the Eigenmode solver, the length l of a microstrip resonator with a fixed width $W = 20\,\mu\text{m}$ is varied in a microwave regime from 8 GHz to 9 GHz. The black dots mark the points where the parametric frequency matches the solution frequency and a resonance is self-consistently found. These points indicate possible resonator geometries. Error bars are point-sized.

However, the obtained 'map' provides only a rough overview of geometries since it consists only of interconnected data points and no continuous data set. To refine the result and to apply the circle fit routine for determining Q_c, f_r and κ, the simulation is repeated for one selected resonator geometry in the Driven Modal. Because longer resonators result in a lower Q_c, Eq. (2.32), it is useful to choose a geometry of short length l. Again, the *impedance* boundary is employed; however, in the Driven Modal the solution frequency *Freq* can be used as parametric frequency f. So, the resonance can be found directly without the need for varying any parameter. In principle, one could find an appropriate resonator geometry by executing only this step. However, the interval in which the resonance frequency might be and in which the driving frequency has to change needs to be guessed. This can be bypassed when providing an overview as described in the first step.

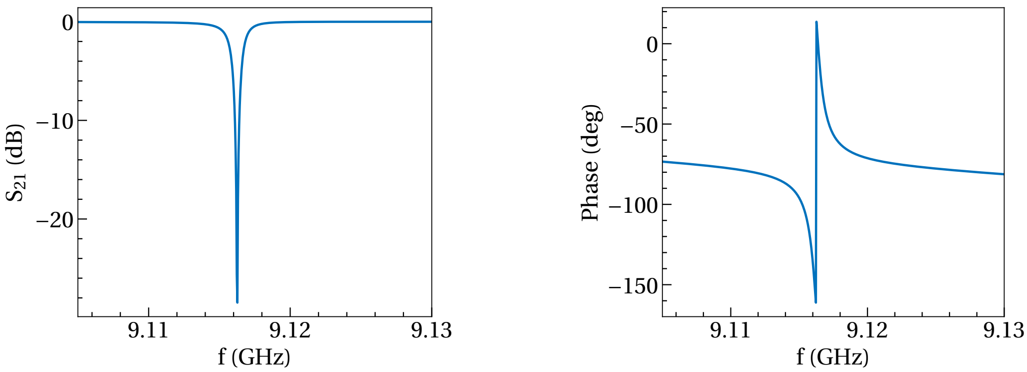

(a) **(b)**

Figure 4.5: Simulation of a (20 × 550) µm microstrip resonator on a sapphire substrate in Driven Modal: (a) The resonance appears in the form of a dip in the magnitude of the S_{21} parameter. (b) shows the corresponding phase.

Fig. 4.5 presents the resulting magnitude and phase following the second step. The resonance appears in the form of a dip in the magnitude of the S parameter and a modification of the phase. The solution from the Driven Modal differs from the result of the first step by $\sim$ 10 MHz. This is due to the inconsistency between the two solution modes and because the first step only offers a rough estimation. To achieve a higher resolution in the Driven Modal result, the steps of the driving frequency can be refined. Next, the circle fit routine is applied to the data to extract the coupling Q factor. The coupling rate is determined by $\kappa = 2\pi f_r / Q_c$.

4.1.3 Resonator Designs

4.1.3.1 Resonators for Characterizing Granular Aluminium

To characterize resonators made of granular aluminium, in total six designs of microstrip geometry have been developed, each sitting on a single sapphire substrate of size (2 × 13) mm. Additionally, the coupling property to a transmon qubit will be investigated in chapter 7. Each resonator is a large kinetic sheet inductance of $L_{\mathrm{kin}} = 2\,\mathrm{nH}$ assigned. By this, eigenfrequencies above 6 GHz are obtained already at resonators of lengths below 400 µm. Because the resonators will be fabricated using silicon substrates, see section 4.2.5, the simulation has been performed using silicon instead of sapphire as well.

Table 4.1: Simulation results using a sapphire and a silicon substrate: The table lists the fundamental mode f_r, the coupling Q factor Q_c and coupling rate κ.

Width × Length (µm)	Parameter	Sapphire	Silicon
	f_r (GHz)	7.137168(8)	6.593259(6)
10 × 550	Q_c	1.12(2)	0.895(13)
	$\kappa/2\pi$ (kHz)	635.0(14)	737(10)
	f_r (GHz)	7.660942(4)	7.076082(4)
8 × 460	Q_c	2.11(4)	1.7(3)
	$\kappa/2\pi$ (kHz)	363(6)	426(7)
	f_r (GHz)	8.1170167(8)	7.4962884(14)
5 × 350	Q_c	5.16(4)	4.3(5)
	$\kappa/2\pi$ (kHz)	157.2(13)	173(3)
	f_r (GHz)	8.20341(4)	7.580111(7)
20 × 625	Q_c	0.53(3)	0.593(5)
	$\kappa/2\pi$ (kHz)	1534(87)	1279(11)
	f_r (GHz)	8.466985(3)	7.8205617(20)
10 × 450	Q_c	2.03(3)	1.73(13)
	$\kappa/2\pi$ (kHz)	416(5)	452(3)
	f_r (GHz)	9.11627(3)	8.42081(2)
20 × 550	Q_c	0.77(4)	0.67(2)
	$\kappa/2\pi$ (kHz)	1185(70)	1256(42)

Tab. 4.1 lists the developed geometries for a sapphire substrate and for a silicon one. The resonators on sapphire lie in a frequency range of 7.0 GHz to 9.2 GHz while the frequency of the resonators simulated on a silicon substrate is shifted by $\sim$ 600 MHz. According to Eq. (1.38), the higher permittivity of silicon lowers the impedance of the microstrip resonator while increasing the capacitance ($C \propto \epsilon$), leading to lower resonances at the same geometry. The increased capacitance also explains the decrease in Q_c of the resonators involving a silicon substrate as Eq. (2.14) predicts.

As suggested in section 2.4, the coupling to the waveguide can be increased when tilting the resonator by an angle ϑ. Therefore, a simulation of this has been investigated. The simulation is done using the Driven Modal solver and modelling a microstrip of size (20 × 625) µm located at the centre of a sapphire substrate according to the previous description in section 4.1.1. Again, the *impedance* boundary is used, and a kinetic sheet inductance of 2 nH is assigned. By using a command for rotating the microstrip around its centre, the tilting angle can be varied using the tool *optimetrics* and solving the system for every angle. The coupling Q factor is extracted by applying the circle fit routine to the data. Fig. 4.6 shows the simulation results. The obtained Q_c increases inversely proportional to $\sin^2(\vartheta)$ as the result of the model derived in section 2.4 suggests. Error bars in Fig. 4.6 are point-sized.

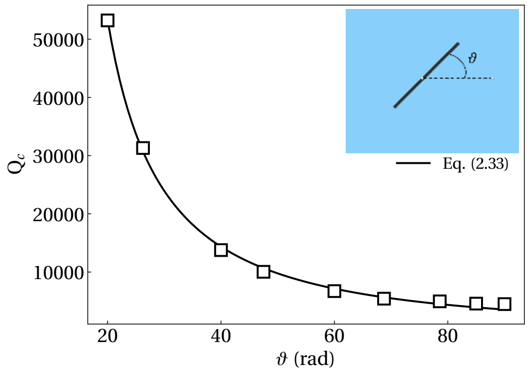

Figure 4.6: Coupling Q factor as function of the angle ϑ: Q_c increases proportionally to $\sin^{-2}(\vartheta)$. Note that ϑ is defined as the angle between the horizontal waveguide axis and the resonator. Error bars are point-sized.

In Fig. 4.7a, the magnitude of the electric field and surface current caused by a resonator of dimensions (8×460) µm on a sapphire substrate is presented. One can see that the field reaches a maximal value at the ends and to the centre of the microstrip while having a minimum in between. This corresponds to theory as discussed in section 1.2, so the microstrip equals a $\lambda/2$ resonator. The small asymmetry seen in the field magnitude is caused by the coupling to the waveguide. Fig. 4.7b presents the corresponding surface current. It behaves exactly opposite to the fields, fulfilling the theoretical expectations according to Eq. (1.19).

(a) **(b)**

Figure 4.7: (a) Magnitude of the electric field of a resonator with the dimensions (8×460) µm on a sapphire substrate. The field reaches a maximum at the ends of the microstrip while having a node in the centre, corresponding to a $\lambda/2$ resonator. (b) The surface current behaves exactly opposite to the field. Red colours indicate high values, whereas blue colours represent low ones.

4.1.3.2 U-shaped Microstrip Resonator

Besides the resonators to characterize the material grAl, another resonator design has been developed that will be investigated experimentally to test a design for a SQUID resonator. Fig. 4.8 illustrates a schematic drawing of this kind of resonator: The SQUID loop that is a superconducting circuit interrupted by two JJs [47] is added to the head structure of the resonator. The junctions are realized by separating two low-ohmic films with a high ohmic one, see the bottom insert in Fig. 4.8. In fabrication, these structures are achieved by two-angle deposition [48]. Details on this process can be found in section 4.2.1.

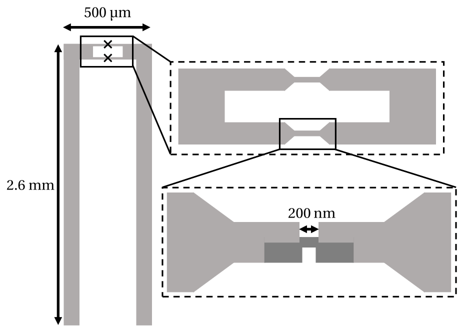

Figure 4.8: *From left to right*: U-shaped resonator of dimensions (50×5650) µm carrying a SQUID in its head structure. *Top insert*: Zoom on the SQUID loop. The two crosses indicate the Josephson junctions that interrupt the superconducting circuit. *Bottom insert*: The insulating tunnel barriers of a junction is created by two deposition films differing in resistivity (light grey: low-ohmic, dark grey: high-ohmic). Such structures are achieved by two-angle evaporation.

Therefore, the resonator investigated here will be made up of two films as well. For simulation, the resonator is modelled the same way as described in section 4.1.2, representing it by a single

Table 4.2: Resonance frequencies from the simulation of the U-shaped resonator: A kinetic sheet inductance between 20 pH to 30 pH results in resonances between 8.5 GHz and 9.3 GHz. The resonator has a dimensions of (50 × 5650) µm. The coupling Q factor is 7.92(7) × 10^4 in average and $\kappa/2\pi = 135.1(12)$ kHz.

$L_{\text{kin}}^{\square}$ (pH)	f_r (GHz)
20	9.2962020(11)
22	9.1342106(6)
24	8.9820365(4)
26	8.8365983(3)
28	8.6931676(3)
30	8.54890747(15)

rectangular sheet with a kinetic sheet inductance that corresponds to the average of both deposition layers. The resonator is assigned a low kinetic sheet inductance of 20 pH to 30 pH. This ensures that only the SQUID will be sensitive to external fields while the actual resonator is hardly affected. The eigenfrequency shall lie in the vicinity of 9 GHz. These conditions require the resonator to have a great length, so it is bent into U-shape as seen in Fig. 4.8. The total length of the resonator is 5650 µm and its width equals 50 µm. Tab. 4.2 lists the simulated resonances together with the corresponding kinetic sheet inductance. Resonances between 8.5 GHz and 9.3 GHz are achieved that decrease for the highest value of $L_{\text{kin}}^{\square} = 30$ pH. Q_c is on average $\langle Q_c \rangle = 7.92(7) \times 10^4$ and the average coupling rate is $\langle \kappa/2\pi \rangle = 135.1(12)$ kHz. In Fig. 4.9a the magnitude of the electric field caused by the resonator is shown. Similar to the resonators presented in section 4.1.3.1, the field reaches a maximal value at the ends of the resonator while having a minimum in between. By this, it corresponds to a $\lambda/2$-resonator. Again, the magnitude of the surface current shown in Fig. 4.9b behaves the opposite, according to theory. The small asymmetries can be traced back to the coupling to the waveguide.

(a) (b)

Figure 4.9: (a) Magnitude of the electric field and (b) surface current of the U-shaped resonator of dimensions (5650 × 50) µm. Red colours indicate high values, whereas blue colours represent low values. The electric filed reaches a maximum at the ends of the resonator while having a node in between ($\lambda/2$ resonator). The surface current behaves exactly opposite.

4.2 Fabrication

As mentioned at the beginning of this chapter, the fabrication process consists of two main steps, the electron lithography and the film deposition. Additional, steps like wafer cleaning, applying the photoresist, sample development and lift-off are necessary. Therefore, this section starts with a general overview of the whole procedure, followed by the characterisation of the deposition process in detail. In the end, details on the fabricated samples are given.

4.2.1 Sample Fabrication in General

To understand the sample fabrication in a better way, this section summarizes the individual steps: wafer cleaning, applying the photoresist, lithography and sample development, followed by film deposition and the lift-off. A schematic cartoon of the whole procedure is presented in Fig. 4.10. A detailed discussion of the evaporation process is given in section 4.2.2.

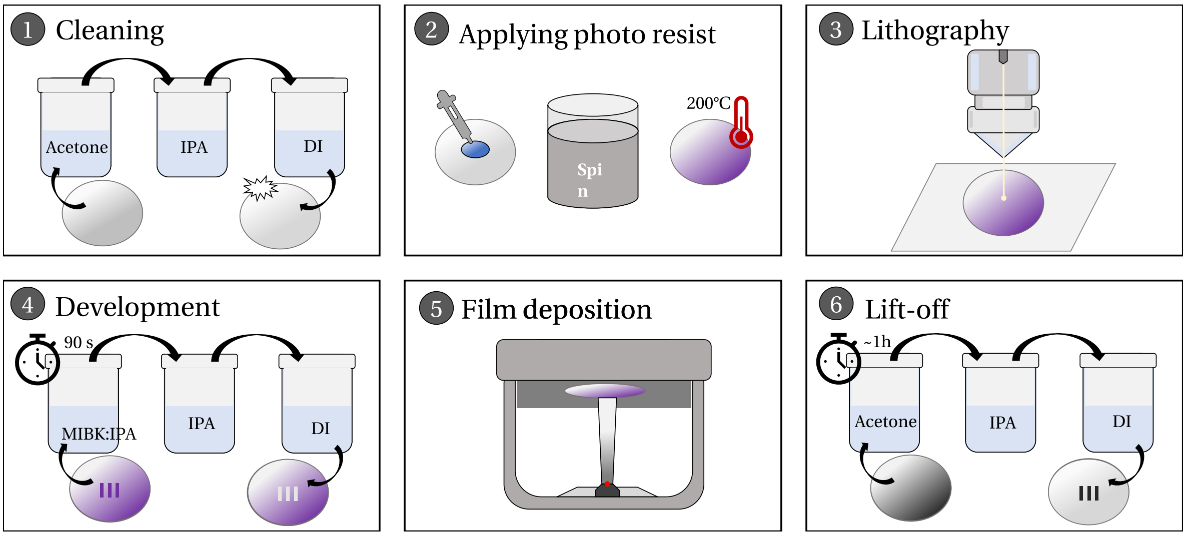

Figure 4.10: The fabrication procedure can be divided in six steps: wafer cleaning, applying photoresist, electron lithography, sample development, film deposition and lift-off. Details are given in the text.

Wafer cleaning: Each wafer has been wet chemically cleaned by going through different solvent baths: The first bath is in acetone while receiving an ultrasonication at 35 kHz for 15 min, so any leftovers of the wafer fabrication and other dirt are removed. Any acetone remains are washed away in an isopropanol (IPA) bath (ultrasonication at 35 kHz for 10 min.). To wash away the IPA, the wafer runs through a bath of deionized water (DIW) for 5 min (ultrasonication at 35 kHz). Last, the wafer is rinsed under DIW and blown dry using a N_2 gun. Every switch between the baths is done as fast as possible to prevent any dirt to dry out on the wafer surface.

Spinning off the photoresist: A photoresist by *MicroChem* consisting of polymer chains made from polymethyl methacrylate with a molecular weight of 950k is used. The chains are dissolved in anisole with a solid share of 4 % (950K PMMA A4). One layer of resist is spun on employing the LabSpin 6 by *Suss*. The wafer is rotated at a speed of 1000 RPM for a total of 100 s. According to *MicroChem*, these spin settings yield a photoresist thickness of about 400 nm [49]. Finally, the resist is hardened by baking the wafer on a hotplate at 200°C for 10 min.

Electron beam lithography: To create a pattern on the wafer the commercial lithography system eLine Plus by *RAITH* is employed. By radiating a high energy beam of electrons of a certain dose onto the resist, the polymer chains break up and their solubility changes. Afterwards, the broken chains are removed in the development step. An illustration of the so-called positive lithography is shown in Fig. 4.11. The scanning electron microscope (SEM) Sigma by *ZEISS* is used as beam source. The microscope additionally features two detectors (InLens Duo and SE2) for taking images of a sample surface. After aligning the electron beam and setting the focus onto the wafer surface, the surface is divided into an exposure grid made of so-called write fields. These write fields are stitched together, giving rise to the stitching error: When a pattern exceeds the size of a write field and the write fields are not properly aligned the final structure might be interrupted by a gap. An example of this error is shown in Fig. 4.12.
Each sample fabricated in this thesis has been exposed using a dose of 200 μC · cm^2, an acceleration voltage of 30 kV and a 120 μm sized aperture.

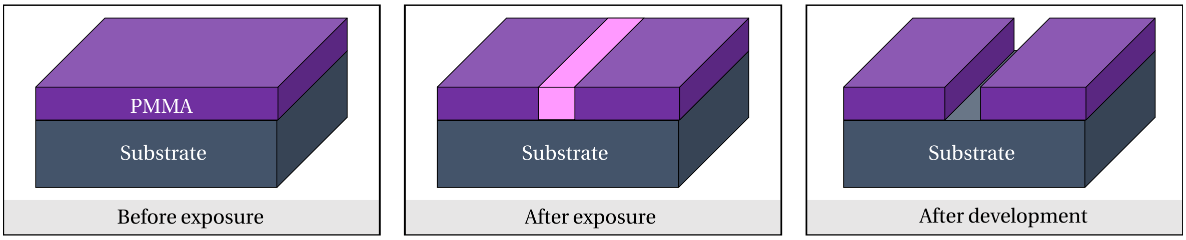

Figure 4.11: Positive lithography: The solubility of the photoresist (violette) is changed after the exposure (light pink). The exposed resist then can be washed away in the development step, leaving the non-exposed photoresist on the substrate surface (grey) behind. It remains a negative of the sample structure.

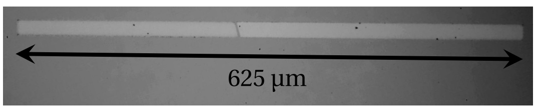

Figure 4.12: Stitching error: The picture shows a (20 × 625) μm microstrip on a silicon wafer. During the lithographic process, the wafer is divided into a grid of write fields. If these write fields are not properly aligned, the final structure might be interrupted by a gap. Picture taken using an optical microscope.

Development: After the exposure the broken up polymer chains are dissolved in a developer solvent made from methyl isobutyl ketone (MIBK) and IPA in a ratio of 1:3 for 90 s, yielding a high resolution in development [49]. The dissolving is stopped by an IPA bath. Finally, the sample is rinsed under DIW, blown dry and mounted into the evaporator machine.

Film deposition: In the deposition process, an electron gun heats an aluminium target. After letting in pure oxygen to the evaporation chamber, the evaporated aluminium formates grains on the wafer surface which are surrounded by aluminium oxide. To achieve films of certain resistivity, the evaporation rate and oxygen mass flow is adjusted. Details on the evaporation process are given in section 4.2.2. Moreover, it is possible to create multilayer structures: After depositing the first layer of film, the sample holder is tilted by a certain angle α. Because the photoresist layer now shades the sample surface partially, the second film deposited will cover only a certain area of the sample. A schematic representation of this process called shadow evaporation is shown in Fig. 4.13.

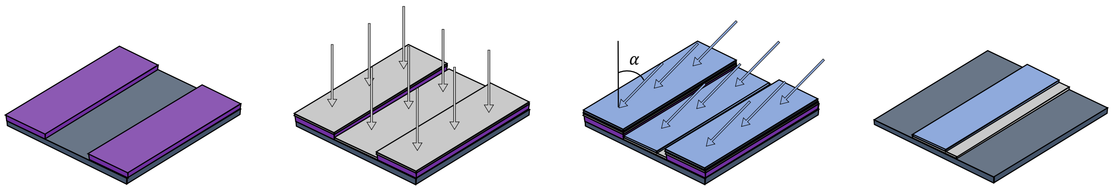

(a) (b) (c) (d)

Figure 4.13: Steps of the shadow deposition process: (a) Substrate (grey) after lithography. The remaining photoresist is coloured purple. (b) Deposition of the first film (light grey). (c) Before applying the second film (blue), the sample is tilted by an angle α. (d) Sample after lift-off: It remains a structure composed of two different deposition layers.

Lift-off: Since the film is covering the whole wafer that means the non-exposed photoresist and the cleared locations where the resist has been dissolved, it is necessary to get rid of the surplus film to win the actual structure. For this purpose, the wafer runs through an acetone bath. The acetone dissolves the non-exposed resist and the surplus of film on top of the resist is carried away. It remains the sample structure. For this, the wafer is kept in a tilted position in the acetone bath until only the sample structure remains. Finally, the wafer is rinsed under acetone to not let the wafer surface dry out and washed in IPA and DIW, successively.

Dicing: As multiple samples are fabricated on a single wafer, the wafer has to be cut to each sample. This is done with the support of the research group of I. Pop at the Karlsruhe Institute of Technology. Using a diamond saw, the wafer is cut into sections, obtaining each sample lying on a single substrate.

4.2.2 Aluminium Deposition in Oxygen Atmosphere

This section will discuss the film deposition process in detail. The employed machine Plassys MEB 550S^{TM} is introduced and the evaporation process is characterized. In general, films of granular aluminium are created by the deposition of aluminium oxide in ultra-high vacuum on to a substrate [19]. This can be done in a sputtering process using a reactive DC magnetron plasma and injecting an Al/O_2 mixture [43]. In this thesis, however, the films are fabricated by thermal evaporation of pure aluminium in an pure oxygen atmosphere using a commercial e-gun evaporation machine.

4.2.2.1 Electron Beam Evaporator MEB 550^{TM}

The evaporation machine features two chambers that can be independently vented from each other and are both evacuated by a pump providing an ultra-high vacuum about $\sim 1.0 \times 10^{-8}$ mbar. The bottom chamber is used for metal evaporation only while in the upper one the oxidation takes place. The top one also functions as load lock. Both chambers are separated by a motorized shutter. In Fig. 4.14, a CAD drawing of the machine is shown.

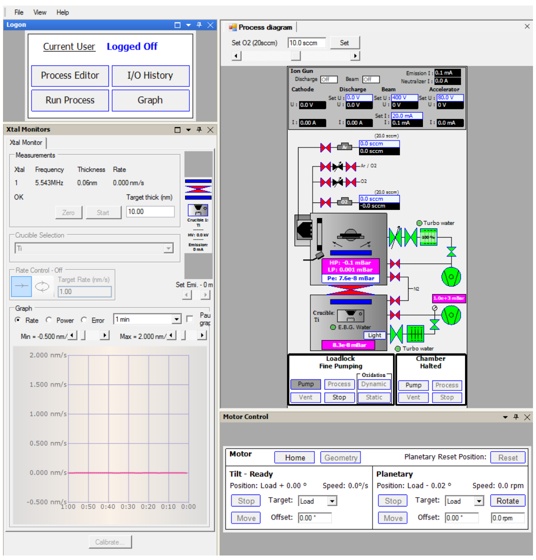

Figure 4.14: Screen shot of the user interface: The bottom left panel records the growth rate. The cartoon on the right contains all components of the machine, including pumps and vents that can be controlled manually.

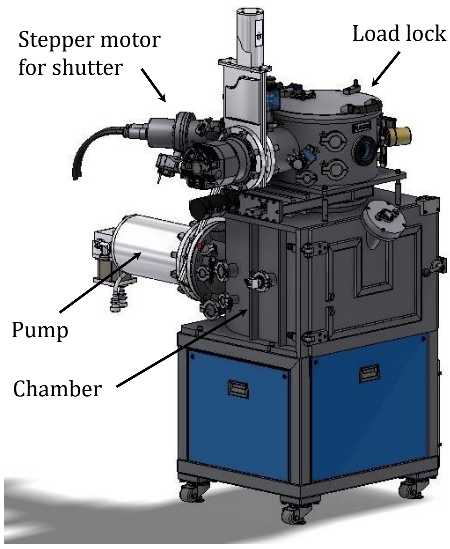

Figure 4.15: CAD drawing of the electron beam evaporator: The cylindrical top chamber (load lock) sits on the evaporation chamber. Details given in the text. Picture taken from the official Plassys website (www.plassys.com; accesed on: 23rd january 2019)

The metal evaporation chamber features an electron gun (*TELEMARK*) with a maximal power of 10 kW and a rotatable target table with crucibles of aluminium, titan and, niobium. The pattern the gun creates on the target surface can be customized. The load lock provides next to the circular sample holder an ion etching gun (*Kaufmann source*) and a supply of argon and O_2. The gun is used to create an Ar/O_2 plasma to remove PMMA leftovers and other impurities from the sample surface. For this, the sample holder can be tilted and rotated to bring the sample in position in front of the plasma gun. The Ar and O_2 flows are controlled each by mass flow controllers with a maximum flow rate of each 20 sccm.

The whole machine, starting with the pumps, the target selection and the electron gun, is controlled via a software with a user interface that is shown in Fig. 4.15. The software provides the possibility to create recipes for the evaporation process. A typical evaporation process starts with plasma etching the sample and a gettering process in which titanium is evaporated in the chamber with closed shutter. The titanium evaporation improves the vacuum. After this, the actual evaporation process takes place which is described in the following section.

4.2.2.2 The Deposition Recipe

Before presenting the results of the process characterization, the general deposition procedure will be pointed out. After cleaning the substrate, it is mounted to the evaporator and the following recipe is executed:

1. Pump load lock down to a pressure in the range of $P_{\mathrm{LL}} < 5 \times 10^{-7}$ mbar (about 3 hours)
2. Ion plasma etching for 2 minutes to descum any residuals: Ar/O_2 plasma made from 10 sccm Ar, 5 sccm O_2 at an accelerating voltage of 200 V and a current of 10 mA
3. Getter process: evaporation of titanium with a rate of 0.2 nm/s for 2 minutes to gather hydrogen and other residuals in the bottom chamber, enhancing the vacuum
4. Regulate aluminium evaporation rate n_{Rate} to the desired value within 2 minutes
5. Open oxygen vent and regulate to the certain flow f_{O2}
6. Wait for 15 s for rate stabilization
7. Open shutter between chamber and load lock
8. Deposit desired film thickness
9. Close shutter, stop oxygen flow and ramp down aluminium evaporation rate
10. Clean aluminium target by evaporation of 20 nm with a rate of 1.0 nm/s and closed shutter

Inertially, the shutter between the chamber and the load lock is closed. To create structures of multiple layers, step 4 to step 10 are repeated for each layer. The desired resistivity of each film is achieved by regulating to a certain evaporation rate and oxygen mass flow. If not mentioned separately, this recipe is used for every sample fabricated in this thesis. The evaporation process listed above is based on the work of Grünhaupt et al. [20]

The samples fabricated for the following investigation are produced on glass substrates of size 26 mm × 76 mm to save the more expensive sapphire or silicon wafers. The cleaning process of these consists of a 10 min ultrasonic bath in acteone at 35 kHz, followed by an IPA bath and ultrasonication for 5 min at 35 kHz and finally rinsing under DIW and blown dry. To determine the film resistivity of the sample, its surface is divided into sections of width w and length L to define a geometry for measuring the sample sheet resistance R, see Fig. 4.16. For the resistance measurement needles made from wolfram and a commercial multimeter are used. The determined resistance equals the average of multiple strips measured. Finally, the film sheet resistance R_s and resistivity ρ can be calculated according to $\rho = R_s \cdot t$ and $R_s = R \cdot w/L$ where t equals the film thickness.

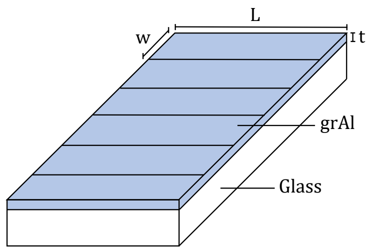

Figure 4.16: Defining a geometry to determine the sheet resistance: The film with thickness t (blue) is divided into strips of width w and length L on the glass substrate (white).

4.2.2.3 Testing the Reproducibility

Because the fabrication consists of several steps in total, a study on the reproducibility has been done. For this, five samples have been fabricated keeping all circumstances as equal as possible and comparing the film resistivity afterwards. The samples of each 20 nm thickenss have been fabricated following the process described in 4.2.2.2 with $f_{\mathrm{O2}} = 4.0$ sccm and $n_{\mathrm{Rate}} = 1.0\,\mathrm{nm/s}$. In Tab. 4.3, the oxygen partial pressures in the load lock and chamber, p_{LL} and p_{CH} that set after injecting $\mathrm{O_2}$ into the chamber and the determined resistivity ρ, are listed. The uncertainty in the partial pressures equals the accuracy of the measurement while the uncertainty in ρ corresponds to the standard deviation of the resistance measurement. The reproduction error of the total process has found to be 18 % (standard deviation). While the resistivity of samples #1, #2, #4 and #5 lie in close range to the average of $\langle\rho\rangle = 500(100)\,\mu\Omega\cdot\mathrm{cm}$, sample #3 differs from this value by

31 %. This is an indication of the sensitivity of the total fabrication procedure since it consists of multiple steps.

Table 4.3: Reproducibility study: Based on five samples fabricated keeping all circumstances as equal as possible ($f_{O2} = 4.0$ sccm, $n_{\mathrm{Rate}} = 1.0\,\mathrm{nm/s}$. 20 nm film thickness), the relative error in fabrication has found to be 18 %. The uncertainty of the pressures in the load lock and in the chamber p_{LL} and p_{CH} equals the measurement uncertainty of 0.1×10^{-5} (mbar).

	#1	#2	#3	#4	#5
ρ (μΩ · cm)	570(80)	550(50)	370(30)	640(160)	570(20)
$p_{\mathrm{LL}} \times 10^{-5}$ (mbar)	7.5	7.5	7.5	7.9	7.7
$p_{\mathrm{CH}} \times 10^{-5}$ (mbar)	1.5	1.0	1.0	1.2	1.1
$\langle\rho\rangle = 500(100)\,\mu\Omega\cdot\mathrm{cm}$					

4.2.2.4 Variation of Oxygen Mass Flow and Growth Rate

To gain understanding of the influence of the two deposition parameters, the oxygen mass flow f_{O2} and the evaporation rate n_{Rate}, on the film result a parameter variation has been done. In total, five samples have been fabricated to examine the influence of the oxygen mass flow and three additional samples for investigating the impact of the evaporation rate. Except for setting a certain evaporation rate and oxygen mass flow, the film deposition followed the routine described in section 4.2.2.2. Also, the determination of each film resistivity has been carried out as described there. For the flow variation, each sample has been fabricated using a fixed evaporation rate of 1.0 nm/s while setting an oxygen mass flow on a value between 4.0 sccm and 6.5 sccm. The samples for investigating the impact of the evaporation rate have been fabricated using a constant oxygen mass flow of 4.0 sccm and regulating n_{Rate} to a value between 0.7 nm/s and 1.2 nm/s. All films have a thickness of $t = 20$ nm.

In Fig. 4.17a and Fig. 4.17b the results are plotted on a logarithmic scale. As expected, the film resistivity increases with more oxygen mass flow since more oxygen enables the formation of more insulating oxide between the pure aluminium grains and, therefore, decreases the electron tunnel probability due to larger barriers. The result is a poorer conductivity. Also, the resistivity increases with decreasing the evaporation rate is expected. When the aluminium evaporates slowly, more time passes in which more oxide is formed on the sample surface. This leads to the same effect as increasing the oxygen mass flow. Error bars in Fig. 4.17a and Fig. 4.17b are point-sized. Since the measurement points in Fig. 4.17a and Fig. 4.17b almost lie on a straight line, a simple exponential fit ($\rho = \exp(m \cdot f_{O2} + b)$) is applied. A more complex fit that passes the origin ($\rho = A \cdot (\exp(m \cdot f_{O2} + b) - 1)$) would be more sophisticated, however, for this approach more data points are necessary.

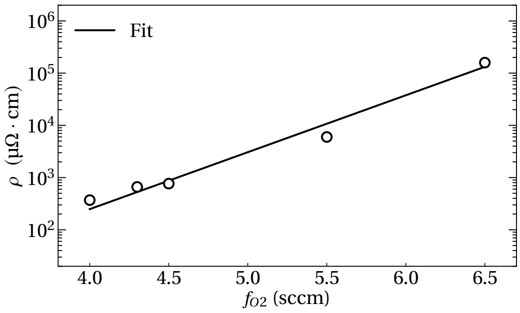

(a)

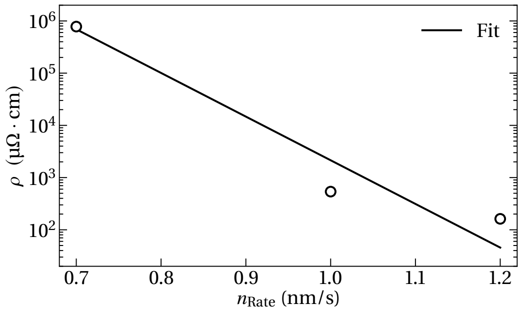

(b)

Figure 4.17: Parameter variation: The (a) oxygen mass flow f_{O2} and (b) evaporation rate n_{Rate} influence the film resistivity ρ in an exponentially way. The solid lines correspond to exponential fits. Error bars are point-size.

Additionally, some more observations have been made while fabrication:

Target level: A refilling of the target leads to a different value of the sheet resistance. That means, an almost full target causes lower resistive films while samples that have been fabricated using an almost empty target result in a higher film resistivity when keeping every other parameter the same. Fig. 4.18 shows a comparison of samples that have been fabricated using the same parameter set but different targets. The films have been evaporated on glass substrates. For every sample, the evaporation rate has been kept at $n_{\mathrm{Rate}} = 1.0$ nm/s while the oxygen mass flow has been regulated to different values. The difference in resistivity between the samples is noticeable and, moreover, increases with increasing the oxygen mass flow. Because the electron gun current adapts to the target level, the different gun currents cause a different evaporation temperature. Consequently, the oxidation happens differently. Error bars in Fig. 4.18 are point-sized.

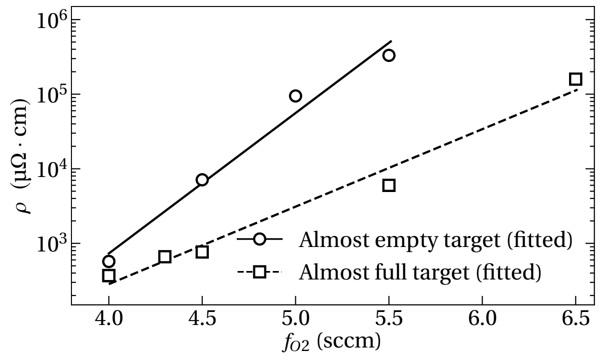

Figure 4.18: Impact of the target level: Comparison of samples that have been fabricated under the same circumstances but using different targets. Almost empty targets result in samples of high resistivity while an almost full target leads to a lower one. This is caused by a different oxidization depending on the electron gun current and target level. The samples have been fabricated using glass substrates and keeping an evaporation rate of $n_{\mathrm{Rate}} = 1.0$ nm/s. Solid lines correspond to exponential fits according to $\rho = \exp(m \cdot f_{O2} + b)$. Error bars are point-sized.

In conclusion, after a target refill a *calibration* of the film growth parameters (f_{O_2}, n_{Rate}) in the form like it has been done in this thesis is necessary to figure out the right values for fabricating films of certain resistivity.

Electron gun pattern: Different electron gun patterns have been tested. Since the pattern influences the stability of the evaporation rate strongly, it has a large impact on the film result. To ensure reproducibility, one should take care to stabilize the evaporation rate as much as possible. For example, a circular pattern causes the evaporation rate to oscillate and the rate is hard to be stabilized. Best results have been reached using an undefined dot-like pattern. Also, a rate of 1.0 nm/s could be stabilized best for which reason this rate has been chosen in the further fabrication process.

4.2.2.5 Spatial Distribution of the Resistivity

Since the valve for the oxygen supply is located laterally to the sample, a spatial gradient of the film sheet resistance has been suspected. In this section, an investigation of the spatial distribution of the resistivity is presented.

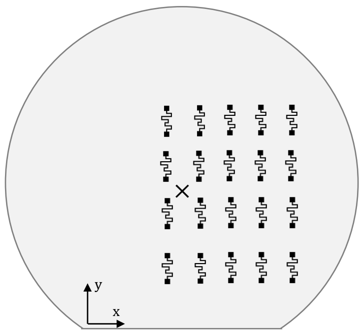

Figure 4.19: Sample matrix on a 2" wafer: To investigate the spatial distribution of the film resistivity on a wafer, a 4 × 5 matrix of meander structures has been fabricated on a silicon wafer. The black cross signs the wafer centre that corresponds to the origin of the coordinate system. Size not for scale.

For this purpose, a matrix of meander structures has been written on a single silicon wafer (*Si-Mat*, $\rho = 1 - 30\ \Omega{\cdot}\mathrm{cm}$, p-Typ, orientation: <100>). Fig. 4.19 shows the distribution of the samples on the wafer. In total, two wafers have been fabricated in this way by following the recipe given in section 4.2.2.2, so two films differing in resistivity are analysed. Contrary to the investigation of the glass substrates, a lift-off is necessary to determine the resistivity of each sample. This is done employing baths of acetone. Averaging over all samples, the first film results in a resistivity of 490 µΩ cm. For this,
$n_{\mathrm{Rate}} = 1.0\,\mathrm{nm/s}$ and $f_{O2} = 4.0$ sccm has been used. The average resistivity of the second film

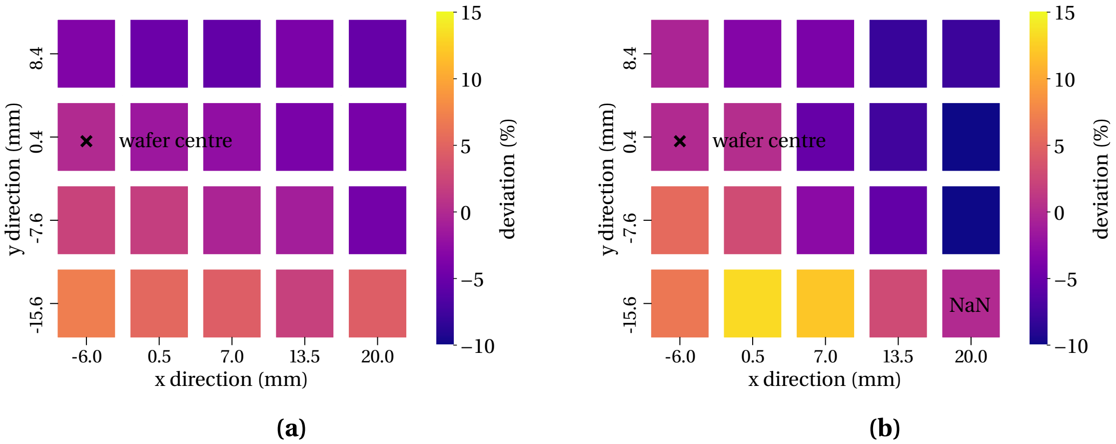

Figure 4.20: The spatial distribution of the resistivity is investigated for two films: (a) $\rho = 490\,\mu\Omega\,\text{cm}$ and (b) $\rho = 4900\,\mu\Omega\,\text{cm}$. The values correspond to the deviation relative to the value at the wafer centre. Although both films show a different distribution, a gradient from the top right corner to the bottom left corner is noticeable. The difference between both films is caused by statistical errors.

resulted in $4900\,\mu\Omega\,\text{cm}$. The fabrication parameter used are $n_{\text{Rate}} = 1.0\,\text{nm/s}$ and $f_{O2} = 5.8\,\text{sccm}$.

The spatial distribution in resistivity is shown in colour in Fig. 4.20a and Fig. 4.20b relative to the value at the wafer centre. The distributions of both films show a gradient that increases from the top right corner to the bottom left corner. Since the oxygen valve is located to the left of the wafer, the oxygen gas reaches the bottom left area first and spreads from there on over the wafer. On this way, more insulating oxide is formed on the bottom left, resulting in lower conductivity. Also, the pump that regulates the chamber pressure contributes to the inhomogeneity. Rotation of the sample holder during the deposition may counteract this effect. However, the influence on the area around the wafer centre seems to be small. The exact values of both samples differ from each other and can be traced back to statistical errors. However, to verify this a comparison of more samples is necessary.

4.2.3 Samples for Measuring the Critical Temperature

The critical temperature of grAl is necessary to calculate $L_{\text{kin}}^{\square}$, see Eq. (3.7). To determine T_c, five samples of different resistivity have been fabricated in duplicate. The investigation of the samples and the measurement of the critical temperature are given in section 5.

All samples have been fabricated on a single low-ohmic 2" silicon wafer (*Si-Mat*, $\rho = 1 - 30\,\mu\Omega \cdot \text{cm}$, p-Typ, orientation: <100>). In Fig. 4.21, the geometry of the sample structure is shown. To reach a high net resistance and to neglect contact resistances during the measurement, a meander structure is chosen. The pads of 300 µm × 300 µm are used for bonding the structure to a printed circuit board. After sample development, the wafer is divided into five sections using a diamond cutter. A 20 nm thick film of granular aluminium of different resistivity is deposited on each wafer section, following the recipe in section 4.2.2.2. This is done by regulating the oxygen mass flow to values between 3.7 sccm and 5.5 sccm. The evaporation rate has been kept constant at 1.0 nm/s for each sample. After lift-off in acetone, the sample resistances have been measured using wolfram needles and a commercial multimeter. Tab. 4.4 lists the determined values whereas the uncertainty of ρ equals the reproducibility error of 18 %.

Table 4.4: Samples for measuring the critical temperature: To provide films of different resistivity, the oxygen mass flow is regulated to different values while keeping an evaporation rate of 1.0 nm/s for each sample. The uncertainty in ρ is 18 %.

f_{O2} (sccm)	3.7	4.0	4.5	5.0	5.5
ρ ($\mu\Omega \cdot$ cm)	140(30)	200(40)	450(80)	1900(40)	4800(900)
	150(30)	190(40)	470(90)	2000(400)	5000(900)

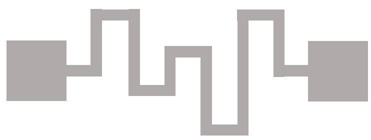

Figure 4.21: Sample geometry: The meander structure has been chosen to ensure that the net resistance is large, so contact resistances can be neglected during measurement.

Additionally, the evolution of the grain size versus resistivity has been investigated by comparing the most low-ohmic and high-ohmic samples. For this, the sample surface is investigated using the InLens Duo detector of SEM of the lithography machine. In Fig. 4.22, pictures of both surfaces are shown. Although the resolution is poor because the maximal magnification of the detector is in the order of grain size, one can see that the grain size stays approximately at 5 nm independent from the resistivity. This is in agreement with earlier observations [17, 19].

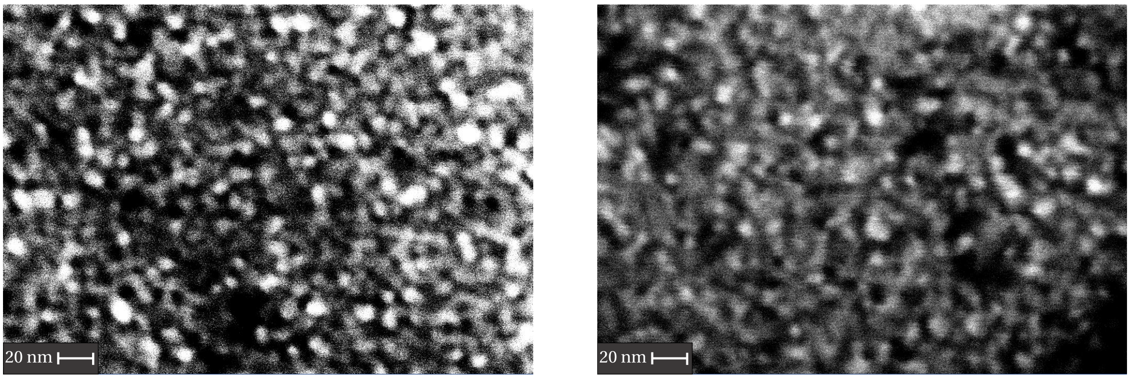

(a) $\rho = 140(30)\ \mu\Omega \cdot \mathrm{cm}$

(b) $\rho = 4800(900)\ \mu\Omega \cdot \mathrm{cm}$

Figure 4.22: Grain size: The grain size stays constant at approximately 5 nm independent from the resistivity. This is in agreement with earlier observations [17, 19]. The pictures of the films fabricated on a silicon substrate has been taken using the InLens Duo detector of the SEM. (a) Low-ohmic sample: Magnification: 372k, Aperture: 30 µm, Acceleration voltage: 3 kV, Working Distance: 5.8 mm (b) High-ohmic sample: Magnification: 437k, Aperture: 30 µm, Acceleration voltage: 5 kV, Working Distance: 5.8 mm

4.2.4 Fabrication of the Multilayer Resonator

As introduced in section 4.1.3.1, the resonator is made from two films laying congruently on each other. The resonator has been fabricated by C. Schneider. For fabrication, a single 2" sapphire wafer (*KYOCERA*, 0.33 mm thickness, single crystal) has been chosen and the fabrication routine described in section 4.2.2.2 has been carried out. However, to create two layers of granular aluminium, step 4 to 10 in the fabrication recipe are repeated: In the first run, a high-ohmic film using $f_{O2} = 4.5$ sccm and $n_{Rate} = 1.0\,\mathrm{nm/s}$ of 20 nm thickness is deposited. After this, the sample holder is tilted by 45° and a second low-ohmic film of 40 nm thickness is applied using $f_{O2} = 3.2$ and $n_{Rate} = 1.0\,\mathrm{nm/s}$. The average resistivity of the two-layer structure is determined to be $\rho = 150(30)\ \mu\Omega \cdot \mathrm{cm}$ whereas the high-ohmic layer shows a resistivity of $\rho = 650(120)\ \mu\Omega \cdot \mathrm{cm}$ and the low-ohmic one is $\rho = 50(9)\ \mu\Omega \cdot \mathrm{cm}$. The latter two values have been determined based on equivalently fabricated films.

4.2.5 Resonators for Characterizing Granular Aluminium

The resonators introduced in section 4.1.3.1 have been fabricated on a 2" silicon wafer of 300 µm thickness (*Sil'tronix*, $\rho > 10^4\ \Omega \cdot \mathrm{cm}$, intrinsic, orientation: <100>). A 20 nm thick film of granular aluminium has been deposited using an oxygen flow of $f_{O2} = 5.5$ sccm and an evaporation rate of 1.0 nm/s. To determine the sheet resistance of the film, five additional meander structures have been fabricated on the same wafer. Using wolfram needles, the resistivity has been determined to be $\rho = 4600(800)\ \mu\Omega \cdot \mathrm{cm}$.

4.3 Summary

A simulation routine to develop microstrip resonators made from granular aluminium has been figured out. The high intrinsic impedance is respected by employing the *impedance* boundary and adjusting a kinetic sheet inductance. Following this routine, geometries of six high-impedance resonators have been determined that provide coupling Q factors of $\sim 10^4$. Depending on the substrate that is either sapphire or silicon, the resonances lie in a range from 7 GHz to 9 GHz. The theory that Q_c can be increased by tilting the resonator has been verified by executing simulations similar to the routine developed for the geometry determination. Further, a low-impedance resonator design has been developed to refine a design for a SQUID resonator.

The fabrication of films made from granular aluminium has been characterized. Films of specific resistivity are obtained by electron beam evaporating aluminium in a pure oxygen atmosphere and adjusting the process parameter that is the oxygen mass flow and the evaporation rate. A large evaporation rate $\geq 1.0\,\mathrm{nm/s}$ is suggested since it supports the stabilization of the evaporation rate, which is crucial for the film quality and reproducibility. Experience shows that an undefined pattern of the electron beam supports the stabilization of the evaporation rate as well. It is also suggested to rotate the sample holder during the evaporation process, so a spatially homogeneous film is deposited. Finally, the resonators investigated by simulation have been fabricated.

Chapter 5
Critical Temperature of Granular Aluminium

The critical temperature of the films made from granular aluminium is not only of interest but necessary for calculating the kinetic inductance of the resonators fabricated in this thesis. Therefore, this chapter presents the results obtained from transport measurement. The fabrication of sample made for this purpose is described in the section 4.2.3.

5.1 Setup & Sample Mounting

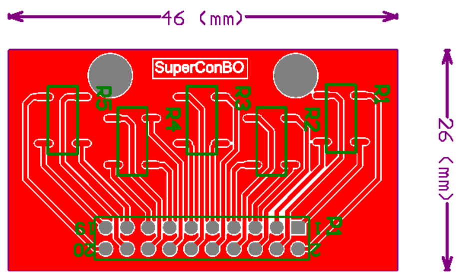

Figure 5.1: Sample mounting: Six samples have been bonded to the PCB using aluminium wires. Thermalization is ensured applying low-temperature varnish between the samples and the board. The PCB is screwed to the base stage of the dilution refrigerator.

In total, six samples differing in resistivity, are bonded to a printed circuit board (PCB) using aluminium wires. The board is made from non-flammable epoxy laminate material (FR-4). To ensure the thermalization of the samples, low-temperature varnish has been applied between these and the PCB. The PCB is then screwed by two M3 screws to the base stage of a delusion refrigerator. A detailed description of the cryogenic system is presented in Fig. B.1. The samples are connected to an AC resistance bridge (*LAKESHORE Model 370*) that provides a bias current and measures the voltage drop over the sample. A superconducting DC-loom connects the bridge to the PCB via superconducting wires (NbTi) that have been soldered onto the board. To reduce thermal impacts the loom is connected to every stage of the cryostat using fed-throughs. A drawing of the PCB is shown in Fig. 5.1. To determine the present temperature, an additional ruthenium oxide sensor (*LAKESHORE ROX 102B*) is placed on one of the screws holding the PCB. The sensor works below 10 mK and up to 40 K with an uncertainty of 16 mK [50] .

5.2 Experiment & Discussion

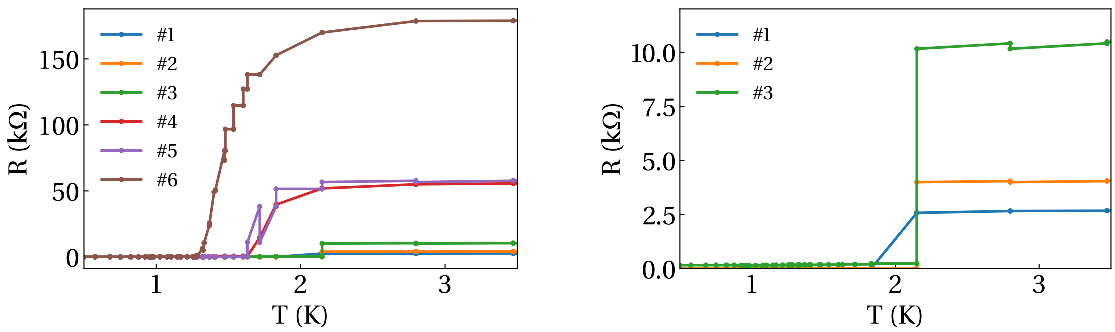

(a) **(b)**

Figure 5.2: Transition to superconductivity: The resistance R versus temperature T for six samples differing in resistivity have been observed performing transport measurements. (a) For the high-ohmic samples (#4 – #6) the transition occurs rather soft while (b) for the low-ohmic ones (#1 – #3) the resistance drops abruptly. Error bars have been neglected since they are of a few Ohms. Details are given in the text.

Fig. 5.2a shows the result of the transport measurement for all six samples and Fig. 5.2b zooms on the low-ohmic samples #1 – #3. Error bars have been neglected since they lie in the range of a few Ohms. In total, the cryostat temperature has been ramped down to below 0.5 K three times while recording the samples resistances. The critical temperature is determined by reading off the inflection point. The uncertainty is estimated to be 0.05 K, corresponding to the spacing between the measurement points around the inflection point. The results are listed together with the samples resistivity and fabrication parameters in Tab. 5.1. The resistivity has been determined

Table 5.1: The table lists the results from the measurement together with the oxygen mass flow f_{O2}used for fabrication. The critical temperature T_c decreases with increasing resistivity ρ as phase fluctuations get prominent. All samples have been fabricated using an evaporation rate of 1.0 nm/s.

	#1	#2	#3	#4	#5	#6
f_{O2} (sccm)	3.7	4.0	4.5	5.0	5.0	5.5
ρ ($\mu\Omega \cdot$ cm)	120(20)	190(30)	400(70)	1800(300)	2000(400)	4800(900)
T_c (K)	1.90(5)	2.20(5)	2.20(5)	1.60(5)	1.60(5)	1.30(5)

after the samples were bonded to the PCB. Since the contact to the sample via a bonded wire is more stable than using wolfram needles as done so far, the determined values differ by up to −16%. The uncertainty in ρ equals the reproduction error of 18 %.

Having a look at Fig. 5.2, the way the resistance changes for the high ohmic samples compared with the low-ohmic ones is noticeable: For sample #4 – #6, the transition occurs rather softly than abruptly. According to Dubouchet et al. [39], the mechanism behind this relies on quantum localization of the single electron states that start preforming Cooper pairs and causing the two energy gaps, Δ_c and Δ_p that get observed in grAl. As discussed in section 3.1, the pseudogap Δ_p then evolves into a hard gap E_g. Applying this explanation to the transition of the low-ohmic samples #1 – #3, one can conclude that the superconductivity of these samples might feature low disorder since their resistances drop occurs abruptly. So, samples #4 – #6 carry high-disordered films.

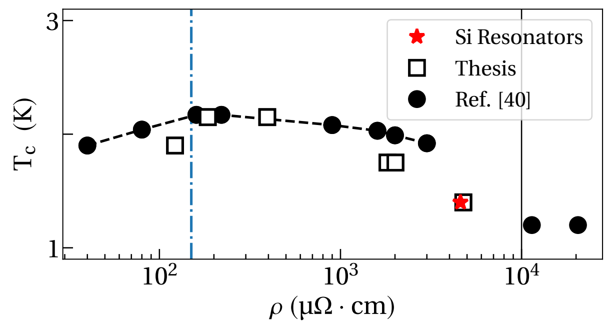

Figure 5.3: Critical temperature T_c determined in this thesis (white squares) compared with results from Levy-Betrand et al [40] (black circles): The distribution of the temperature follows the dome-like behaviour, reaching almost the same maximal value (2.2 K) and decreasing for films of higher resistivity. The deviation of the high-ohmic samples (> 20 %) might be caused by strong disorder. The red star indicates the location of the high-impedance resonators made on silicon whereas as the blue dashed line indicates the location of the U-shaped low-impedance resonator since for the T_c has not been determined. The black solid line at $\rho = 10^4\,\mu\Omega\cdot\mathrm{cm}$ indicates the superconductor-to-insulator transition (SIT) [44]. Error bars are point-sized.

Fig. 5.3 shows the critical temperature versus resistivity compared with results obtained by the research group of I. Pop at the Karlsruhe Institute of Technology (KIT) [40]. The error bars in Fig. 5.3 are point-sized. The blue dashed line assigns the U-shaped resonator introduced in section 4.2.4. Since the critical temperature of this film has not determined, no data point is available. The red star indicates the high-impedance resonators made on silicon substrates: The film parameters used for their fabrication correspond to sample #6, therefore the critical temperature of the resonators is assumed to be same. The solid line in Fig. 5.3 indicates the superconductor-insulator transition (SIT) [44]. Except for sample #6, the T_c of all samples lies in a range of 1.30(5) K to 2.20(5) K, exceeding the T_c of bulk aluminium (∼1.2 K) [51]. and is well comparable to the results from Levy-Bertrand et al. Although less data points are available, the dome-like distribution is recognizable.

Particularly, the maximal T_c is reached for almost the same value (2.2 K, 98 % matching) from a similar film resistivity of 190(30) $\mu\Omega \cdot$ cm (86 % matching). Sample #6, however, differs in T_c by $> 30\%$ and the T_c lies close to the value of bulk aluminium like the insulating samples left from the SIT in Fig. 5.3 measured by Levy-Bertrand et al. Since the sample film is located close to the SIT at $\rho = 10^4\ \mu\Omega \cdot$ cm, the sample film might be already influenced by localization effects and features a special high disorder with strong grain coupling. Based on this observation, it is suggested that the SIT might be not located at an exact value but rather spreads over an area around this, causing high disorder and strong localization effects already below $10^4\ \mu\Omega \cdot$ cm.

5.3 Summary

Performing transportation measurements the critical temperature of six samples fabricated on silicon substrates has been determined. The results correspond well to previous observation [40]. The typical dome-like distribution of the critical temperature as a function of the room temperature resistivity is observed, revealing a maximal T_c of 2.20(5) K for films of $\rho = 190(30)\ \mu\Omega \cdot$ cm. However, the observed results suggest that the SIT rather happens over a range of $(1.0 \pm 0.1 \times 10^4)\ \mu\Omega \cdot$ cm than at a fixed border of so far communicated $10^4\ \mu\Omega \cdot$ cm [44], leading to special high disordered films close to this drop off.

Chapter 6
Transmission Measurements

This chapter presents the experimental results obtained by investigating the resonators in transmission configuration. Measurements have been performed using different input powers and temperatures between 30 mK to 500 mK. Also, the effect of a micro magnet mounted on the setup has been analysed. After introducing the employed setup, the results are discussed and compared to the simulation as far as possible.

6.1 Measurement Setup

In essence, the employed setup consists of the resonators on their substrates that are inserted in the waveguide. The waveguide itself is placed in a dilution refrigerator. The measurements are performed in notch configuration.

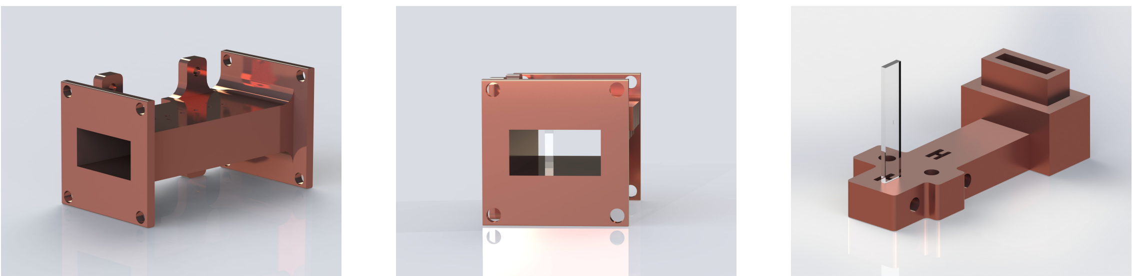

(a) **(b)** **(c)**

Figure 6.1: CAD rendered picture of (a) and (b) the waveguide (WR102 standard) and (c) the clamp holding a sample on a sapphire substrate. For creating the picture the software *SolidWorks* has been used.

6.1.1 Waveguide

Since the waveguide takes up a certain volume inside the space limited refrigerator, it is designed in a way that multiple samples can be installed similar to previously performed experiments.[28] In total, the waveguide system consists of three parts: The waveguide itself, three clamps which

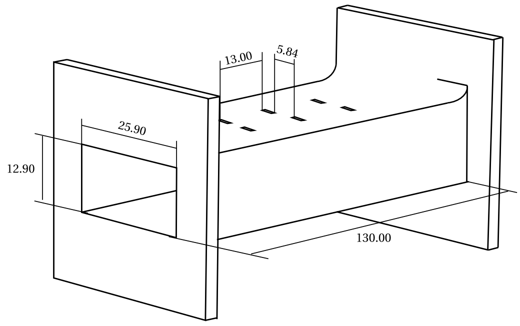

Figure 6.3: Illustration of the waveguide to visualize its size.

each hold two substrates and two couplers, one at the beginning and one at the end of the waveguide. Both, the waveguide and the clamp are made from copper. A CAD rendered picture of the waveguide can be seen in Fig. 6.1a and 6.1b. Fig. 6.1c shows a clamp used for holding the samples. The employed couplers are commercial ones (*PASTERNACK*) and used to match the impedance of the incoming microwave and to receive it at the end of the waveguide. They correspond to the WR102 standard that equals a waveguide width and height of 25.9 mm × 12.9 mm. The total length of the waveguide is 130 mm. By this, the substrates are spaced 13 mm from each other along the waveguide axis and have a lateral distance of 5.84 mm. Fig. 6.3 illustrates the dimensions. According to Eq. (1.36) the waveguide cutoff frequency is 5.78 GHz which is also verified by Fig. 6.2 that shows a transmission measurement of the waveguide at room temperature.

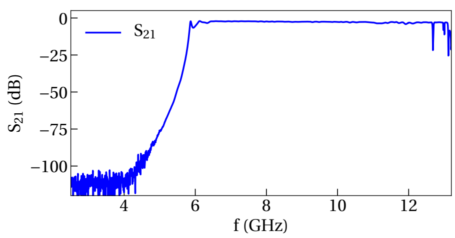

Figure 6.2: Transmission measurement of the waveguide at room temperature. The cut off frequency lies at 5.8 GHz.

6.1.2 Dilution Refrigerator Setup

The waveguide is installed to the baseplate of the cryostat (*Oxford Instruments*) and is surrounded by a double layer permalloy can along with superconducting aluminium shields to shield any magnetic fields from the outside. The waveguide is connected via SMA ports to the feed line. To couple in a clean input signal, first, any DC-offset is removed by a DC block. Next, the signal passes a −20 dB at the 4 K stage and a −30 dB attenuator at the base plate (20 mK) to lower thermal noise. Before the signal then enters the waveguide, an Ecosorb filter absorbs any infrared radiation.

Propagating through the waveguide and leaving it again on the other end, the signal passes a DC 12 GHz filter and two isolators subsequently. The latter two ensure that no signal is entering through the output port. By this, noise form the high-electron-mobility transistor (HEMT) leaking back to the waveguide is prevented. The HEMT is located at the 4 K plate. This and a +40 dB amplifier finally amplify up the signal again before being recorded by the vector network analyser (VNA). A survey of the complete setup is presented in the appendix B, Fig. B.1.

6.2 Experimental Results

6.2.1 Resonators Made on Silicon Substrates

The highimpedance resonators introduced in chapter 4 have been mounted to the set up as previously described. Considering the discussion on the critical temperature in chapter 3.24, the resonators feature a kinetic sheet inductance of 2.4(5) nH following Eq. (3.7). This is in good agreement with the $L_{\mathrm{kin}}^{\square} = 2.0\,\mathrm{nH}$ used for simulation. However, no resonances have been observed in a broad investigated frequency range from 3 GHz to 12 GHz. This can have multiple reasons that are discussed in the following.

While mounting the samples they might have been damaged. However, no destruction has been observed after demounting them again.
Another reason might be the fabrication of an incorrect resonator geometry that does not exactly equal the design developed during the simulation. Slight variations in the dimensions change the resonator eigenfrequency. However, the broad frequency range mentioned above has been investigated without measuring any resonance. Therefore, this reason is discarded.
Since the resistivity of the film the resonators is located far to the right of the superconducting dome and close to the SIT, see Fig. 5.3, the film might be insulating or it is strongly disordered and no phase coherence over the whole resonator is achieved. Although, the superconductivity of an equivalent film has been proven (5.2a, sample #6), spatial inhomogeneities of the deposited film might lead to an higher ρ since the resistivity of the film has been measured at test structures located to the upper edge of the wafer whereas the resonators are fabricated in the wafer centre. According to the investigation made in section 4.2.2.5, the film resistivity varies up to 15% over the wafer which can lead to an effective resistivity of $\rho \geq 5.0\,\mu\Omega\cdot\mathrm{cm}$. This consideration supports the hypothesis made in the previous chapter: The SIT might occur already for smaller values and rather happens over a range of $(1.0\times10^4 \pm 0.1\times10^4)\,\mu\Omega\cdot\mathrm{cm}$ than at a fixed border.

Concluding, to obtain superconducting resonators made from granular aluminium, it is useful to create films of resistivity that is located to the dome centre in a range from $10^2\,\mu\Omega\cdot\mathrm{cm}$ to $10^3\,\mu\Omega\cdot\mathrm{cm}$, at least one order below the SIT. The desired kinetic sheet inductance can be achieved by adjusting the film thickness according to Eq. (3.7). It also shall be pointed out that using higher evaporation rates might lead to a more homogeneous distributed film as discussed in section 4.2.2.

6.2.2 U-shaped Resonator

6.2.2.1 Overview

Measurements have been performed with zero and non-zero external magnetic field. First, the results with the influence of the field are discussed. These have been performed in dependency on the input power P_{in} and refrigerator temperature T. The results obtained with zero external field are given in section 6.2.2.4. The exact value of the magnetic field strength that reaches the resonator could not be determined directly but it is estimated to be $\sim$ mT.

To discuss the effect of the input power and temperature on the Q factors and resonance, the number of photons in the resonator is an important variable that is estimated by [52]

$$\bar{N} = \frac{1}{2\pi h f^2} \frac{Q_L^2}{Q_c} P_{\text{in}} \,. \tag{6.1}$$

Note that the input power is attenuated by the employed cables and attenuators in the measurement setup by -90 dBm.
For the temperature dependency measurements, a heater inside the fridge was used, regulated by a PID controller. Before recording the sample transmission at a specific temperature, it has been waited until the sample thermalizes.
To extract the Q factors from the measurement data, the circle fit routine described in section 2.6 is used.

6.2.2.2 Power Dependency Measurement

To investigate the impact of the photon number in the resonator, the input power applied at the VNA has been varied between $+15$ dBm and -75 dBm. Using Eq. (6.1), the corresponding photon number lies between $\bar{N} = 1$ and $\bar{N} = 10^8$. Fig. 6.4 shows the evolution of the coupling and in internal Q factor. Error bars are point-sized. Contrary to the expectation, Q_c decreases for small photon numbers close to the single-photon regime. According to Eq. (2.14), the coupling to the waveguide depends only on the resonator geometry and should remain the same, independent of variables like the photon number. To achieve small photon numbers below $\bar{N} = 10^2$, the (VNA) input powers have to be in the range of -75 dBm to -60 dBm, leading to a noisy transmission signal and a faulty determination of Q_c, illustrated in Fig. 6.5. For $\bar{N} \geq 10^6$, the non-linearity of

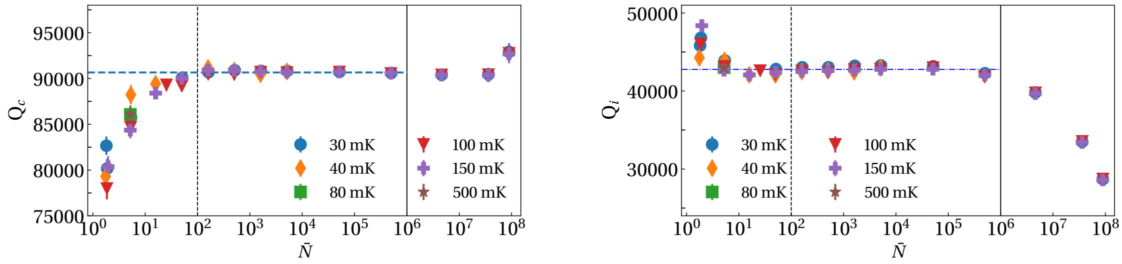

(a) **(b)**

Figure 6.4: Measured (a) coupling Q and (b) internal Q factor versus the photo number: For $\bar{N} \geq 10^6$, the non-linearity of the resonator influences the resonance strongly, so Q_c and Q_i cannot be determined to the true value since the circle fit routine is based on a linear model. The decrease in Q_c and increase in Q_i for small $\bar{N} < 10^2$ is caused by a low signal to noise ratio and are given no trust. The average value for Q_c in the range between $\bar{N} = 10^2$ to $\bar{N} = 10^6$ is $9.067(4) \times 10^4$ and $\langle Q_i \rangle = 4.278(18) \times 10^4$. Error bars are point-sized.

the resonator influences the resonance and leads to a distorted peak, see Fig. 6.5. In this regime, the circle fit routine fails to determine the exact Q factors since it is based on a linear model. Concerning Eq. (2.14), the Q_c factor should stay at a value that corresponds the average between $\bar{N} = 10^2$ to $\bar{N} = 10^6$, $\langle Q_c \rangle = 9.067(4) \times 10^4$ that is indicated by the blue dashed line in Fig. 6.4a.

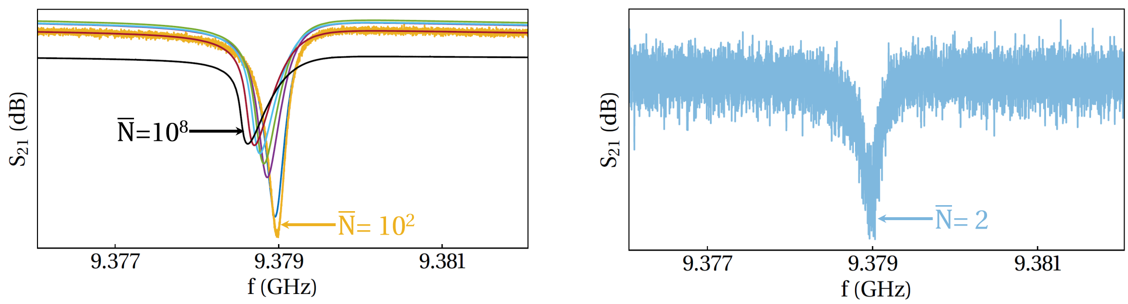

(a) **(b)**

Figure 6.5: Measured transmission signal for (a) photon numbers between 10^2 and 10^8 and (b) for $\bar{N} = 2$: For values of $\bar{N} > 10^6$, the peak shifts due to the non-linearity of the resonator. A low signal to noise ratio occurs for $\bar{N} \leq 10^2$.

Similar observations are made for the internal Q factor: Fig 6.4b shows an increase for small photon numbers while Q_i decreases in the non-linear regime. According to the discussion in section 2.3.2 and observations made by other groups [8], one would expect the opposite behaviour. Therefore, it is assumed that the increase for $\bar{N} < 10^2$ is caused by a low signal to noise ratio as well whereas the decrease at $\bar{N} > 10^6$ is caused by the non-linearity, see Fig. 6.5. The average value for Q_i in the range from $\bar{N} = 10^2$ to $\bar{N} = 10^6$ is $4.278(18) \times 10^4$. This value lies at least one order below internal Q factor measured by other groups (Grünhaupt et al.: $Q_i \geq 10^5$) [8]. As it will become clear in section 6.2.2.4, the external magnetic field causes this low Q_i value.

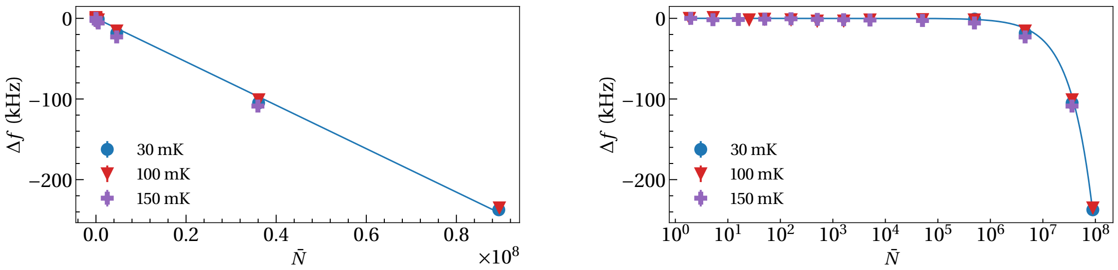

(a) **(b)**

Figure 6.6: (a) Frequency shift $\Delta f = f - f_r$ on a linear scale. For large $\bar{N} > 10^6$, the non-linearity results in a negative frequency shift. By applying a liner fit (solid line), the shift is determined to be $K_{11} = -2.7(6) \times 10^{-3}$Hz. Averaging over all temperatures, f_r is 9.378946(4) GHz. (b) shows the same plot on a logarithmic scale. Error bars are point-sized.

The internal Q factor could be enhanced using an aluminium waveguide instead of a copper one since aluminium reaches superconductivity below 1.2 K. This shields external magnetic fields and prevents losses caused by flux formations. Recent observations suggest depositing low gapped aluminium islands on the substrate around the resonator [53]. These islands act like phonon traps and lead to a reduction of quasiparticles that are generated by high energetic phonons in the substrate.

Further, a shift of the fundamental frequency is observed. Fig. 6.6 shows the shift $\Delta f = f - f_r$ on a logarithmic scale measured at 30 mK, 100 mK and 150 mK. Averaging over all temperatures, f_r is 9.378946(4) GHz. The error bars in Fig. 6.6 are point-sized. Because of the non-linear behaviour for large photon number, $\bar{N} > 10^6$, the shift appears to be negative. However, for small photon numbers $\bar{N} < 10^2$, the resonance shifts to higher frequencies. This is traced back to the small signal to noise ratio. Applying a linear fit to the data according to Eq. (3.24) and averaging, the shift per photon in the resonator is determined to be $K_{11} = -2.7(6) \times 10^{-3}$ Hz when considering it is related to the self-Kerr effect. This value is one order below the K_{11} of a comparable film (Maleeva et al.: $\rho = 160\,\mu\Omega \cdot \mathrm{cm}$, $K_{11} = 2 \times 10^{-2}$ Hz) [17]. The measured K_{11} might lay below the comparable value since only the average resistivity of the resonator matches the compared film whereas the resonator investigated here actually is composed of two films differing in resistivity. Therefore, no verification can be given whether the shift is exactly related to the self-Kerr effect as well. For temperatures below 150 mK, the shift is the same. A discussion on the temperature influence is given in the next section.

6.2.2.3 Temperature Dependency Measurement

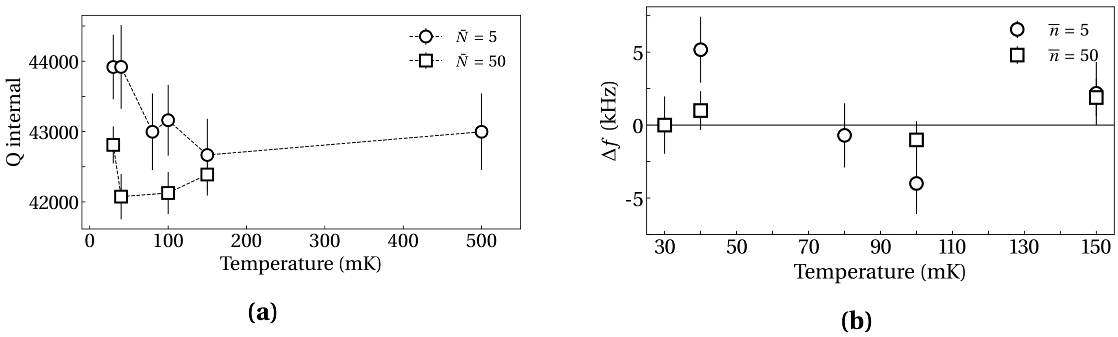

Figure 6.7: Temperature dependency for $\bar{N} = 5$ and $\bar{N} = 50$ for (a) the internal Q factor and (b) the frequency shift $\Delta f = f - f_r$, $f_r = 9.378946(4)$ GHz for both photon numbers. While Δf fluctuates around zero, a decrease in Q_i for $\bar{N} = 5$ is observed. The lack of measurement points prevents the verification of an exact trend.

In Fig. 6.7a, the results for the internal Q factor varying the temperature between 30 mK and 500 mK at $\bar{N} = 5$ and $\bar{N} = 50$ are presented. No actual trend can be seen for $\bar{N} = 50$ and Q_i seems to fluctuate around an average value of $\langle Q_i \rangle = 4.24(3) \times 10^4$. A decrease in Q_i is seen for $\bar{N} = 5$. According to the discussion on loss mechanisms in section 2.3.2, conductive losses result in a decreasing trend, Eq. (2.15), while the activation of two-level systems leads to an increase of Q_i. However, Eq. (2.15) is only valid for bulk SC and the lack of measurement points prevents the assumption of conductive losses to be the dominant loss mechanism.

Fig. 6.7b shows the frequency shift Δf observed for different temperatures between 30 mK and 150 mK for $\bar{N} = 5$ and $\bar{N} = 50$. For smaller photon numbers, the frequency is shifted by ± 7 kHz while for $\bar{N} = 50$, Δf is close to zero. Remembering the small signal to noise ratio in this regime, it is suggested that these observations are related to noise. No significant frequency shift has been expected according to the observations made by other groups [54]. A strong temperature influence is expected for $T > 300$ mK. The shift then can be predicted by a BCS model [8].

6.2.2.4 Results at Zero External Magnetic Field

In the first part of this section, the influence of the external magnetic field applied to the resonator is discussed. The second part compares the measurement at zero external field to the simulation performed in section 4.1.3.2.
The measurement recorded before the micro magnet has been installed was performed at $T = 300$ mK and at an input power of -40 dB (VNA) corresponding to $\bar{N} = 1 \times 10^4$. The results are compared to a measurement with non-zero external field at the same photon number but $T = 150$ mK. Tab. 6.1 lists both measurement results.

Table 6.1: Measurement results with zero and non-zero external magnetic field for $\overline{N} = 1 \times 10^4$. The coupling Q factor and resonance frequency lie above the values obtained by simulation, revealing a small kinetic sheet inductance of $\sim$ 20 pH. The measured Q_i lies in the order of expectation.

	T (mK)	f_r (GHz)	$Q_c/10^4$	$Q_i/10^4$	$\kappa/2\pi$ (kHz)
$B = 0$	300	9.27113196(4)	9.45(4)	8.98(5)	98.1(4)
$B \neq 0$	150	9.3789489(8)	9.07(5)	4.28(3)	103.4(6)

Although the results obtained with non-zero external magnetic field have been recorded at a different temperature, both measurements are comparable since the impact of the temperature is low according to the previous discussion. Noticeable is the decrease of Q_i by more than 50 %. According to the discussion on superconductivity in section 3.1, grAl belongs to the type II SC. The external field penetrates the material in the form of flux tubes in which no superconducting phase exists. Based on this, losses occur due to non-zero resistance [55] and the formation of vortices. This also causes the shift to a 1 % larger resonance frequency with non-zero external field. The sensitivity of granular aluminium to magnetic fields has also been shown by other groups [20].

Comparing the measurement recorded for $B = 0$ with the simulation performed in section 4.1.3.2, the measured resonance is in good agreement with the simulation using a kinetic sheet induction of 20 pH. However, the resonator fabricated shows a larger Q_c. The enhanced coupling can be traced back to small dimensional differences of the fabricated waveguide and the mounting of the sample. The measured internal Q factor lies in the expected range of 10^4 but below the Q_i observed by other groups who determined $Q_i \geq 10^5$ [8]. Internal loss mechanisms like two-level systems related to impurities might cause the lower Q_i. However, without further investigations, no exact explanation can be given.

6.2.3 Summary

Microstrip resonators made from granular aluminium differing in geometry and intrinsic impedance have been investigated in transmission configuration. No signal could be detected for the resonators fabricated with a large kinetic sheet inductance of $\sim$ 2.4(5) nH. It is assumed that the superconductivity of the film is strongly disordered and no phase coherence is achieved, so the superconducting state is prevented. To avoid this, it is suggested to fabricate films with a resistivity in the range of the dome centre that is $10^3\,\mu\Omega\cdot\mathrm{cm}$ to $10^4\,\mu\Omega\cdot\mathrm{cm}$. The desired kinetic sheet inductance can be adapted by adjusting the film thickness.

A double-layer U-shaped microstrip resonator has been characterized with zero and non-zero external magnetic field. For photon numbers between $\bar{N} = 10^2$ and $\bar{N} = 10^6$, the average coupling

Q factor is $\langle Q_c \rangle = 9.45(4) \times 10^4$ and the internal Q factor is $\langle Q_i \rangle = 8.98(5) \times 10^4$. Resonance is found in the vicinity of 9 GHz, corresponding to an average kinetic sheet inductance of 20 pH. After installing a micro magnet to the setup, the resonator has been characterized by different temperatures and photon numbers with non-zero external magnetic field of strength $\sim$ mT. Temperatures between 30 mK and 150 mK do not influence the resonator performance significantly. The internal quality factor decreases by half to a value of $\langle Q_i \rangle = 4.28(3) \times 10^4$ for $\bar{N} = 10^2$ to $\bar{N} = 10^6$ for all temperatures. The resonance shifts to a 1 % higher frequency. The frequency shift and the decrease in Q_i is caused by the external field. It penetrates the material in the form of flux tubes and causes additional internal losses due to vortices and non-superconducting areas with non-zero resistance. For small photon numbers below $\bar{N} = 10^2$, Q_c and Q_i differ from the average values which can be traced back to a low signal to noise ratio. A strong non-linearity occurring in a peak shift is observed at photon numbers of $\geq 10^6$. The resonance shifts for large photon numbers to a lower value. The shift per photon in the resonator has been determined to be $2.7(6) \times 10^{-3}$ Hz for all temperatures. In the non-linear regime, Q_i and Q_c differ from the average values as well. Concluding, it is suggested to extend the results by further measurements and to enhance the signal to noise ratio by longer averaging while recording the transmission.

Chapter 7
Coupling to a Transmon Qubit

To meet the final goal of realizing a resonator suitable to readout the state of a superconducting qubit, this chapter presents the investigation of a microstrip resonator made from granular aluminium that is coupled strongly to a transmon qubit. This is done by performing finite element simulations using the software HFSS. Before presenting the simulation results, the physics of coupling is described. Details on this can be found in the appendix A.

7.1 Coupling Theory

To simplify the derivation of the coupling between a transmon qubit [56] and a resonator, the transmon is modelled as two-level system neglecting its anharmonicity and the resonator is considered to be a linear oscillator. The complete derivation is given in the appendix A.

The Jaynes-Cumming Hamiltonian, appendix Eq. (A.1), expresses the interaction between a two-level system with mode ω_a and a linear oscillator with mode ω_b. The interaction of both modifies the original modes to so-called dressed states ω_A and ω_B [57]. These modes do not represent the bare states of the qubit or resonator but a hybridization of these. The dressed states are given by Eq. (7.1) and (7.2).

$$\omega_A = \frac{1}{2}\left(\omega_a + \omega_b - \sqrt{4g^2 + \Delta^2}\right) \tag{7.1}$$

$$\omega_B = \frac{1}{2}\left(\omega_a + \omega_b + \sqrt{4g^2 + \Delta^2}\right) \tag{7.2}$$

Here, g denotes the coupling strength between the transmon and the resonator and Δ corresponds to the detuning between both bare modes, $\Delta = \omega_a - \omega_b$. When plotting the dressed states as a function of the detuning, one obtains the characteristic avoided crossing presented in Fig. 7.1.

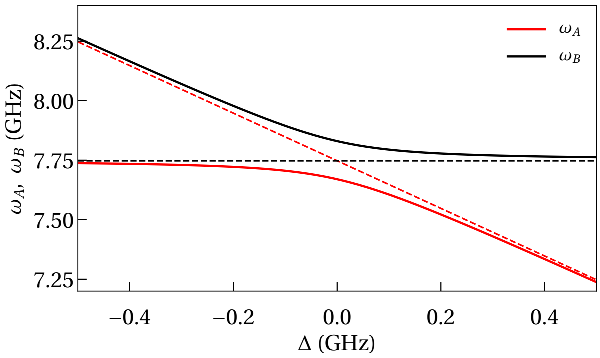

Figure 7.1: Avoided crossing: Dressed states ω_A and ω_B as a function of the detuning $\Delta = \omega_a - \omega_b$. At $\Delta = 0$, a maximal coupling is achieved and each mode is half-qubit and half-resonator. For large Δ or a small ratio of g/Δ, the dressed states turn to the original modes, ω_a and ω_b.

For large Δ, so g/Δ being small, the dressed states turn to the original modes, $\omega_A \to \omega_R$ and $\omega_B \to \omega_Q$. A maximal coupling of $2g$ is obtained for $\Delta = 0$ at which each mode is half-qubit and half-resonator.

7.2 Simulation

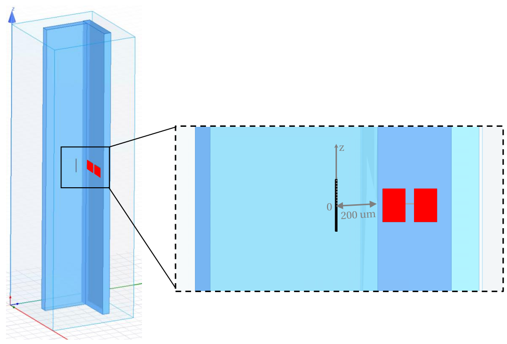

Figure 7.2: (*From left to right*) Simulation model: The resonator (dark grey) and transmon qubit (red) modelled by 2D sheets are each placed on a single sapphire substrate (blue) that are aligned in a L-form. The insert shows a zoom on the structures. The vertical displacement z of the resonator relative to the transmon is adjusted during the simulation.

To observe the avoided crossing between the resonators and the qubit, finite element simulations are performed using the Eigenmode solver of the software HFSS introduced in section 4. Doing this, the resonator and qubit are modelled as 2D sheets as suggested in section 4.1.1. Both, the resonator and the qubit are each placed on a single substrate (sapphire) that are arranged in a L-like formation as shown in Fig. 7.2, so the resonator and qubit face each other. While the

transmon is placed at the centre of the substrate, the resonator is placed horizontally close to the substrate border (the distance is $x = 200\,\mu\text{m}$) and its vertical displacement z relative to the transmon is adjusted during the simulation.
The qubit is composed of two larger rectangles of dimensions (500 × 400) µm representing the capacitors that are connected by a smaller rectangle of dimensions (10 × 40) µm corresponding to the junction, see Fig. 7.2. The resonator has a dimensions of (20 × 625) µm and a kinetic sheet inductance of 2 nH. To correctly regard the impedance of the junction, the boundary *Lumped RLC* is employed. This allows the assignment of a kinetic inductance, resistance and capacitance to the element. Because the junction is considered to act as a pure inductance, the element has a zero resistance and zero capacitance but a kinetic inductance L_J. Similar, the capacitor pads are assigned to be perfect conductors using the *Perfet E* boundary that turns elements to superconductors. Note that this boundary is assigned to every element by default. The resonator is again the boundary *impedance* assigned to correctly regard the high impedance granular aluminium has. The avoided crossing is obtained when the system is solved for the first and second mode for different detunings. To achieve this, the qubit frequency is changed by sweeping its inductance L_J using the tool *optimetrics*. Finally, the coupling g is obtained by determining the minimum of the difference between ω_A and ω_B, $2g = \min\{|\omega_A - \omega_B|\}$.

7.3 Discussion

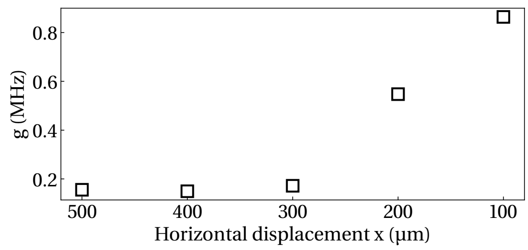

(a)

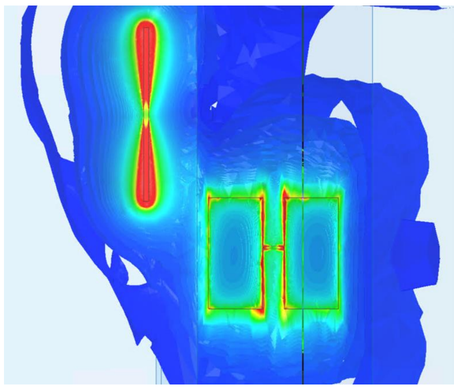

(b)

Figure 7.3: (a) Coupling strength g between the microstrip resonator with the dimensions (20 × 625) µm and a transmon qubit. At a fixed horizontal position, the resonator is shifted vertically upwards. The coupling enhances since it increases proportionally to the field gradient. In (b), a plot of the magnitude of the electric field is shown when the resonator is 500 µm shifted upwards. A deviation from the symmetric identical field distribution of the transmon pads is observed. Red colours indicate higher values whereas blue colours represent low values.

At a horizontal position of $x = 200\,\mu m$, the vertical position of the resonator then has been changed between $z = 0\,\mu m$ and $z = 500\,\mu m$. The result is shown in Fig. 7.3a. Fig. 7.3b shows a plot of the magnitude of the electric fields.

The coupling strength g enhances for larger vertical displacements up to a maximal value of $g > 100$ MHz. As the coupling mechanism is of capacitive nature and the resonator causes a larger field gradient when shifted upwards. The field gradient causes a non-symmetrical distribution of the electric field. This is recognized at the transmon pads, shown in Fig. 7.3b. So, the increase in g is expected for this configuration. When shifting the resonator above further, g will decrease again. Although g would reach an even higher value when the resonator is placed closer to the substrate border, this position has been chosen because otherwise the resonator might be damaged during fabrication.

7.4 Summary

Performing finite element simulations, the coupling of $g > 100$ MHz between a microstrip resonator to a transmon qubit has been investigated. A large coupling is achieved when the resonator is placed laterally close to the transmon and vertically shifted upwards, so a large overlap of the electric field gradient is achieved. This is realized by arranging the resonator and the qubit in a L-like formation.

Chapter 8
Conclusion

The first part of this thesis investigated the fabrication process of resonators made from granular aluminium. The fabrication consists of several preparing steps of electron beam lithography and depositing aluminium in a pure oxygen atmosphere by electron beam evaporation. It has been shown that the film resistivity strongly depends on the oxygen mass flow and evaporation rate. High evaporation rates of 1.0 nm/s or more are suggested since these are well to stabilize and enhance the film homogeneity. Due to the location of the oxygen valve and vacuum pump in the chamber, the film resistivity differs spatially. To prevent this, the sample holder can be rotated planetary.
The next part of this thesis investigated the critical temperature of granular aluminium. For this, six samples differing in resistivity fabricated on a silicon substrate have been bonded to a printed circuit board that is placed on the base stage of a dilution refrigerator. The characteristic superconducting dome has been observed and the transition temperatures for all samples correspond well to the results made by other groups except the high-ohmic samples. It is assumed that the superconductor to insulator transition (SIT) happens rather over a range around a resistivity of $10^4\,\mu\Omega\cdot\mathrm{cm}$ than at a fixed border.

To characterize the material, microstrip resonators with a large kinetic sheet inductance of 2 nH have first been simulated performing finite element simulation before fabricating and investigating them in transmission configuration. To do so, the resonators have been placed in a custom-designed waveguide made from copper that is mounted to a dilution refrigerator and cooled down below 100 mK. However, no resonance has been observed. It is assumed that the film the resonators are made from is located close to the SIT, supporting the hypothesis that this transition happens over a range. To obtain resonators made from granular aluminium, it is suggested to fabricate films with a resistivity close to the dome centre of $10^2\,\mu\Omega\cdot\mathrm{cm}$ to $10^3\,\mu\Omega\cdot\mathrm{cm}$. The desired kinetic sheet inductance can be adjusted by the film thickness.

Additionally, a U-shaped microstrip resonator consisting of two deposition films, a high-ohmic and a low-ohmic one, has been investigated to refine a design for a SQUID resonator. Before fabrication, the correct resonator dimensions have been determined by performing finite element simulation as well. By mounting the resonator to the same copper waveguide, it has been characterized in

transmission configuration. Resonance is observed in the vicinity of 9 GHz, corresponding to an average kinetic sheet inductance of 20 pH. Different input powers down to the single-photon regime have been observed as well as different temperatures up to 500 mK. The average coupling quality factor is $9.45(4) \times 10^4$ and the internal quality factor is $8.98(5) \times 10^4$ for photon number from $\bar{N} = 10^2$ to $\bar{N} = 10^6$. For small $\bar{N} \leq 10^2$, the quality factors behaves contrary to the expectation. This observation is caused by a low signal to noise ratio. For large photon numbers $\geq 10^6$, the non-linearity of the resonator leads to a decrease in the internal quality factor and an increase of the coupling Q factor. The frequency shift caused by the non-linearity has been determined to be $2.7(6) \times 10^{-3}$ Hz.
A decreasing trend of the internal quality factor for raising temperatures has been observed. However, no exact dependency could be verified. For this, more measurements at higher temperatures are necessary. According to the observations made, the resonance does not depend on temperatures below 150 mK which is also in agreement with results by other groups.
Further, the effect of an external magnetic field of mT strength has been investigated. The external field causes the internal quality factor to decrease by half and shifts the resonance to a 1 % higher frequency. This verifies the flux tuneability of granular aluminium.

In the last part of this thesis, the coupling between a high-impedance microstrip resonator and a transmon qubit has been investigated performing finite element simulations. A large coupling rate of $g > 100$ MHz is obtained when arranging the resonator and the qubit in a L-like formation and placing the resonator horizontally close to the transmon but vertically positioned above of it.

With its rich physical properties, granular aluminium is applicable in a large field of superconducting quantum circuits. In the continuation of this thesis, one can figure out different resonator geometries that result in a large coupling rate to transmon qubits to serve as a readout resonator. For this, the qubits are placed in a waveguide strongly coupled to each other and to the microstrip resonator. The readout out is performed by the resonator that is strongly coupled to the waveguide. Further, granular aluminium is suited to realize so-called superinductors and can be used to realize a fluxonoium qubit.

Bibliography

[1] Jukka P. Pekola, Olli-Pentti Saira, Ville F. Maisi, Antti Kemppinen, Mikko Möttönen, Yuri A. Pashkin, and Dmitri V. Averin. Single-electron current sources: Toward a refined definition of the ampere. *Reviews of Modern Physics*, 85(4):1421–1472, October 2013.

[2] Peter K. Day, Henry G. LeDuc, Benjamin A. Mazin, Anastasios Vayonakis, and Jonas Zmuidzinas. A broadband superconducting detector suitable for use in large arrays. *Nature*, 425(6960):817–821, October 2003.

[3] Xiu Gu, Anton Frisk Kockum, Adam Miranowicz, Yu-xi Liu, and Franco Nori. Microwave photonics with superconducting quantum circuits. *Physics Reports*, 718-719:1–102, November 2017.

[4] Guillem Via, Gerhard Kirchmair, and Oriol Romero-Isart. Strong Single-Photon Coupling in Superconducting Quantum Magnetomechanics. *Physical Review Letters*, 114(14):143602, April 2015.

[5] Vladimir Eduardovich Manucharyan. *Superinductance*. PhD thesis, Yale University, New Haven, 2012.

[6] Susanne Richer, Nataliya Maleeva, Sebastian T. Skacel, Ioan M. Pop, and David DiVincenzo. Inductively shunted transmon qubit with tunable transverse and longitudinal coupling. *Physical Review B*, 96(17):174520, November 2017.

[7] Jiansong Gao. *The physics of superconducting microwave resonators*. PhD thesis, California Institute of Technology, 2008.

[8] Lukas Grünhaupt, Nataliya Maleeva, Sebastian T. Skacel, Martino Calvo, Florence Levy-Bertrand, Alexey V. Ustinov, Hannes Rotzinger, Alessandro Monfardini, Gianluigi Catelani, and Ioan M. Pop. Loss Mechanisms and Quasiparticle Dynamics in Superconducting Microwave Resonators Made of Thin-Film Granular Aluminum. November 2018.

[9] Jens Koch, Terri M. Yu, Jay Gambetta, A. A. Houck, D. I. Schuster, J. Majer, Alexandre Blais, M. H. Devoret, S. M. Girvin, and R. J. Schoelkopf. Charge-insensitive qubit design derived from the Cooper pair box. *Physical Review A*, 76(4), October 2007.

[10] Michael A. Nielsen and Isaac L. Chuang. Quantum Computation and Quantum Information by Michael A. Nielsen, December 2010.

[11] J. Ignacio Cirac and Peter Zoller. Goals and opportunities in quantum simulation. *Nature Physics*, 8:264–266, April 2012.

[12] D. Willsch, M. Nocon, F. Jin, H. De Raedt, and K. Michielsen. Gate-error analysis in simulations of quantum computers with transmon qubits. *Physical Review A*, 96(6):062302, December 2017.

[13] Vladimir E. Manucharyan, Jens Koch, Leonid I. Glazman, and Michel H. Devoret. Fluxonium: Single cooper-pair circuit free of charge offsets. *Science*, 326(5949):113–116, October 2009.

[14] Ioan M. Pop, Kurtis Geerlings, Gianluigi Catelani, Robert J. Schoelkopf, Leonid I. Glazman, and Michel H. Devoret. Coherent suppression of electromagnetic dissipation due to superconducting quasiparticles. *Nature*, 508(7496):369–372, April 2014.

[15] M. T. Bell, I. A. Sadovskyy, L. B. Ioffe, A. Yu. Kitaev, and M. E. Gershenson. Quantum Superinductor with Tunable Nonlinearity. *Physical Review Letters*, 109(13):137003, September 2012.

[16] N A Masluk, I M Pop, A Kamal, Z K Minev, and M H Devoret. Microwave Characterization of Josephson Junction Arrays: Implementing a Low Loss Superinductance. September 2012.

[17] N. Maleeva, L. Grünhaupt, T. Klein, F. Levy-Bertrand, O. Dupré, M. Calvo, F. Valenti, P. Winkel, F. Friedrich, W. Wernsdorfer, A. V. Ustinov, H. Rotzinger, A. Monfardini, M. V. Fistul, and I. M. Pop. Circuit Quantum Electrodynamics of Granular Aluminum Resonators. September 2018.

[18] T. Chui, P. Lindenfeld, W. L. McLean, and K. Mui. Coupling and isolation: Critical field and transition temperature of superconducting granular aluminum. *Physical Review B*, 24(11):6728–6731, December 1981.

[19] G. Deutscher, H. Fenichel, M. Gershenson, E. Grünbaum, and Z. Ovadyahu. Transition to zero dimensionality in granular aluminum superconducting films. *Journal of Low Temperature Physics*, 10(1):231–243, January 1973.

[20] Lukas Grünhaupt, Martin Spiecker, Daria Gusenkova, Nataliya Maleeva, Sebastian T. Skacel, Ivan Takmakov, Francesco Valenti, Patrick Winkel, Hannes Rotzinger, Wolfgang Wernsdorfer, Alexey V. Ustinov, and Ioan M. Pop. Granular aluminium as a superconducting material for high-impedance quantum circuits. *Nature Materials*, 18(8):816–819, August 2019.

[21] C. Axline, M. Reagor, R. Heeres, P. Reinhold, C. Wang, K. Shain, W. Pfaff, Y. Chu, L. Frunzio, and R. J. Schoelkopf. An architecture for integrating planar and 3d cQED devices. *Applied Physics Letters*, 109(4):042601, July 2016.

[22] Markus Aspelmeyer, Tobias J. Kippenberg, and Florian Marquardt. Cavity Optomechanics. *Reviews of Modern Physics*, 86(4):1391–1452, December 2014. arXiv: 1303.0733.

[23] Alexander G. Krause, Martin Winger, Tim D. Blasius, Qiang Lin, and Oskar Painter. A high-resolution microchip optomechanical accelerometer. *Nature Photonics*, 6(11):768–772, November 2012.

[24] Joerg Bochmann, Amit Vainsencher, David D. Awschalom, and Andrew N. Cleland. Nanomechanical coupling between microwave and optical photons. *Nature Physics*, 9(11):712–716, November 2013.

[25] Max Ludwig and Florian Marquardt. Quantum many-body dynamics in optomechanical arrays. *Physical Review Letters*, 111(7):073603, August 2013. arXiv: 1208.0327.

[26] S. Mancini, V. I. Man'ko, and P. Tombesi. Ponderomotive control of quantum macroscopic coherence. *Physical Review A*, 55(4):3042–3050, April 1997.

[27] David M. Pozar. *Microwave engineering*. Wiley, Hoboken, NJ, 4th ed edition, 2012.

[28] David Zöpfl. Characterisation of stripline resonators in a waveguide. page 112.

[29] D. B. Leeson. S-Parameter Matrices. Technical report, 1999.

[30] Matthew James Reagor. *Superconducting Cavities for Circuit Quantum Electrodynamics*. PhD thesis, Yale University, Yale, December 2015.

[31] Agustin Palacios-Laloy. Superconducting qubit in a resonator: test of the Legget-Garg inequality and single-shot readout. page 241.

[32] Sebastian Meier. Loss reduction of superconducting coplanar microwave resonators on sapphire substrates. page 48.

[33] K Saito. Temperature Dependence of the Surface Resistance of Niobium at 1300 MHz - Comparison to BCS Theory -. page 6, 1999.

[34] D. P. Pappas, M. R. Vissers, D. S. Wisbey, J. S. Kline, and J. Gao. Two Level System Loss in Superconducting Microwave Resonators. *IEEE Transactions on Applied Superconductivity*, 21(3):871–874, June 2011.

[35] Chen-To Tai. *Dyadic Green functions in electromagnetic theory*.

[36] J. Bardeen, L. N. Cooper, and J. R. Schrieffer. Theory of Superconductivity. *Physical Review*, 108(5):1175–1204, December 1957.

[37] B. D. Josephson. The discovery of tunnelling supercurrents. *Reviews of Modern Physics*, 46(2):251–254, April 1974.

[38] Michael Tinkham. *Introduction to Superconductivity*.

[39] Thomas Dubouchet, Benjamin Sacépé, Johanna Seidemann, Dan Shahar, Marc Sanquer, and Claude Chapelier. Collective energy gap of preformed Cooper pairs in disordered superconductors. *Nature Physics*, 15(3):233–236, March 2019.

[40] F. Levy-Bertrand, T. Klein, T. Grenet, O. Dupré, A. Benoît, A. Bideaud, O. Bourrion, M. Calvo, A. Catalano, A. Gomez, J. Goupy, L. Grünhaupt, U. v. Luepke, N. Maleeva, F. Valenti, I. M. Pop, and A. Monfardini. Electrodynamics of granular aluminum from superconductor to insulator: Observation of collective superconducting modes. *Physical Review B*, 99(9), March 2019.

[41] Thomas Timusk and Bryan Wayne Statt. The pseudogap in high-temperature superconductors: an experimental survey. 1999.

[42] A P Sears. *Extending Coherence in Superconducting Qubits: from microseconds to milliseconds.* PhD thesis, Yale University, New Haven, 2013.

[43] H Rotzinger, S T Skacel1, M Pfirrmann, J N Voss, J Münzberg, S Probst, P Bushev, M P Weides, A V Ustinov, and J E Mooij. Aluminium-oxide wires for superconducting high kinetic inductance circuits. November 206.

[44] U S Pracht, N Bachar, L Benfatto, G Deutscher, E Farber, M Dressel, and M Scheffler. Enhanced Cooper pairing versus suppressed phase coherence shaping the superconducting dome in coupled aluminum nanograins. October 2015.

[45] J. A. A. J. Perenboom, P. Wyder, and F. Meier. Electronic properties of small metallic particles. *Physics Reports*, 78(2):173–292, November 1981.

[46] Rudolf Gross and Achim Marx. *Festkörperphysik.* Oldenbourg Verlag, 2012.

[47] J. Clarke and A. Braginski. *The SQUID Handbook: Fundamentals and Technology of SQUIDs and SQUID Systems, Volume I | Solid State Physics | Physics & Astronomy | Subjects | Wiley.* Wiley-VCH, 2004.

[48] G. J. Dolan. Offset masks for lift-off photoprocessing. *Applied Physics Letters*, 31(5):337–339, September 1977.

[49] MicroChem. NANO™PMMA and Copolymer. Technical report.

[50] LAKESHORE: Ruthenium Oxide (ROX) RTDs Sensors. Technical report.

[51] Bernhard Ilschner and Robert F. Singer. *Werkstoffwissenschaften und Fertigungstechnik: Eigenschaften, Vorgänge, Technologien.* Springer-Lehrbuch. Springer-Verlag, Berlin Heidelberg, 5 edition, 2010.

[52] A. Bruno, G. de Lange, S. Asaad, K. L. van der Enden, N. K. Langford, and L. DiCarlo. Reducing intrinsic loss in superconducting resonators by surface treatment and deep etching of silicon substrates. *Applied Physics Letters*, 106(18):182601, May 2015. arXiv: 1502.04082.

[53] Fabio Henriques, Francesco Valenti, Thibault Charpentier, Marc Lagoin, Clement Gouriou, Maria Martínez, Laura Cardani, Marco Vignati, Lukas Grünhaupt, Daria Gusenkova, Julian Ferrero, Sebastian T. Skacel, Wolfgang Wernsdorfer, Alexey V. Ustinov, Gianluigi Catelani, Oliver Sander, and Ioan M. Pop. Phonon traps reduce the quasiparticle density in superconducting circuits. *arXiv:1908.04257 [cond-mat]*, August 2019. arXiv: 1908.04257.

[54] Francesco Valenti, Fabio Henriques, Gianluigi Catelani, Nataliya Maleeva, Lukas Grünhaupt, Uwe von Lüpke, Sebastian T. Skacel, Patrick Winkel, Alexander Bilmes, Alexey V. Ustinov, Johannes Goupy, Martino Calvo, Alain Benoît, Florence Levy-Bertrand, Alessandro Monfardini, and Ioan M. Pop. Interplay Between Kinetic Inductance, Nonlinearity, and Quasiparticle Dynamics in Granular Aluminum Microwave Kinetic Inductance Detectors. *Physical Review Applied*, 11(5):054087, May 2019.

[55] I S Beloborodov, A V Lopatin, V M Vinokur, and K B Efetov. Granular electronic systems. February 2007.

[56] M H Devoret. Quantum Fluctuations in Electrical Circuits. volume Course 10, page 395.

[57] Kurtis Geerlings. *Improving Coherence of Superconducting Qubits and Resonators*. PhD thesis, Yale University, 2013.

Appendix A
Coupling a Resonator to a Transmon

In general, a transmon qubit is built from a capacitor and a Josephson junction, interconnected to a non-linear resonant circuit [56]. In contrary to a linear LC circuit, the Josephson junction adds an anharmonicity, so the energy levels of the transmon are not equally spaced but the energy difference decreases with the level number.

The following derivation is based on the PhD thesis by K. L. Geerlings [57]. The coupling between a two-level system and a harmonic oscillator is expressed by the Jaynes-Cummings Hamiltonian given in Eq. (A.1).

$$H_{\mathrm{JC}} = \hbar\omega_R\left(a^\dagger a + \frac{1}{2}\right) + \frac{\hbar\omega_Q}{2}\sigma_z + \hbar g\left(a^\dagger\sigma^- + a\sigma^+\right) \tag{A.1}$$

The system can be modelled by the circuit shown in Fig. A.1 when assuming the resonator and transmon qubit are capacitively coupled via two capacitors with each $2C_c$. The Jaynes-Cummings Hamiltonian then modifies to Eq. (A.2) by summing up the energies of each element (capacitor, inductance, JJ).

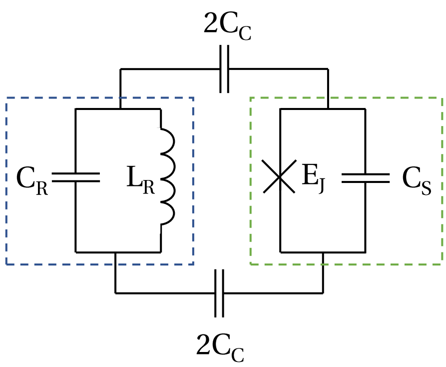

Figure A.1: Circuit model: The resonator is modelled as a linear oscillator with inductance L_R and capacitance C_R. The transmon qubit is represented as a circuit consisting of a capacitance C_s and a Josephson junction E_J. Both are coupled by two capacitances $2C_c$. Figure adapted from K. L. Geerlings [57].

$$H = \left(\frac{Q_1^2}{2}\frac{1}{C_R + (C_c||C_s)} + \frac{\Phi_1^2}{2L_R}\right) + \left(\frac{Q_2^2}{2}\frac{1}{C_R + (C_c||C_s)} - E_J \cos\left(\frac{\Phi_2}{\Phi_0}\right)\right) + \left(Q_1 Q_2 \frac{C_c}{C_R C_s + C_s C_c + C_c C_R}\right) \tag{A.2}$$

In Eq. (A.2), the first term corresponds to the resonator mode (mode a), the second one equals the qubit mode (mode b) and the last term describes the coupling. Because in this derivation, the qubit mode is assumed to be a harmonic oscillator, so the cosines term in Eq. (A.2) has to be extended for small values of the qubit phase Φ_2. Rewriting the equation and using several substitutions given in Eq. (A.5) to (A.10), the Hamiltonian splits in an ordinary term H_0 and a non-linear term H_1. The index j adapts a (resonator mode) or b (qubitresonator mode).

$$H_0 = \hbar\omega_a\left(a^\dagger a + \frac{1}{2}\right) + \hbar\omega_b\left(b^\dagger b + \frac{1}{2}\right) + \hbar g\left(a^\dagger b + a b^\dagger\right) + \hbar g\left(ab + a^\dagger b^\dagger\right) \tag{A.3}$$

$$H_1 = -\frac{E_c}{12}\left(b^\dagger + b^\dagger\right)^4 \tag{A.4}$$

$$\Phi_j = \left(j + j^\dagger\right)\sqrt{\frac{\hbar Z_j}{2}} \tag{A.5}$$

$$Q_j = -i\left(j - j^\dagger\right)\sqrt{\frac{2}{\hbar Z_j}} \tag{A.6}$$

$$Z_j = \sqrt{\frac{L_R}{(C_R + (C_c||C_s))}} \tag{A.7}$$

$$\omega_a = \sqrt{\frac{1}{L_R(C_R + (C_c||C_s))}} \tag{A.8}$$

$$g = \frac{1}{2}C_c\frac{\omega_R\omega_Q}{(C_R + C_c)(C_s + C_c)} \tag{A.9}$$

$$E_c = \frac{e^2}{2(C_s + (C_c||C_R))} \tag{A.10}$$

The last term in Eq. (A.3) can be neglected when assuming $g \ll \omega_a, \omega_b$ (rotating wave approximation). The frequencies ω_a and ω_b correspond to the bare modes that are modified by the coupling to two dressed modes ω_A and ω_B, given in Eq. (A.12) and (A.13). These states are obtained after diagonalizing the Hamiltonian, Eq. (A.11) and neglecting the anharmonicity.

$$\begin{pmatrix} a \\ b \end{pmatrix} = \begin{pmatrix} \lambda_a & \mu_a \\ \lambda_b & \mu_b \end{pmatrix} \begin{pmatrix} A \\ B \end{pmatrix} \tag{A.11}$$

$$\lambda_a = -g\sqrt{\frac{1+(4g^2)^{-1}\left(\Delta+\sqrt{4g^2+\Delta}\right)^2}{4g^2+\Delta^2}},$$

$$\lambda_b = g\sqrt{\frac{1+(4g^2)^{-1}\left(\Delta-\sqrt{4g^2+\Delta}\right)^2}{4g^2+\Delta^2}},$$

$$\mu_a = -\frac{\Delta-\sqrt{4g^2+\Delta^2}}{2}\sqrt{\frac{1+(4g^2)^{-1}\left(\Delta+\sqrt{4g^2+\Delta}\right)^2}{4g^2+\Delta^2}}$$

$$\mu_b = \frac{\Delta+\sqrt{4g^2+\Delta^2}}{2}\sqrt{\frac{1+(4g^2)^{-1}\left(\Delta-\sqrt{4g^2+\Delta}\right)^2}{4g^2+\Delta^2}}$$

$$\omega_A = \frac{1}{2}\left(\omega_a+\omega_b-\sqrt{4g^2+\Delta^2}\right) \tag{A.12}$$

$$\omega_B = \frac{1}{2}\left(\omega_a+\omega_b+\sqrt{4g^2+\Delta^2}\right) \tag{A.13}$$

When introducing the number operators N_A and N_B, the Hamiltonian can finally be written according to Eq. (A.14).

$$H_0 = \hbar\omega_A\left(A^\dagger A+\frac{1}{N_A}\right)+\hbar\omega_B\left(B^\dagger B+\frac{1}{N_B}\right) \tag{A.14}$$

The dressed states do not represent the qubit or resonator mode directly. However, for large Δ, so g/Δ being small, they go to $\omega_A \to \omega_R$ and $\omega_B \to \omega_Q$. In Fig. 7.1, ω_A and ω_B are plotted versus the detuning Δ. One can see the characteristic avoided crossing with a maximal coupling of $2g$ that is observed for $\Delta = 0$. At this point, each mode is half-qubit and half-resonator.

Appendix B
Refrigerator Setup

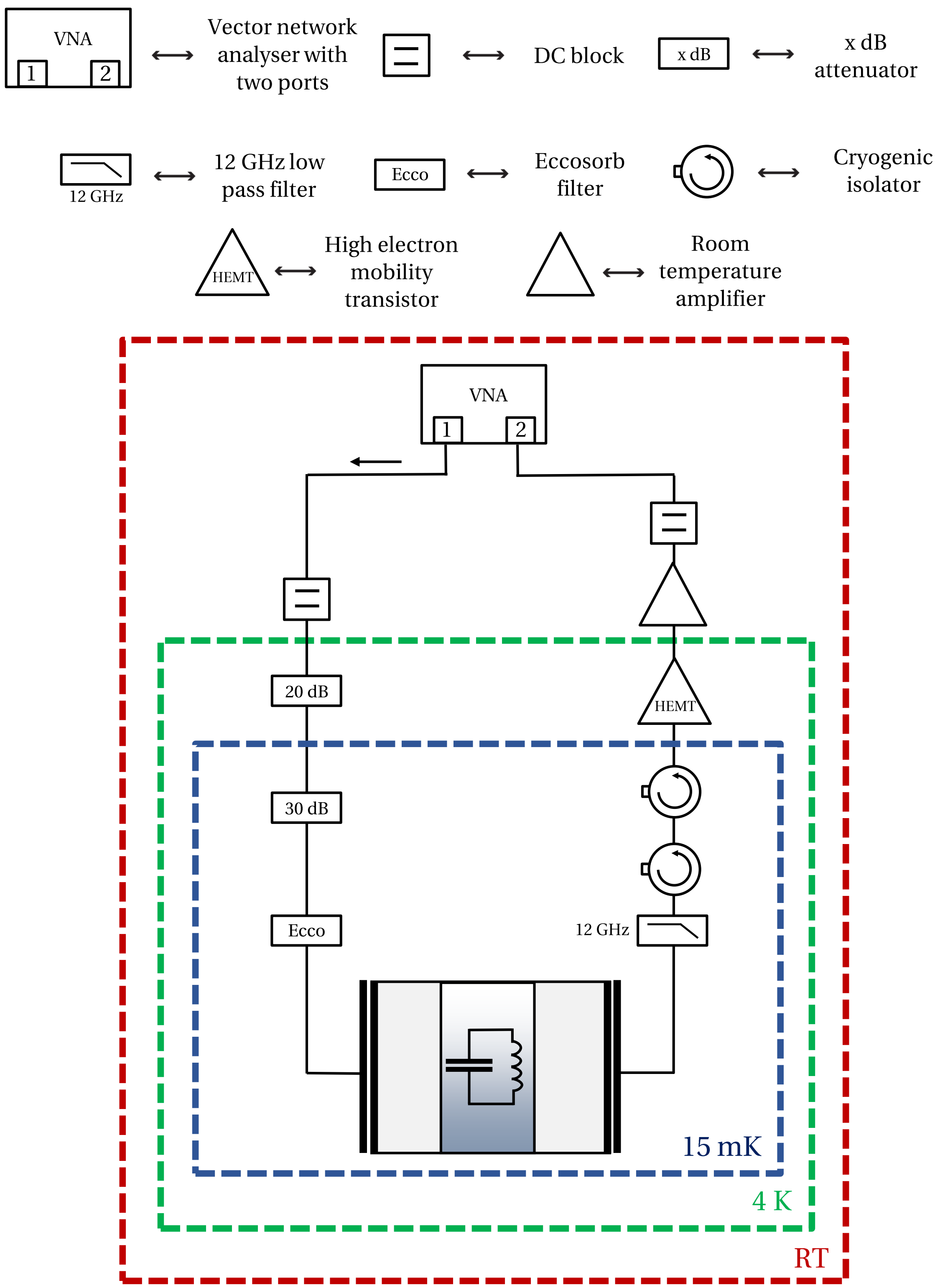

Figure B.1: Measurement setup: The waveguide is placed inside a dilution refrigerator. To couple in a clean input signal different attenuators and filters are used to lower any thermal noise. Details in the text.